# Satellite and Debris Characterisation with Adaptive Optics Imaging

**Michael Copeland**


A thesis submitted for the degree of
Doctor of Philosophy
The Australian National University

October 2020

Except where otherwise indicated, this thesis is my own original work.

Michael Copeland

6 October 2020

To Mum, Dad and Leana for their support.

# Acknowledgments

Firstly, I would like to thank my primary supervisor Francis Bennet. Your support and guidance throughout my PhD has made this possible. Without your encouragement I don't think I would have been able to make it this far. Thanks also to my co-supervisors Francois Rigaut and Celine d'Orgeville who provided advice and support.

I would also like to thank everyone in the adaptive optics group who assisted in getting AOI up and running and spending many late nights operating on the telescope. In particular I would like to thank Marcus Lingham. Over the last two years you have always been willing to help out day and night, and encouraged me to carry on even when I was losing motivation. A big thanks also goes to Doris Grosse, Ian Price, Visa Korkiakoski, and Tony Travouillon. Without your assistance and support I would not have been able to finish my PhD.

A large thanks also goes to everyone at EOS: Craig, James, Ian, Alex, Mark, Rod, Amy, Yue, Chris, and Keith. Thank you for allowing us to access and use the telescope and for all of the support you provided to get AOI working. A special thanks goes to Ian Ritchie and Alex Pollard who spent many late nights both operating and supporting us while operating the telescope.

I would also like to thank everyone at SERC: Steve, Michelle, David, and Robert. Thank you for support in going to conferences, my scholarship, and purchasing equipment for my project.

Thank you for everyone at the RSAA and AITC who have made me feel welcome. My various office mates throughout the years Elliott Thorn, Henry Zovaro, and Jamie Soon, thanks for making my time at Stromlo a bit easier with your support and friendship.

Finally, I would like to thank my family for all of the support they have provided me. Thank you to mum and dad for reading through papers and my thesis.

I must of course acknowledge the support of the Australian Government through the Australian Government Research Training Program (RTP) Scholarship, and the Cooperative Research Centre for Space Environment Management (SERC Limited) through the Australian Government's Cooperative Research Centre Programme.

# Abstract

Space debris poses a significant risk to the safety of the space environment. The field of space situational awareness (SSA) has grown in response to the increasing threat of space debris to develop methods to mitigate this threat. Precise tracking and accurate orbit predictions are needed to identify potential collisions so avoidance measures can be taken. Orbital predictions are influenced by physical characteristics which are typically unknown, and therefore must be approximated. Direct observation from a ground based telescope can measure the characteristics of an object, however the image is degraded due to atmospheric turbulence. The distortion can be overcome by using adaptive optics where the wavefront is measured and a correction is applied by a deformable mirror to return a flat wavefront. While modern developments in adaptive optics have been for astronomy applications the same methods can be used for SSA.

This thesis presents the development and operation of Adaptive Optics Imaging (AOI), an adaptive optics system for satellite and debris characterisation. AOI operates on a 1.8 m telescope located at Mt Stromlo Observatory in Canberra, Australia. AOI is capable of capturing high resolution images of objects in low Earth Orbit (LEO) to identify features and characterise objects. Satellites in geostationary orbit (GEO) can be tracked as they pass by a known reference star for accurate position measurement.

AOI was used to significantly improve images capture of stars with a Strehl ratio of 34% obtained. The effectiveness of the AO correction was shown when capturing images of Cosmos 1656 where several features could be observed during closed loop operation that were not evident in open loop. The quality of the images obtained were further improved by implementing a multi-frame blind deconvolution algorithm which made several features such as the panel array and body more visible. The satellite features were measured to obtain an approximation for the size of the satellite.

A process was developed to identify when stars will pass within 15 arcseconds of a GEO satellite. The GEO satellite position would then be measured relative to the known star position allowing an accurate tracking of a satellite. GEO satellite tracking was demonstrated with a simulation, however no on-sky tracing was successful as the GEO satellites were too dim to detect.

# Thesis Outline

A high level overview of the work completed in this thesis is provided in Chapter 1. Chapter 1 introduces the Adaptive Optics Imaging (AOI) instrument which is the foundation of this thesis and provides context for the remaining chapters. This chapter also provides relevant background theory for adaptive optics and space situational awareness. Chapter 2 introduces the requirements of the system and provides explanation on the selection of several components which drove the optical design of AOI. The optical and mechanical design is presented in Chapter 3, this includes decisions made during the design process and the expected optical performance. Chapter 4 covers the image processing techniques which are applied on all raw images captured during operation. This processing is necessary before analysis of the images is performed. The results obtained from operation of AOI are presented in Chapter 5. The results include initial lab testing and on-sky verification, and results obtained when observing satellites and debris in LEO and GEO. Chapter 6 summarises and concludes the thesis and provides future work that can build on work from this thesis.

# Contents

# List of Figures

# List of Tables

Chapter 1

# Introduction

## 1.1 AOI: Adaptive Optics Imaging

Adaptive Optics Imaging (AOI) is an adaptive optics system for space situational awareness (SSA) research and is built by the Research School of Astronomy and Astrophysics (RSAA) at the Australian National University (ANU). AOI operates on the EOS Space Research Centre 1.8 m telescope at Mount Stromlo Observatory located in Canberra, Australia. The development of AOI is in the framework of the CRC for space environment management, with ANU a contributing partner. The Space Environment Research Centre (SERC) is made up of 4 research programs which include:

- Research program 1: Tracking, Characterising and Identifying Objects in Orbit, and Preservation of the Space Environment
- Research program 2: Orbit Determination and Predicting Behaviours of Space Objects
- Research program 3: Space Asset Management
- Research program 4: Space Segment

AOI contributes to research program 1.2 (debris characterisation and object database), and 1.3 (GEO object tracking).

The primary objective of AOI is to capture high resolution images of satellite and debris for the purposes of object identification, characterisation, and tracking. This is a unique capability in Australia and data obtained through AOI will assist in refining orbital models to improve future predictions and make the space environment a safer

place to operate. Geostationary orbit (GEO) satellites will be tracked with AOI by capturing images as the satellite passes by a reference star with known position. The satellite position can be measured using astrometry in what is a novel approach for tracking satellites.

The work completed in this thesis includes the design, build and operation of AOI. The optical and mechanical design of the adaptive optics system was completed. This system was built, aligned, and integrated onto the telescope where it was commissioned, then on-sky operations were commenced.

## 1.2 Atmospheric Effects

All ground based imaging systems are subject to distortion induced by the atmosphere. The atmospheric conditions for astronomical observations is commonly referred to as seeing. This distortion is the cause of stars that 'twinkle' in the night sky and results in a degradation of performance for any optical system viewing light which passes through the atmosphere.

Atmospheric distortion or turbulence is due to local variations in the refractive index which distorts the wavefront of light passing through. The wavefront coming from a distance source such as a star can be considered flat, thus variations in the wavefront measured on the ground are due to the effects of the atmosphere. The atmosphere is a dynamic system with constantly changing temperature gradients and wind shear creating instabilities and distorting light travelling through it. The constantly changing environment results in convective cells which have a characteristic length of $r_0$ and time scale of $\tau_0$. $r_0$ is referred to as the Fried parameter and provides a measure of the strength of the turbulence.

The diffraction limit of a telescope is related to its diameter $D$ by $\lambda/D$, where $\lambda$ is the observing wavelength. When observing through the atmosphere the resolution of the system is limited to $\lambda/r_0$. If the diameter of the telescope diameter is larger than $r_0$ the diffraction limit cannot be achieve and the system is seeing limited. In effect the system is operating as if the telescope has a diameter of $r_0$.

The largest telescopes currently operating have primary mirror diameters of 8 – 10 m and the next generation of extremely large telescopes (ELTs) will have mirrors 25 – 39 m in diameter will begin operations in the mid 2020s [Tamai et al., 2016; McCarthy et al., 2018]. These large telescopes are especially affected by poor atmospheric con-

ditions degrading the possible resolution they can achieve. This effect is minimised by building the telescopes at sites with good atmospheric conditions. Tall mountains in dry locations and consistent airflow such as in the Hawaiian Islands, Chilean Andes, and Antarctica are the best sites in the world for telescopes because of the good seeing.

### 1.2.1 Atmospheric Turbulence

Kolmogorov developed a description for turbulence in 1941 [Kolmogorov, 1941]. The Kolmogorov turbulence model describes turbulences as a decay of eddies, which begin at the outer scale $L_0$ and dissipate into smaller and smaller eddies until all of the energy is dissipated at the inner scale $l_0$. The refractive index structure function in relation to a position $r$ and separation $\rho$ is given by [Roddier, 1999]

$$D_n(\rho) = \langle |n(r) - n(r+\rho)|^2 \rangle = C_n^2 \rho^{2/3} \tag{1.1}$$

where $\langle\rangle$ represents the ensemble average. $C_n^2$ is the refractive index structure constant and is a measure of the local inhomogeneities in the refractive index. If $C_n^2$ is integrated over the optical path it gives the the total amount of turbulence, which distorts the wavefront.

### 1.2.2 Observing Through a Turbulent Atmosphere

The classical means in which an electromagnetic wave is represented is by the wavefunction

$$\Psi = Ae^{i\phi} \tag{1.2}$$

where A is the amplitude of the wave and $\phi$ the phase. When coming from a distant object such as a star this becomes a plane wave before entering the atmosphere. The variations in the atmosphere's refractive index cause distortions in the flat wavefront as some parts of the wavefront will be delayed compared to others due to higher refractive indices. Over a refractive medium *n(z)* the phase fluctuation induced in the wave is given by

$$\phi = k \int n(z) dz \tag{1.3}$$

where k is the wavenumber $(2\pi/\lambda)$. Given the wavelength dependence of the phase fluctuations the wavefront is less affected at longer wavelengths so observations taken in the near infra-red (NIR) or infra-red (IR) are less impacted by atmospheric turbulence. Much like the refractive index structure function there is a phase structure function, which gives the difference in phase. The phase structure function is described by

$$D_\phi(\xi) = \langle |\phi(x) - \phi(x+\xi)|^2 \rangle \tag{1.4}$$

where $x$ is a given position and $\xi$ is a separation. The phase structure function can also be written in relation to the refractive index structure constant $C_n^2$ by

$$D_\phi(\xi) = 2.91k^2(\cos\gamma)^{-1} \int C_n^2 dh \xi^{5/3} \tag{1.5}$$

where $\gamma$ is the zenith angle of the observation. The term $(\cos\gamma)^{-1}$ relates to the amount of atmosphere that the light must pass through and is referred to as the airmass (AM). The smallest AM possible is 1 where a telescope is at zenith so looking directly upwards. As the telescope moves away from zenith the light must travel through a larger length of atmosphere, which increases the distortion caused by the turbulence.

Fried described the phase structure function as

$$D_\phi(\xi) = 6.88 \left(\frac{\xi}{r_0}\right)^{5/3} \tag{1.6}$$

where $r_0$ is the turbulence characteristic length or Fried parameter. The Fried parameter is then given by

$$r_0 = \left[0.423k^2(\cos\gamma)^{-1} \int C_n^2 dh\right]^{-3/5} \tag{1.7}$$

As $r_0$ is a function of wavenumber the wavelength dependence of the Fried parameter is $\lambda^{6/5}$, which emphasises that observations are less impacted by turbulence at longer wavelengths.

#### 1.2.2.1 Temporal Atmospheric Variations

The dynamic nature of the atmosphere means that the refractive index variations will be changing over time. Any compensation of the distorted wavefront must be at a time scale shorter than the temporal variation in the atmosphere or it is otherwise ineffective. The characteristic time scale $\tau_0$ is given by

$$\tau_0 = 0.314\frac{r_0}{V_{wind}} \tag{1.8}$$

where $V_{wind}$ is the wind velocity averaged over the turbulent layer height. Greenwood described the bandwidth required for an adaptive optics system to effectively correct for turbulence. The Greenwood frequency is a quantity used for specifying the speed required by an AO system and is given by [Beckers, 1993]

$$f_G = \frac{0.135}{\tau_0} \tag{1.9}$$

## 1.3 Adaptive Optics

A method of compensating the effects of atmospheric turbulence was proposed by Horace Babcock in 1953. Adaptive Optics (AO) systems were subsequently developed as a method to compensate for the degradation caused by atmospheric turbulence and restore the resolution of the telescope system [Buffington et al., 1977; Hardy et al., 1977].

The basic breakdown of an AO system is shown in Figure 1.1.The AO system is comprised of 3 main components; a wavefront sensor (WFS), deformable mirror (DM), and control computer. Light that is collected by the telescope is fed into the AO system where a portion is split off and sampled by the wavefront sensor. The wavefront measurements are interpreted by the control computer, which then sends commands to the deformable mirror. The deformable mirror is updated by the control computer to take a shape which corrects for the wavefront distortions. This system runs as a closed loop where the atmospheric distortions are constantly corrected as they vary over time.

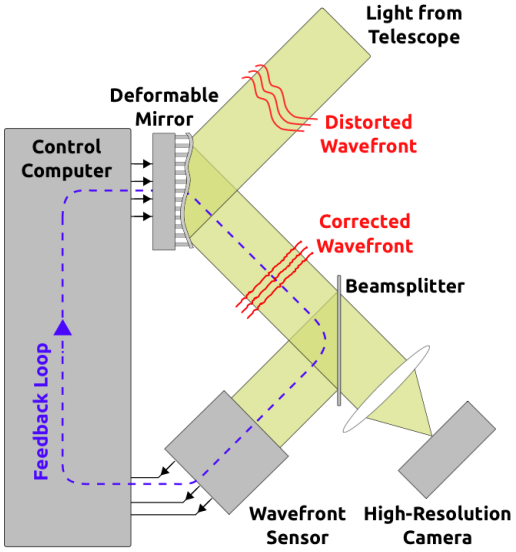


Figure 1.1: AO system components.

### 1.3.1 Shack Hartmann Wavefront Sensor

The wavefront sensor (WFS) is the component responsible for measuring the wavefront aberrations so the AO system can apply a correction. There are many different types of wavefront sensor that can be used including; Shack Hartmann wavefront sensor (SHWFS), pyramid wavefront sensors, curvature wavefront sensors, and others. The most common type of wavefront sensor is the Shack Hartmann wavefront sensor and is the WFS type used in this thesis.

A SHWFS samples a beam through a microlens array, which is a grid of small lenses. Each of the microlenses focuses the potion of the beam onto a detector, resulting in a grid of spots which can be measured. The SHWFS is located in a pupil plane that is conjugated to the deformable mirror and the layer of atmosphere being sampled. For a single conjugate AO system the DM and WFS are typically conjugated to the primary or secondary mirror of the telescope.

Figure 1.2 shows the concept of the SHWFS. If the incoming wavefront is flat or not aberrated then the the spots produced are centred on the microlens array grid. However, if the incoming beam is aberrated and the wavefront distorted then the spots will move and the relative displacement is related to the sampled wavefront. This is commonly referred to as measuring the slopes.

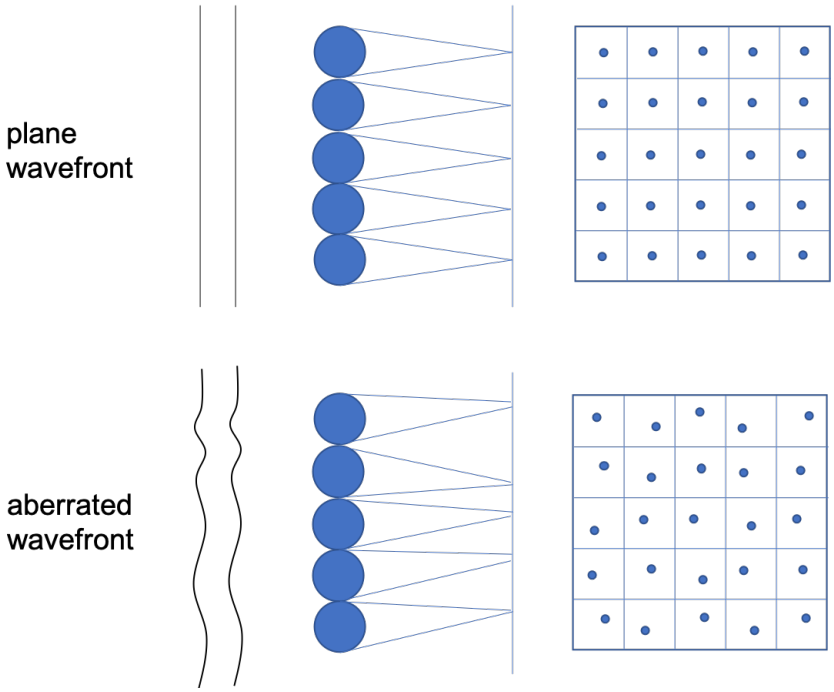


Figure 1.2: Top: Shack Hartmann wavefront sensor with plane wavefront input. As the wavefront is flat each microlens focusses the spot to the centre of the subaperture. Bottom: Shack Hartmann wavefront sensor with aberrated wavefront input. The local gradient of the wavefront causes the focussing beam to bend resulting in non-centred spots.

Spot position is measured by determining the centroid by a centre of gravity measurement related to the values measured in the pixels for each subaperture. The centroid is determined by

$$c_a = \frac{\sum_{i,j} a_{i,j} I_{i,j}}{\sum_{i,j} I_{i,j}} \tag{1.10}$$

where $a_{i,j}$ is the pixel position in dimensions x and y, and $I_{i,j}$ is the intensity measure in the pixel.

The number of subapertures in a SHWFS is an essential part of the AO system design. The number of subapertures dictates the scale of turbulence that can be measured by the system. Each lenslet will result in the average slope across the subaperture being measured. If the microlens array is projected onto the primary mirror the pitch of each subaperture represents the smallest $r_0$ which can be measured by the AO system. Although more subapertures can be used to sample smaller scale turbulence

the performance may not increase as increasing the number of lenslets reduces light in each subaperture. With the same amount of light spread across more subapertures there is a lower signal to noise ratio at each spot resulting in a greater error in the centroid measurement.

### 1.3.2 Deformable Mirrors

The deformable mirror (DM) is a principle component of an AO system which is responsible for applying the correction to return a flat wavefront. A DM can change the mirror surface shape through a grid of controlled actuators attached to a thin flexible membrane which has a reflective coating.

There are several different DM technologies available which include; voice coils, piezoelectric, micro-electromechanical systems (MEMS), and biomorph. Each technology has strengths for specific parameters and the selection of a DM is dependent on the requirements of the system. DMs can also be made with a continuous face sheet or a segmented one where segments can operate independently from one another.

Commonly used DM technologies are MEMS and voice coils. The MEMS DMs can typically be produced with small pitch (interactuator spacing) and they can operate very quickly. The downside of these DMs is the small stroke available, which is the amount the actuators can push the mirror surface. This can mean that low order aberrations such as tip and tilt cannot be effectively compensated with these DMs. A voice coil DM can be made with large stroke and larger pitch but have lower bandwidth than a MEMS DM. Figure 1.3 shows an example of a voice coil DM.

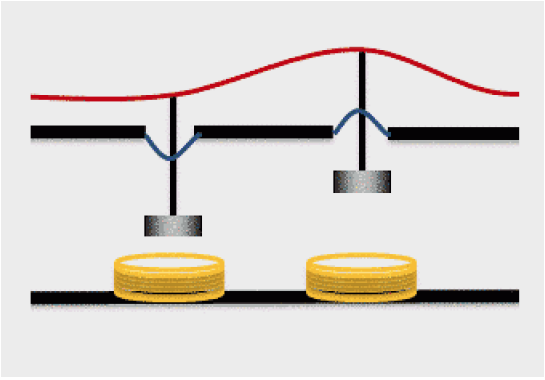

Figure 1.3: Voice coil DM. The voice coils apply a magnetic field to each actuator causing them to push or pull the flexible reflective surface. Image credit: ALPAO

When a DM is used with a SHWFS the optimum arrangement is Fried geometry where the DM actuators are mapped to the corner of each lenslet in the SHWFS [Fried, 1977]. Therefore, the number of actuators across the DM pupil will determine the number of subapertures across the SHWFS.

### 1.3.3 Wavefront Reconstruction

The wavefront that is measured by a WFS must be appropriately transformed to obtain commands for the DM actuators. The slopes s measured by the WFS can be related to DM commands by

$$s = IM \times u \tag{1.11}$$

where IM is the interaction matrix and u is the DM command vector. The interaction matrix is a characterisation of the influence that each DM actuator has on the slope in every subaperture in the WFS. Given the nature of a SHWFS there will be more actuators than there are subapertures so the interaction matrix will have dimensions m×n where m is the number of actuators, n is the number of subapertures, and m >n. An interaction matrix can be generated by individually poking each actuator in the DM and measuring the response of the WFS. The DM command matrix can be retrieved by inverting the interaction matrix.

The interaction matrix is not square; therefore, singular value decomposition (SVD) is used to invert the interaction matrix. SVD is a mathematical method to compute the pseudoinverse of a non square matrix. The interaction matrix can be represented by

$$IM = USV^T \tag{1.12}$$

where U and V are orthonormal matrices and S is a diagonal matrix containing the eigenmodes of the interaction matrix. When computing the command matrix the modes are filtered to remove modes with small eigenvalues. A threshold value can be set such as eigenvalues that are >10% of the largest eigenvalue are used. The DM command matrix is then

$$IM^{-1} = VS^{-1}U^T \tag{1.13}$$

### 1.3.4 Imaging

A portion of the corrected wavefront that is not sent to the WFS is used for scientific observations as shown in Figure 1.1. This corrected wavefront can be used for imaging as the resolution of the system has been improved by removing the atmospheric turbulence and there is higher detail.

In order to capture all of the detail available in an image the system must be designed so it has Nyquist sampling. The image is captured by a camera which features a 2-dimensional array of pixels. In order to preserve detail in the image the pixel density of a camera must be large enough to ensure that detail is not lost when sampling the image.

### 1.3.5 Guide Stars

The adaptive optics system requires a source in order to measure the wavefront, which is typically referred to as a guide star. The guide star has to be observed at a rate faster than the characteristic time scale $\tau_0$ and observed with sufficient signal to noise ratio, which necessitates observing a bright star. To perform a suitable correction on light from the science target the light from the guide star must pass through the same column of turbulence. If the guide star and science target have an angular separation the measured wavefront aberration and correction applied may not be correct leading to reduced performance of the AO system. The isoplanatic angle is the angular separation between two sources where the atmospheric disturbances are the same [Fried, 1982]. Figure 1.4 shows the effect of observing a guide star which has an angular separation from the science object with the wavefront distortion differing for the two objects. The isoplanatic angle is usually on the scale of arcseconds, which results in limited sky coverage in a conventional AO system [Valley, 1980].

In a standard AO system the guide star used for the AO correction will be another star, which is called a natural guide star (NGS). To increase the sky coverage of adaptive optics systems artificial guide stars have been developed, which are known as laser guide stars [Primmerman et al., 1991]. A powerful laser is propagated into the atmosphere and pointed towards the science object [Fugate et al., 1991]. There are two types of laser guide stars; Rayleigh and sodium LGS. A Rayleigh guide star will use a green or ultraviolet laser to scatter from atoms up to an altitude of 10 – 15 km. The scattered light is collected by the telescope and used in the WFS.

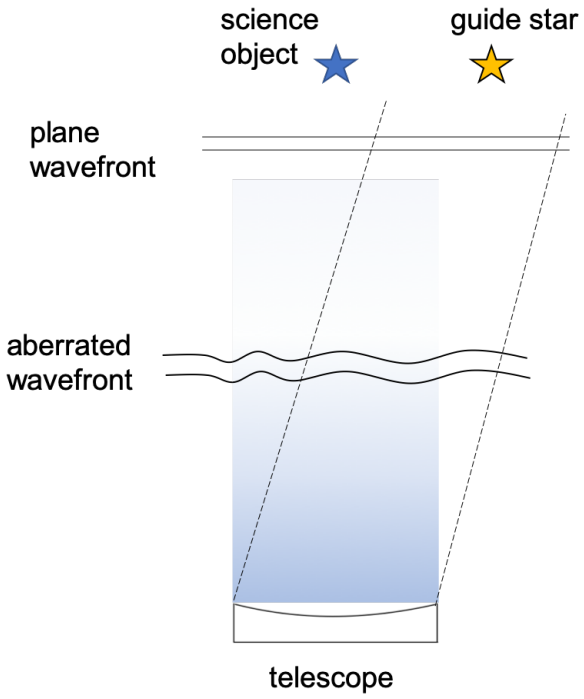


Figure 1.4: Effect of guide star with angular separation from science object. The wavefront becomes aberrated as it propagates through the atmosphere. If the guide star has a large angular separation from the science object the wavefront measured will be different resulting in error in the adaptive optics correction.

Sodium LGSs will excite atoms in the sodium layer at an altitude of 90 – 100 km [Foy and Labeyrie, 1985]. The sodium layer is formed largely due to meteor deposition and the density has a strong seasonal variation, but can also change from day to day [Hunten, 1981]. The guide star laser is specifically tuned to excite the $D_2$ line in the sodium atoms, which has a 589.2 nm wavelength [Happer et al., 1994]. The excited atoms will re-emit light at the same wavelength, which is collected by the telescope. Sodium LGSs are favoured by observatories due to improved performance over a Rayleigh LGS.

While an LGS can increase the sky coverage of an AO system there are limitations preventing full sky coverage. Tip-tilt information cannot be extracted as the upward beam experiences an unknown tip-tilt due to atmospheric turbulence so the tip-tilt introduced in only the downward direction cannot be measured from a LGS. There-

fore, a LGS AO system also requires a NGS for tip-tilt measurements. The tip-tilt measurements are made with a dedicated tip-tilt WFS which does not require as much flux as a SHWFS. The NGS does not need to be as bright as in a conventional AO system, which results in greater sky coverage.

LGS AO systems are also impacted by the cone effect as the guide star is located at a finite altitude. The light emitted from the guide star propagates through the atmosphere as a cone as illustrated in Figure 1.5. Thus, some of the atmospheric turbulence starlight experiences is not sampled by the LGS light resulting in error in the wavefront correction. The cone effect can be reduced by using a constellation of multiple LGSs to perform laser tomography, where the column of atmosphere can be measured.

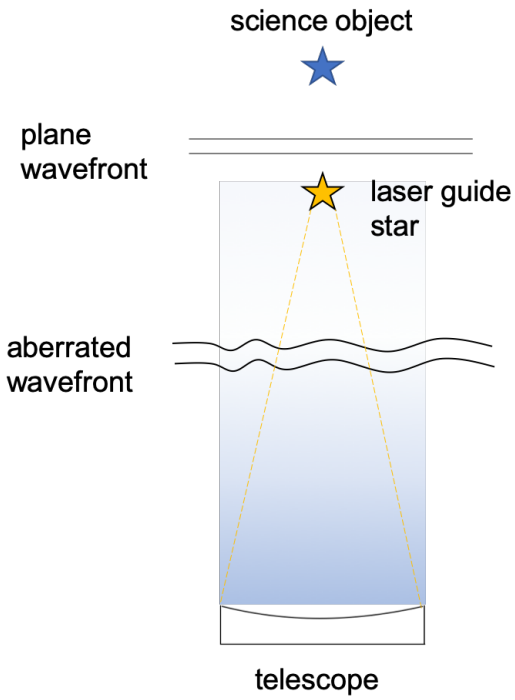


Figure 1.5: Cone effect when using laser guide star. The finite height of the guide star means the entire column of atmosphere is not measured

LGS AO systems also suffer from spot elongation on large aperture telescopes. The sodium layer is approximately 10 km in width, thus when viewing the spot off axis the LGS appears elongated. The spot in a SHWFS will become elongated in each subaperture, which causes aloss of sensitivity in the spot position measurements, and introduces error into the measurement. This is of particular concern for the ELTs, which will have much larger primary mirrors than any other in existence.

### 1.3.6 Strehl Ratio

The Strehl ratio is a measure of the performance of an optical system as it provides a metric relative to an ideal case where no aberrations occur. It is is the ratio between the peak intensity of a source through an aberrated system to the peak of an identical optical system, which has no aberrations. In telescope systems the ideal point spread function (PSF) can typically be approximated with an Airy function, which is the diffraction pattern produced by a circular aperture. Supporting structures such as the secondary mirror spider and obscuration can cause the diffraction pattern to deviate from the Airy function, however it is an appropriate approximation.

The Strehl ratio $S$ was related to the root mean square error of the wavefront $\sigma$ and can be approximated by [Mahajan, 1983]

$$S \approx e^{-\sigma^2} \tag{1.14}$$

### 1.3.7 Zernike Modes

The Zernike polynomials are a set of orthogonal polynomials which are defined on a unit circle. The Zernike polynomials have been used to describe optical aberrations and Noll was able to reconstruct atmospheric turbulence into a sum of Zernike modes [Noll, 1976]. The Zernike modes are defined by

$$\left.\begin{aligned} Z_{even,j} &= \sqrt{n+1}R_n^m(r)\sqrt{2}\cos m\theta \\ Z_{odd,j} &= \sqrt{n+1}R_n^m(r)\sqrt{2}\sin m\theta \end{aligned}\right\} m \neq 0 \tag{1.15}$$

and

$$Z_j = \sqrt{n+1}R_n^0(r), \quad m = 0 \tag{1.16}$$

where

$$R_n^m(r) = \sum_{s=0}^{(n-m)/2} \frac{(-1)^s (n0s)!}{s![(n+m)/2-s]![(n-m)/2-s]!} r^{n-2s} \tag{1.17}$$

Several of the common zernike modes are illustrated in Figure 1.6.

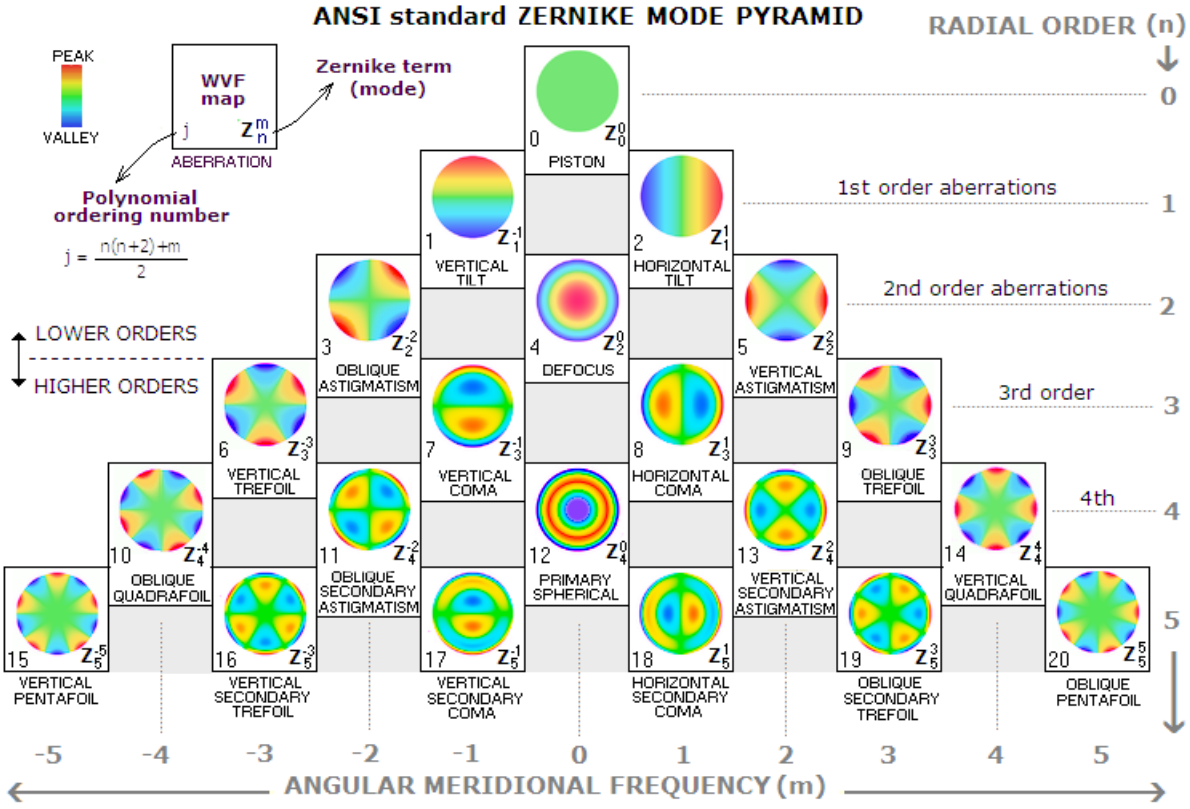


Figure 1.6: Visualisation of the first 20 Zernike modes. Image credit: Telescope-Optics

### 1.3.8 Adaptive Optics Applications

Adaptive optics was originally developed for astronomy applications but the same principles can be used for applications where a wavefront may be distorted by a turbulent medium. The techniques can be easily applied to observing non stellar sources in space such as satellites for space situational awareness (SSA) applications. Adaptive optics can be used for biomedical imaging applications such as vision, microscopy and spectroscopy. The eye can introduce aberrations due to the lens, cornea, and fluids. Adaptive optics systems can reduce the effects of these aberrations and have been demonstrated to significantly improve retinal image quality. Similarly in microscopy of biological samples refractive index variations in the surface of a sample can induce aberrations in the image and adaptive optics can be used to increase image quality.

Adaptive optics can also be used in free-space optical communications. Propagating light through free-space to transmit data will encounter the same issues as astronomical observations where atmospheric turbulence will distort the wavefront. This can lead to effects such as beam spread, beam wander, and intensity variations. All of these will reduce the reliability and data rate of a free-space link so adaptive optics is a method to improve the performance. The received wavefront could be corrected, or the transmitted laser could be pre-compensated for the atmospheric turbulence so that when the beam passes through the turbulence all the aberrations are reversed and a flat wavefront is delivered to the receiver. Free-space optical communications can be made with ground to space links or ground to ground where the beam is propagated horizontally through the atmosphere.

## 1.4 Space Situational Awareness

Space plays a critical role in communication, navigation and many other vital services, thus a secure space environment is necessary for access to these services in the future. Ever since Sputnik 1 was sent into orbit in 1957 the number of objects has dramatically increased, which has led to a crowded space environment.

### 1.4.1 Space Debris

The amount of space debris grossly outweighs active spacecraft. Spent rocket bodies, defunct satellites and fragments from breakups and collisions are spread all throughout space. These objects are referred to as debris and they pose a great risk to active spacecraft as there is no control of their trajectory. The orbits of all objects will eventually decay, causing them to fall back to Earth or burn up in the atmosphere. This decay can take years, decades, or centuries to occur depending on the orbit.

In 1978 Kessler postulated that orbits could be rendered unusable due to debris [Kessler and Cour-Palais, 1978]. If an orbit was to become too populated with debris then a single collision could cause a cascade of collisions resulting in the catastrophic destruction of all active spacecraft in that orbit. When a collision occurs pieces of the colliding objects would break off and be able to collide with other objects. This would lead to exponential growth of debris as objects continue to collide with one another[Su, 1986; Eichler and Rex, 1990]. This is known as the Kessler syndrome.

It is estimated there is more than 500,000 pieces of debris in orbit. It is difficult to know with certainty as current tracking methods only allow for larger objects to be routinely tracked and objects 1 cm or smaller cannot be tracked.

The high velocity of all objects in orbit means that even small objects pose a significant risk to spacecraft. Objects are moving at approximately 10 km/s meaning that a small piece of debris on the scale of 10 cm can cause catastrophic damage to a satellite. An example of the force that a small impact can make in a spacecraft is shown in Figure 1.7 which shows a 7 mm chip in one of the windows of the ISS by a piece of small debris. The debris is thought to be a very small metal piece (<1 mm) or paint flake. Small objects such as the paint flake are not tracked so spacecraft such as the ISS have significant shielding to prevent damage when collisions with small objects occur, but this shielding cannot protect against large debris.

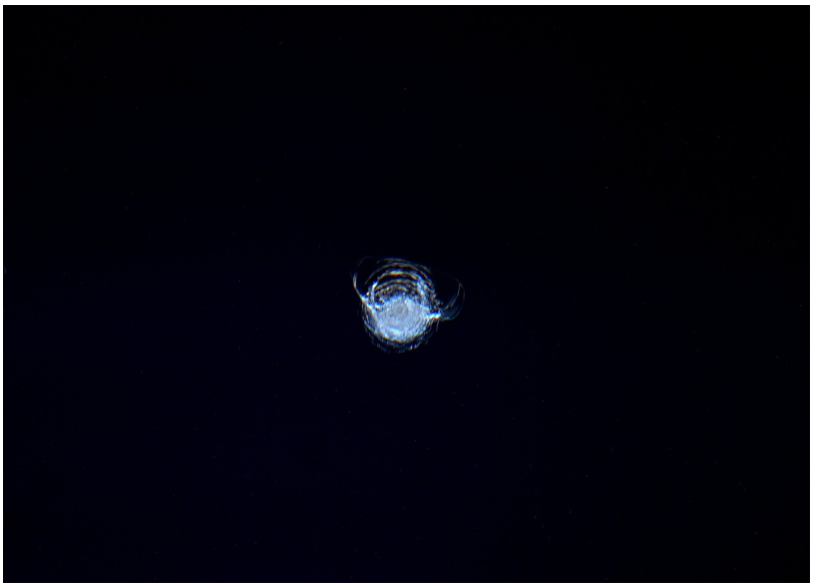

Figure 1.7: 7mm chip in ISS window due to small metal piece or paint flake. Image credit: ESA

The only method to avoid a potential collision is to perform a manoeuvre to change orbits. Routine manoeuvring to avoid collisions results in using propellant, which can reduce the operational lifetime of a satellite. Satellites have only a fixed amount of propellant to last for the mission duration, which is used to maintain orbit. Therefore, repeated manoeuvres will reduce the available propellant and operational lifetime

#### 1.4.1.1 Geostationary Orbit (GEO)

There are several orbits where there is higher risk of a Kessler syndrome developing as they offer desirable properties to satellite operators. One of the most important of these is geostationary orbit (GEO), which is a special orbit at 35,786 km. In this orbit the satellites are orbiting at the same rate as Earth rotates, so they are effectively stationary to an observer on Earth's surface. For this reason GEO satellites are used for applications such as communications and weather prediction.

Geostationary orbits are very carefully managed due to the limited space available. All satellites in the orbit must operate within a defined slot so active satellites are spaced apart. At the end of a satellites' lifetime it must move itself into a graveyard orbit so that it is removed from the GEO belt. A sudden failure or breakup may result in a GEO satellite being unable to move into a graveyard orbit and produce debris which could collide with remaining satellites in GEO. Additionally many graveyard orbits periodically pass through the GEO orbit, which presents opportunities for collisions to occur.

#### 1.4.1.2 Low Earth Orbit (LEO)

Low Earth orbit (LEO) is heavily populated with active spacecraft and debris which places it at high risk of developing Kessler syndrome. Kessler concluded that some LEO orbits were already at risk in 1991 and careful management is required [Kessler, 1991]. LEO contains many communications satellites such as the Iridium constellation and other high profile spacecraft such as the International Space Station (ISS) and the Hubble space telescope (HST). Figure 1.8 shows the population of catalogued debris increasing over time.

LEO has experienced rapid growth in the number of objects launched in recent years. This is partly due to the introduction of cubesats, which allows those who before could not afford to launch a satellite to move into space. Cubesats allow for small scale experiments and missions to be accomplished and can be launched by utilising spare payload capacity when a large scale mission is launched. The lower cost to develop a satellite and launch allows educational institutions and small companies to become players in space.

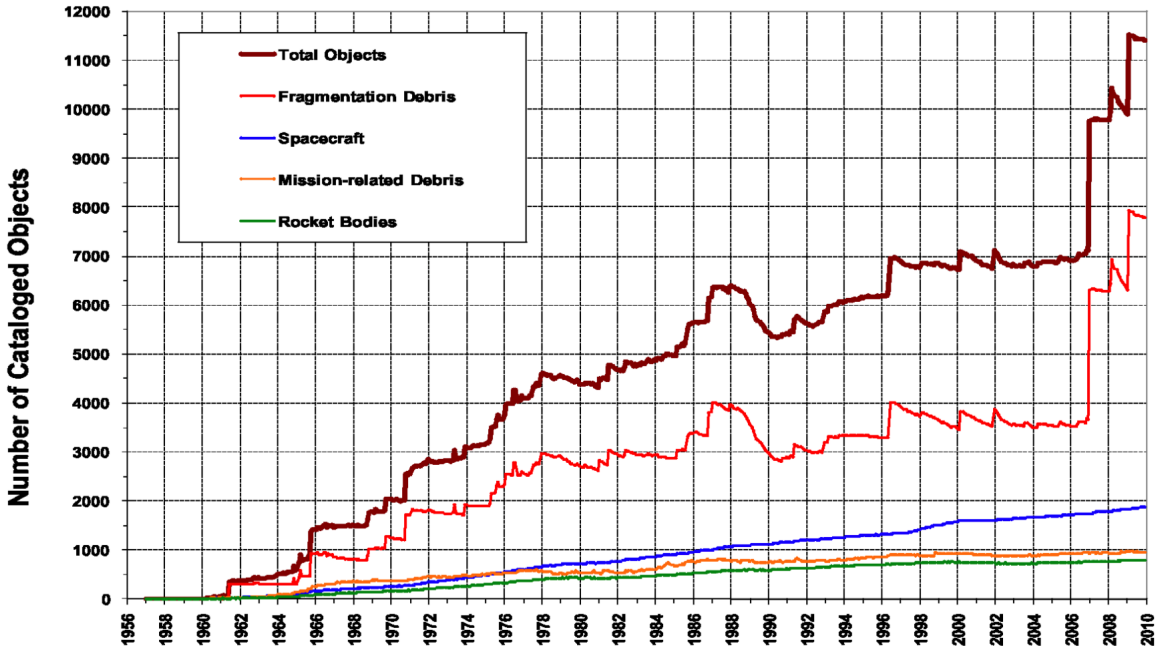


Figure 1.8: Population of catalogued objects in space as a function of time. The two sharp rises in fragmentation debris and total objects are due to the 2007 Fengyun-1C destruction and the 2009 Iridium/Cosmos collision. [Johnson, 2010]

The rise in cubesats and other small scale satellites does raise issues for space environment management. The lower cost of cubesat development can result in a higher chance of failure with less redundancy available. Failure on launch is also high for cubesats with approximately 30% failing to turn on when they are released from the rocket. There are also manoeuvring responsibility concerns as a cubesat may not have capabilities to perform a manoeuvre to avoid a potential collision. If the other object also cannot manoeuvre then a collision could occur creating debris. If the satellite can manoeuvre then the satellite has to expend fuel to ensure there is no collision, which can decrease its operational lifetime.

Several large constellations of satellites are planned for operation to provide global communications networks. These constellations will have thousands of small satellites such as cubesats that will be in similar orbits to maintain communications coverage. A rapid increase in the number of active satellites creates a greater risk for all objects within the the orbit and a collision in a densely populated constellation could result in a cascade of debris. The Starlink constellation of 60 satellites launched by SpaceX in May 2019 has had a collision warning that required the manoeuvre of

a European Space Agency (ESA) satellite in September 2019. There was a collision probability of 1 in 1,000 between ESA's Aeolus and Starlink44, and ESA decided to manoeuvre to avoid any risk to their satellite. The Starlink constellation is expected to grow to over 12,000 satellites which could result in many more of such manoeuvres to avoid potential collisions [European Space Agency, 2019].

There are two significant debris producing events that have occurred in LEO, these are the Iridium/Cosmos collision and the Chinese anti-satellite test. These two events have resulted in distinct jumps in the debris population shown in Figure 1.8.

A major debris forming event was the destruction of Fengyun-1C during an anti-satellite missile test conducted by China. The Fengyun-1C was a Chinese weather satellite that was destroyed on 11th of January 2007. The test resulted in more than 2800 pieces of debris being identified by tracking networks. This anti-satellite test was widely condemned by the international community due to the unnecessary creation of a large debris field, which compromises the safety of all operational satellites within the large debris field [Johnson et al., 2008; Liou and Johnson, 2009].

The Iridium/Cosmos collision was an accident between the inactive Cosmos 2251 satellite and an active Iridium 33 communications satellite on 10th of February 2009. The two satellites were predicted to pass closely to each other in the days before and after the collision. As the Cosmos 2251 satellite was non-operational only Iridium 33 was capable of manoeuvring to prevent a collision. Iridium 33 was not manoeuvred and the two satellites collided in what was the first instance of two satellites colliding in space. The collision speed was 10 km/s and produced a large cloud of debris with approximately 1800 new objects identified [Kelso, 2010]. The large debris field created is in a populated region of LEO and has potential to collide with other objects to create further debris [Anselmo and Pardini, 2009].

The growing number of inactive satellites is also of concern in the LEO environment. When satellites reach the end of their lifetime they are no longer manoeuvrable and pose a risk to other satellites. These satellites could collide with an active satellite similar to the Iridium/Cosmos incident where the operator does not think the collision will occur and doesn't move their satellite. There is also risk that two inactive satellites could collide, and even if the collision can be predicted nothing can be done as neither can be controlled.

Envisat is a Earth observation satellite launched by ESA in 2002 and failed in 2012. Envisat is in a 790 km altitude sun-synchronous orbit and is of particular concern due to its size and the potential damage that could occur if it collided with another object. The satellite measures $5 \times 10 \times 26$ m with the solar panel array extended and weighs in excess of 8,000 kg. A photographic render of Envisat with the solar panel array deployed is shown in Figure 1.9. Envisat will eventually fall back to Earth but is estimated to take 150 years. Due to the potential disastrous outcomes of any object colliding with Envisat missions are being considered that could deorbit the satellite to remove the risks of collisions [Phipps et al., 2012].

Figure 1.9: Envisat satellite. Image credit: ESA

### 1.4.2 Satellite and Debris Tracking

Tracking networks across the world are used to cultivate catalogues of known objects. These catalogues are constructed and maintained by government organisations and private companies. The objects are routinely tracked to update orbital models and provide conjunction assessment. Different techniques are used for tracking and their effectiveness and can be dependent on factors such as size, type of object, and distance away from the tracking station.

#### 1.4.2.1 Radar

Radar is one of the primary methods which is used to track debris by the US Space Surveillance Network (SSN). The network can track objects over 10 cm in size and with a network distributed throughout Earth all objects that can be detected are routinely tracked. New radar systems are currently being developed to increase the capability of radar tracking. The Lockheed Martin Space Fence is currently being built and once operational it is expected to significantly increase the number of known and tracked debris objects [**?**]. It is expected that Space Fence could reveal 100,000s of new objects that previously were not tracked.

#### 1.4.2.2 Laser Ranging

Laser ranging provides the most accurate positional measurement. There are two types of laser ranging; satellite laser ranging (SLR) and debris laser ranging (DLR). The principle behind laser ranging techniques is to use a pulsed laser to illuminate an object from the ground. Light that is reflected off the object is returned to the ground station and detected. As there are discrete pulses the time of flight of the pulse to propagate to the object and come back is known so a very accurate range can be measured. The pointing direction of the telescope is known as well as the position of the ground station, so the position of the object can be determined.

SLR systems typically offer better reliability with higher accuracy and work with lower power lasers requirements. A satellite is considered to be a cooperative object that features a retroreflector to allow for easy ranging. Satellites are usually more routinely tracked and their position can be estimated with less error, thus they will be more likely to be reacquired at their next tracking point. As a result SLR systems are able to track the positions of satellites with millimetre accuracy [Degnan, 1985].

Ranging of debris and other non-cooperative objects can be more difficult as the object may not have a retroreflector; consequently, the return signal may be very small. The term debris covers a variety of objects from small fragments broken off a spacecraft to a rocket body. The piece of debris may not be very large or reflective; therefore, to obtain a detectable return signal it must be illuminated with a more powerful laser. The addition of laser ranging to traditional tracking data has been shown to significantly increase accuracy in orbital prediction [Bennett et al., 2013].

#### 1.4.2.3 Optical Passive Tracking

Tracking an object optically passively involves measuring the light coming from the object of interest without having to provide any illumination. Direct imaging is a method used for passive tracking. When sunlight is reflected off the the object a telescope can be used to collect the reflected light and capture an image. This can limit the times when tracking is possible as the object must be sunlit, so it cannot be in Earth's shadow. Observations typically must happen at night so the signal from the object is not overwhelmed by the sky background, however there are several examples where satellites have been successfully imaged during daytime [Estell et al., 2019].

Passive tracking with imaging is routinely used to track GEO objects. The distance to the GEO belt can make active tracking techniques difficult as the return signal may be insufficient to detect. Additionally due to the distance from Earth GEO objects are usually always illuminated by the sun so they can be tracked for the entire night. Due to the size and distance, objects in GEO are dim with a brightness of magnitude 10 – 15 in the visible spectrum.

Passive optical tracking provides less accuracy than a active method such as laser ranging. Only angle information can be measured from direct imaging, while with laser ranging the range is also measured. Atmospheric turbulence will also affect imaging and will result in aberration impacting detection of the object due to low flux and the position measurement.

### 1.4.3 Debris Mitigation

Several methods have been proposed for active debris removal to reduce the risks of collisions with operational satellites [Liou et al., 2010]. Objects in very low orbits will degrade quickly due to the slowing effects of atmospheric drag, but those with higher orbits can take centuries to degrade. One solution is to send a spacecraft to capture debris, which can then be deorbited, however there are difficulties with capturing an uncooperative object without causing further debris.

Other methods proposed have been remote manoeuvre or removal using photon pressure from a laser. A sufficiently powerful laser would be capable of imparting momentum to an object, which could speed it up or slow it down to change its orbit [Mason et al., 2011; Grosse et al., 2018]. If it were slowed down enough it could also be deorbited. A high energy laser could also be used to create a plasma on the surface of debris resulting in thrust, which would slow the object down until it deorbits [Phipps et al., 2012].

### 1.4.4 Orbital Predictions

Tracking can provide very accurate position measurement at the moment an object is tracked but there must be a way to predict where the object will be sometime in the future. To make any reliable collision predictions modelling the orbit of objects and propagating the orbit forward in time is essential. The simplified general perturbations (SGP) model is one method that was developed for forward propagating an orbit [Lane, 1965]. SGP will calculate the orbital state vectors relative to the Earth centred inertial coordinate system for a given moment, which can then be stepped forward by a small time step repeatedly for future prediction. This model was first used in the 1970s [Cranford and Lane, 1969]. Today the SGP4 propagator is commonly used for orbital predictions [Vallado and Crawford, 2008]. SGP4 works using a two line element (TLE) data set originally developed to work on punch cards but now given in text format contained on two lines. The TLE contains all the information needed for propagation such as identifying information and measurements of orbit.

There are many processes that will influence the orbit and these are taken into consideration with orbital propagators. These parameters include:

- Atmospheric drag
- Solar radiation pressure
- Gravity variations
- Electromagnetic interactions
- Localised heating/cooling
- Object spin

These parameters will not be fixed over time or the same for every object meaning approximations are made to estimate the parameter values. There may be natural variations in the strength of the external forces such as the solar radiation changing with solar output or variations in the atmosphere. Additionally, the physical characteristics will affect how different forces act upon the object. Characteristics such as size, shape, orientation, mass, and material will all impact the influence of external forces and therefore must be well known in order to make a accurate prediction of the orbit [McMahon and Scheeres, 2015; Lucchesi, 2001]. Such information is not always possible without a direct measurement of the object. The satellite designer or operator may have detailed specifications of a spacecraft but this information may not be shared for commercial or strategic reasons. Additionally any debris that has been created from a fragmentation event will have unknown characteristics as it is not possible to measure this.

The cannonball model is one such approach used to measure the effect of solar radiation pressure, which assumes that the object is a spherical ball or "cannonball" [Lachut and Bennett, 2016]. With this approximation there are no effects from varying orientation so it is simpler to apply the external forces. This approach can be very accurate for geodetic satellites such as LAGEOS which is a dense ball covered in retroreflectors enabling it to be continuously ranged so precise geodetic measurements can be made [Cohen and Smith, 1985].

Figure 1.10: LAGEOS satellite used for geodesy. Image credit: NASA

### 1.4.5 Adaptive Optics for Space Situational Awareness

Adaptive Optics in SSA applications can provide improvements over existing optical imaging and tracking systems. The removal of atmospheric distortions and image motion with AO can lead to more accurate measurement of position, and allow for dimmer objects to be detected as the light is concentrated into a smaller area. Using AO and a high resolution imaging system as proposed in AOI can allow specific features of satellites in LEO to be resolved, and the characteristics used to feed into orbital models to improve accuracy [Fruh et al., 2013].

There are some unique challenges in designing an AO system for SSA compared to astronomy purposes. When looking at a LEO object there are no stars to use as a guide star as the object is moving quickly across the sky. A laser guide star may be used, however the object must also be used as the NGS [Hart, 2018]. Additionally, the telescope must be capable of tracking quickly and smoothly to follow the object [Fugate, 2003]. The AO system must run faster as the slew rate of the telescope is increased to follow the LEo object as the turbulence is changing at a faster rate. Therefore, AO systems designed for SSA applications require multiple kilohertz loop speed to provide a suitable correction for LEO objects.

## 1.5 Turbulence Profile Measurement with SCIDAR

Knowledge of the atmospheric turbulence strength at a site guides the design of an adaptive optics system. Layers of the atmosphere where the bulk of the turbulence is located can be identified, and the strength of the total turbulence can be measured with site characterising instrumentation. If the AO system is conjugated to multiple layers then the turbulence profile knowledge can guide the layers of the atmosphere, which the deformable mirrors should be conjugated.

SCIntillation Detection And Ranging (SCIDAR) and SLOpe Detection And Ranging (SLODAR) are two techniques that can be used for measuring the turbulence profile [Vernin and Roddier, 1973; Wilson, 2002]. In addition to adaptive optics systems for space situational awareness applications a SCIDAR system was developed to measure the turbulence at Mt. Stromlo Observatory in Canberra, Australia. This SCIDAR system is not the focus of the work completed for this thesis, but a contribution to the project has been made with some components developed for AOI utilised in SCIDAR.

A SCIDAR system uses a measurement from a binary star system to determine the location and strength of the turbulence layers. The binary stars have a known separation of $\theta$ and light from the stars pass through a layer of turbulence at height $h$, and identical measurements of the wavefront aberrations will be recorded at $d = h\theta$ on the ground. An autocorrelation of the scintillation pattern recorded on the ground will result in peaks, which correspond to the height of the turbulence layers, and the amplitude of the peaks is proportional to the strength of the layers.

A standard SCIDAR system cannot effectively measure the turbulence strength close to the ground, which is where the strongest turbulence typically exists. A generalised SCIDAR system can overcome this limitation by measuring a plane conjugated to a negative altitude, allowing the entire turbulence profile to be measured. In a generalised SCIDAR system the two pupils from the binary star are overlapping thus the scintillation pattern of the two stars is added in the overlapping region and information can be lost. Splitting the two pupils and imaging them individually can overcome this limitation and is known as stereo-SCIDAR [Shepherd et al., 2014]. Stereo-SCIDAR systems usually require two detectors, one for each of the split pupils. The SCIDAR system developed for site measurements of Mt. Stromlo uses generalised SCIDAR, will be upgraded to a stereo-SCIDAR with a single detector. The upgrade is possible by adding a roof prism in the focal plane of the instrument. This prism separates the two fields into two separate beams that are no longer overlapping but can be imaged on the same detector as shown in Figure 1.11.

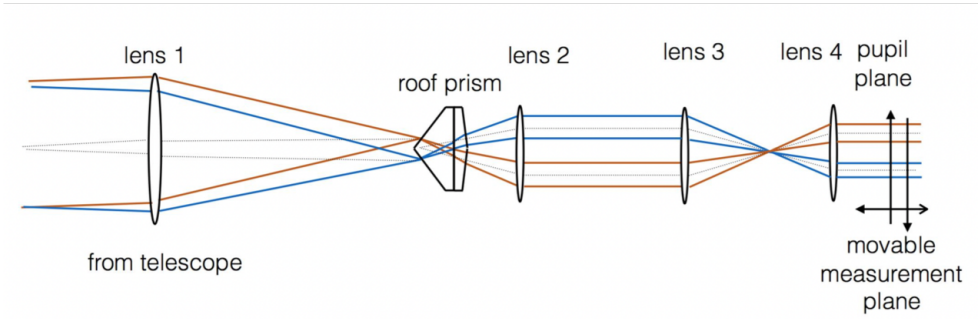


Figure 1.11: Optical layout of stereo-SCIDAR. The roof prism is placed in the focal plane and separates the two fields, which are relayed to a pupil plane where the scintillation pattern of each pupil can be recorded without overlap [Grosse et al., 2016]

Chapter 2

# Requirements and Design Specifications

Design of an AO system is dependant on the fixed parameters such as telescope specifications, and the expected performance of the system. This chapter details the requirements of the system and the specifications derived to meet those requirements. There are several key elements to AOI that influence and constrain the design choices that can be made. The telescope is a fixed system and the specifications such as the primary mirror diameter and coudé path diameter will influence the AO system requirements.

Selection of three key components are detailed in this chapter. They are the deformable mirror, wavefront sensor camera, and imaging camera. These items have significant cost compared to the rest of the AO system and are chosen to best meet the performance goal of AOI and then the rest of the system is designed around these components.

## 2.1 Telescope Specifications

The EOS deep space tracking 1.8 m telescope is used for AOI. The telescope has a primary mirror diameter of 1752 mm (1.8 m) and a 251 mm diameter secondary mirror. The secondary mirror collimates the beam, and the beam interfaces with instruments via a coudé path. The specifications of the telescope are shown in Table 2.1.

Table 2.1: Telescope Specifications

| Description | Specification |
|---|---|
| Primary mirror diameter | 1.752 m |
| Secondary mirror diameter | 0.251 m |
| Telescope magnification | 6.98 |
| Secondary obscuration | 14.3% |
| Coudé path length | 20 m |

The coudé path leads to a clean room where instruments can be kept in gravitationally invariant and environmentally stable conditions, which allows for simpler mechanical design. The optical path of the telescope and coudé path is shown in Figure 2.1.

## 2.2 Coudé Path Interface (Beam Expander)

As the beam is collimated by the telescope secondary mirror the incoming beam to the instrument will be 251 mm in diameter. Such a large diameter beam is not practical to work with in an instrument and must be reduced to a more suitable size. Thus a beam expander is required to reduce the size of the beam to one that will work with standard sized optics.

The beam expander has the following requirements:

- Output beam is the same size as the deformable mirror clear aperture – A requirement that the beam size is the same as the deformable mirror aperture means that further optics are not required to relay the beam onto the DM.
- Pupil position is sufficient distance from the final optic in the beam expander – The DM must be placed within a pupil plane, that is a conjugate plane to the telescope primary mirror. The requirement for a specific distance to the pupil plane is to allow the reflected beam from the DM to be picked off without vignetting the incoming beam. The DM is to be placed at a shallow angle of $16^{o}$ to reduce asymmetry in the projection of the beam on the DM.
- Physical dimensions that fit within the available bench space – An optical table with dimensions $1200 \times 1800$ mm is available for the AOI system. The beam expander must fit on the table.

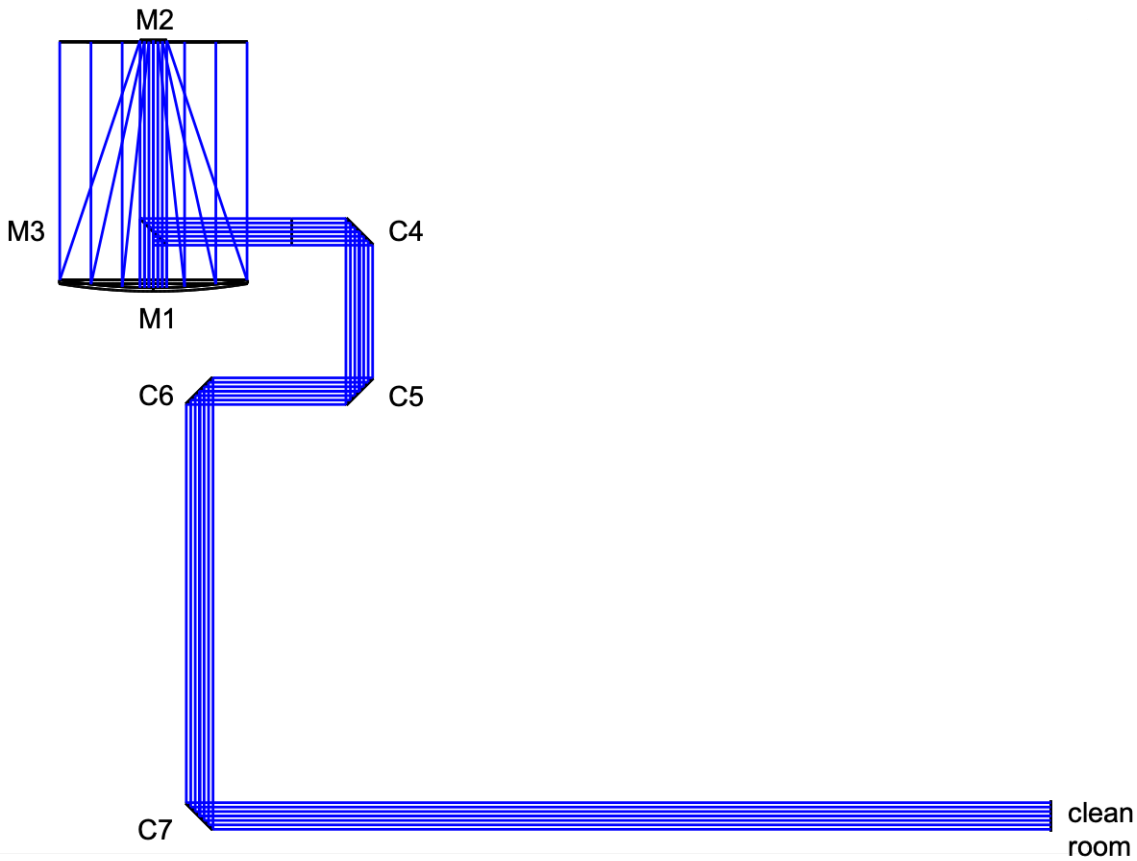


Figure 2.1: Optical path of telescope to clean room. The 1.8 m primary mirror (M1) collects light from the objects of interest. The secondary mirror (M2) collimates the converging beam to a 251 mm diameter beam and reflects the beam to the tertiary mirror (M3), which folds the beam along the elevation axis of the telescope. The fold mirrors C4 - C7 take the beam to the clean room

- No significant optical aberrations introduced – Geometric and chromatic aberrations will reduce the performance of the adaptive optics correction.

### 2.2.1 Pupil Position

The DM will be angled at a maximum of 8 degrees to avoid an elliptical spot over the DM aperture. As the angle is small a large distance is required to allow the reflected beam to clear the final optic in the beam expander. If the final lens in the beam expander is assumed to be a 2 inch optic the centre of the reflected beam must be more than 35mm from the centre of the incoming beam to allow for clearance of

the lens mounts. The distance (d) between the incoming and reflected beams can be estimated by

$$d = x \tan 2\theta \tag{2.1}$$

where x is the distance along the optical axis and $\theta$ is the angle of the DM. If the distance between the centre of the beams is to be 35 mm and the DM is angled at 8 degrees the pupil must be 122 mm from the final optic. Therefore, the pupil must be greater than 122 mm from the final optic to allow the DM to be placed in the system without a relay.

## 2.3 Adaptive Optics

### 2.3.1 Deformable Mirror

The choice of deformable mirror determines how many actuators are projected across the primary mirror pupil. In general the design of the adaptive optics system uses Fried geometry, where a DM actuator is mapped to the corner of a subaperture in the wavefront sensor. The deformable mirror will be responsible to correct tip-tilt aberrations so a high stroke DM is needed. In order to provide sufficient stroke voice coil actuator DMs are the most appropriate technology to use. Therefore, the DM selection was on the range available from ALPAO. RSAA has previous experience with ALPAO DMs having developed previous AO systems using ALPAO deformable mirrors. This previous experience provides confidence in the performance of the DMs meeting the necessary requirements and will reduce the time and effort required to develop software and control for the DMs.

The number of actuators across the telescope pupil will determine the scale of turbulence that can be corrected by the adaptive optics system. This can be viewed as the smallest $r_0$ with which the system will be effective. At the time of AOI design no extensive survey of the site conditions had been performed. However, from experience operating systems at Mt. Stromlo Observatory we found seeing conditions of around 2 arcseconds were a reasonable assumption. Such seeing conditions translate to an $r_0$ value of 11 cm. If the WFS subapertures are projected onto the telescope primary mirror with an 11 cm size then 1752/110 = 16 subapertures are required for the system. If the AO system utilises Fried geometry then a 17×17 grid of actuators is required for the DM.

The assumption of 2 arcsecond seeing at Mt. Stromlo Observatory is the upper limit that the AO system will be able to provide a reasonable correction. Seeing conditions can be much worse, and instances of 4 arcsecond seeing has been experienced. In situations where the seeing is worse than 2 arcseconds operations of AOI will not continue as the AO system is not effective.

#### 2.3.1.1 DM Options

Given the expected site conditions at Mount Stromlo Observatory two DMs have been considered as possible choices for the AOI system. They are the ALPAO DM277 and ALPAO DM468. These two DMs are very similar in performance and share a common construction, but the DM468 has a larger actuator grid. The specifications of the two DMs considered for AOI are listed in Table 2.2.

Table 2.2: Specifications of ALPAO DM277 and DM468

| Specification | DM277 | DM468 |
|---|---|---|
| Actuators | 277 | 468 |
| Pitch (mm) | 1.5 | 1.5 |
| Pupil diameter (mm) | 24.5 | 33 |
| Actuator grid | 17×17 | 22×22 |
| Tip-tilt stroke (µm) | 15 | 15 |
| Settling time (µs) | 500 | 500 |

The DM277 meets the requirements to perform corrections in 2 arcsecond seeing or better. The DM468 was considered to allow the system to operate in less favourable conditions. With a 22×22 actuator grid the WFS subapertures would be 8.3 cm in size.

#### 2.3.1.2 Simulations

Simulation of the AO system for AOI have been conducted and the outcomes of the simulations provide information on the best suited DM for the system. The AO system was simulated with two DMs, the DM277 and DM468.

The conclusions of the simulation regarding the DMs was there was no benefit to performance to use the DM468 over the DM277. The DM468 has more actuators and ideally it should provide an improved correction over the DM277 due to the poor seeing conditions at Mt Stromlo. However, the larger number of actuators requires more subapertures in the wavefront sensor; therefore, the signal for each subaperture at the wavefront sensor detector is decreased. The effect of increasing the number of subapertures is to decrease the signal to noise ratio (SNR) at the wavefront sensor, which reduces the performance of the AO system. The reduction in SNR with the DM468 caused lower performance compared to the DM277 system, leading to the recommendation for the DM277.

#### 2.3.1.3 Optical Design

The higher actuator count of the DM468 presents additional challenges in the design of the wavefront sensor. The wavefront sensor camera has a 240×240 pixel detector, which will limit the number of pixels available for sampling each subaperture to 10×10 pixels (including one guard pixel). If a microlens array of 300µm pitch is chosen, a relay between the microlens array and camera will be required to reduce the beam size to obtain the correct sampling. The inclusion of a relay in not desired as it adds further optics to the system.

#### 2.3.1.4 DM Choice

The ALPAO DM277 is recommended for purchase as the deformable mirror for the AOI system. Simulations of the system have shown that the DM277 will provide increased performance over the DM468 due to higher signal to noise in the wavefront sensor. The DM277 also provides fewer design challenges, and allows for more flexibility in the wavefront sensor design as more pixels are available to sample each subaperture. The DM277 is also the cheapest of the two DMs considered for the system. The DM277 will cost approximately $80,000 AUD less than the DM468, which provides a significant saving.

### 2.3.2 Wavefront Sensor

The wavefront sensor design is a Shack Hartmann featuring a microlens array and high performance camera. The camera used for wavefront sensing was set before design as the OCAM 2k EMCCD camera from First Light Imaging. The WFS camera was fixed and the WFS was designed to suit the camera specifications. This was done for two reasons:

- Cost – The camera is very expensive to purchase, approximately $250,000 AUD. The camera had been purchased for a similar project and was available for use; therefore, using the OCAM 2k added no extra cost to the project.

- Performance – The OCAM 2k is the most suitable camera for the intended application of satellite imaging. The camera is capable of operating at the full 240×240 pixel frame at a rate of 2 kHz with very low noise. No other camera is capable of the same performance making the OCAM 2k the ideal choice for the AOI WFS.

The specifications of the OCAM 2k are described in Table 2.3.

Table 2.3: First Light OCAM 2k Specifications

| Description | Specification |
|---|---|
| Frame size | 240 × 240 |
| Pixel size | 24 $\mu$m |
| Frame rate (full frame) | 2067 Hz |
| Readout noise | 0.3 $e^-$ |
| Dark current | <0.01 $e^-$/pix/frame @ -40$^o$C |

Selection of the microlens array to make the Shack Hartmann wavefront sensor will depend on two variables, the pitch and radius of curvature of each lenslet. To go directly from the microlens array to the WFS camera with no magnification a pitch of no more than 360 µm is required. For cost reasons a COTS microlens array is preferred as an available COTS component will be an order of magnitude cheaper to purchase. A COTS microlens array with 360 µm pitch could not be found; however, 300 µm pitch microlens arrays are easily available with suitable radius of curvature.

With a 300 µm pitch a 12.5×12.5 pixel region will sample each subaperture which can be expanded to 13×13 pixels per subaperture by slightly defocusing the camera. The defocussing does not affect the performance of the WFS but allows an integer number of pixels per subaperture.

AOI operates in the visible spectrum and the OCAM 2k uses a silicon detector so visible light must be used on the WFS. To ensure sufficient flux on the camera to measure the wavefront 450 – 800 nm light will be used on the WFS.

## 2.4 Imaging

The imaging camera is used to capture images of the object that has been corrected by the AO system. The requirements for the imaging camera are

- Nyquist sampling of a diffraction limited spot
- Frame rate of at least 30 Hz for lucky imaging with goal of 60 Hz
- Large field of view for quick acquisition
- Low noise

The WFS is operating with a wavelength range of 450 – 800 nm so these wavelengths cannot be used for imaging. Imaging can be performed for >800 nm wavelengths. While the quantum efficiency of a silicon detector is lower for NIR wavelengths it is still acceptable over a range of 800 – 950 nm.

Nyquist sampling a diffraction limited spot requires a 2×2 pixel region across the spot FWHM. Assuming the diffraction limited is set by the telescope then at 800 nm imaging wavelength the diffraction limit is

$$\frac{\lambda}{D} = \frac{800\times10^{-9}}{1.752} = 4.56 \times 10^{-7} rad$$

This is equal to 0.094" so the plate scale of the imaging system to achieve Nyquist sampling is 0.047"/pixel.

The requirements for the imaging system are difficult to meet due to practicality restrictions. The requirement for Nyquist sampling determines the plate scale or field of view of each pixel in the detector. As this plate scale is small the only way to achieve a large field of view is by using a camera with a large number of pixels. However, a large sensor typically has to readout slowly to reduce readout noise, which

is not possible due to the speed requirement of the system. The sampling, frame rate, and noise requirements are essential for system performance and therefore are prioritised in the design. Methods for acquisition can be achieved in different ways such as a dedicated camera system with a large field of view.

Electron Multiplied Charged Coupled Devices (EMCCDs) are the most suitable camera type for the requirements of AOI. They are capable of sensing very faint signals with extremely low noise and fast frame rates. There are several manufacturers of EMCCD cameras; however, the product lines are identical as they all make cameras using chips from e2v. Therefore, specifications such as pixel size and frame size are the same with small differences in the noise and speed based on the manufacturers' implementation.

There are therefore three different camera sizes considered for the imaging of AOI as shown in Table 2.4. It is noted that the OCAM 2k camera is not considered due to its high cost.

Table 2.4: Camera Specifications

| Specification | 1 | 2 | 3 |
|---|---|---|---|
| Frame size | 128×128 | 512×512 | 1024×1024 |
| Pixel size | 24 µm | 16 µm | 13 µm |
| Frame rate (full frame) | 1000 Hz | 60 Hz | 30 Hz |

### 2.4.1 Imaging Field of View

The field of view (FOV) of the imaging camera is an important consideration. Satellite tracks contain error as they are based on a prediction from the last time it was actively tracked. Therefore, it is necessary to have a large FOV to assist in quick acquisition. When viewing low Earth orbit satellites they are only visible for 10 minutes or less so fast acquisition is necessary. The angular FOV of AOI translates to a searchable area at different altitudes, which are shown in Table 2.5.

Table 2.5: Searchable area within imaging FOV

| Altitude (km) | 25" | 75" |
|---|---|---|
| 500 | 55 × 55 m | 183 × 183 m |
| 800 | 87 × 87 m | 293 × 293 m |
| 1,000 | 110 × 110 m | 366 × 366 m |
| 36,000 | 3,944 × 3,944 m | 13,177 × 13,177 m |

The imaging camera for the AOI system is used for imaging satellites in low Earth orbit (LEO) and geostationary orbit (GEO). Objects are imaged using reflected sunlight, thus imaging is conducted with visible and near infra-red light.

The requirements of the imaging camera are summarised in Table 2.6.

Table 2.6: Requirements of the Imaging Camera

| Specification | Requirement |
|---|---|
| Readout noise | <1 $e^-$/pixel |
| Frame rate | >30 Hz |
| Pixel size | >10 µm |
| Field of view* | >20" |

* This requirement is for field of view with Nyquist sampled images.

### 2.4.2 Camera Options

The requirement for a low noise and high speed camera operating in the visible spectrum limits the possible camera options. The detector type best suited to these requirements is an EMCCD, which are able to image with very low readout noise and dark current, and high frame rates.

Improved performance from an EMCCD camera can be achieved by using a camera with an e2v sensor. Cameras with e2v sensors are available in 128×128, 512×512, and 1024×1024 pixels sizes from various manufacturers. As the same sensors are used in the cameras prices are very similar for all vendors. Performance is also similar between cameras of different vendors, with some minor differences due to different parameters, which are optimised by the manufacturer.

The First Light Imaging OCAM 2k EMCCD camera that will be used in the WFS was also considered. This camera has a 240×240 pixels sensor and can operate up to 2 kHz, which is significantly greater than the speeds of the other cameras considered. The required frame rate for the imaging camera is between 30 and 60 Hz so the faster speed provided by the OCAM 2k is not needed. As the OCAM 2k is also significantly more expensive than the other cameras considered for comparison, it is therefore not suitable as the imaging camera.

### 2.4.3 Optimum Camera Frame Size

There are three frames sizes which can be chosen, 128×128, 512×512, and 1024×1024 pixels. The choice of the best frame size will depend on which camera can provide a sufficient field of view and fast frame rate. Large field of view requires a high number of pixels; however, the frame rate decreases with the number of pixels, which must be read out. Therefore, a trade off between field of view and frame rate is required and the camera offering the best balance between the two parameters will be most suitable.

#### 2.4.3.1 Field of View

The maximum field of view is obtained by using all pixels available in the camera. In order to capture Nyquist sampled images at 800 nm the imaging plate scale must be 0.047"/pixel. The requirement for the field of view when Nyquist sampling is 20"; therefore, the minimum frame size to meet the field of view requirement is 400×400 pixels.

This frame size eliminates the 128×128 pixel sensor size from consideration. Both the 512×512 and 1024×1024 pixel cameras are acceptable to achieve the minimum field of view requirement.

#### 2.4.3.2 Frame Rate

The frame rates for the cameras will vary with the region of interest (ROI) chosen. Fewer pixels in the ROI results in faster frame rates. A comparison of frame rates for 512×512 and 1024×1024 pixel cameras is performed using Nuvu HNu 512 and HNu 1024 cameras. Table 2.7 lists the maximum possible frame rates for the Nuvu HNu 512 and HNu 1024 with different regions of interest. Similar rates are achieved with other cameras considered.

Table 2.7: Frame Rates for Camera ROI

| ROI | HNu 512 | HNu 1024 |
|---|---|---|
| 1024×1024 | N/A | 16.7 Hz |
| 512×512 | 63 Hz | 32.7 Hz |
| 256×256 | 124 Hz | 62.7 Hz |

The frame rate of the HNu 1024 is limited to 16.7 Hz when imaging with the full frame. As the requirement for frame rate is at least 30 Hz, the 1024×1024 camera would need to be windowed to a 512×512 ROI to meet this requirement. By windowing down to a 512×512 ROI the possible FOV using each detector would be the same. Given that the HNu 512 can operate at nearly double the frame rate compared to the HNu 1024 it is favourable to select the 512×512 camera.

### 2.4.4 Discussion

With the field of view and frame rate requirements for AOI the most suitable camera for the imaging is an EMCCD with 512×512 pixel frame size. For all cameras considered a 512×512 ROI is the largest possible frame capable of imaging at a frame rate of at least 30 Hz. This frame size also provides a Nyquist sampled field of view of 25", which exceeds the requirement of 20".

Although the 512×512 camera and 1024×1024 camera, windowed to 512×512, can both meet the requirements for AOI it is recommended the 512×512 is purchased. The 512×512 camera can operate at a much faster frame rate, which provides flexibility during operation as the frame rate can be increased if needed. The pixels in the 512×512 camera are also larger at 16 µm compared to 13 µm for the 1024×1024 camera.

### 2.4.5 Camera Survey

There are multiple 512×512 pixel EMCCD cameras available. Three cameras are considered for comparison: The Nuvu HNu 512, Andor iXON Ultra 897 and Princeton Instruments ProEM-HS: 512BX3. These cameras have been previously considered for purchase by the RSAA AO group, and quotes have been obtained for each.

#### 2.4.5.1 Specifications

The key specifications of each camera is listed in Table 2.8.

Table 2.8: Camera Specifications

| Camera | Nuvu HNu 512 | Andor iXON Ultra 897 | Princeton Instruments ProEM-HS: 512BX3 |
|---|---|---|---|
| Pixels | 512×512 | 512×512 | 512×512 |
| Pixel size (µm) | 16×16 | 16×16 | 16×16 |
| EM gain | 5000 | 1000 | 1000 |
| Readout noise ($e^-$) | <0.1 | <1 | <1 |
| Dark current ($e^-$/pixel/second) | 0.0002 | 0.001 | 0.001 |
| Clock induced charge ($e^-$/pixel/frame) | 0.001 | 0.0018 | 0.002 |
| Frame rate at full frame (Hz) | 63 | 56 | 61 |
| Interface | Camera Link | Camera Link | GigE |

The specifications listed in Table 2.8 indicate the Nuvu HNu 512 offers the best performance of the cameras considered. The Nuvu camera provides lower readout noise, dark current, and clock induced charge, which produces the lowest overall noise performance. The Nuvu camera also offers the highest speed of 63 Hz at the full 512×512 frame, thus the superior noise performance does not impact the speed at which it can operate.

The RSAA has purchased Nuvu cameras in the past and has experience in developing software to work with the cameras and interface with other systems. This experience provides increased confidence in set up, and may reduce time needed for development for AOI.

### 2.4.6 Camera Choice

The Nuvu HNu 512 is recommended for purchase as the imaging camera for AOI. The HNu 512 features a suitable sensor size of 512×512 pixels and meets the requirements of the AOI imaging camera. The Nuvu HNu 512 provides exceptional performance in two critical areas for the AOI system, noise and speed. The HNu 512 has the lowest readout noise, dark current, and clock induced charge of all cameras considered, which will allow high signal to noise ratio images to be obtained from the AOI system. Previous experience with Nuvu cameras provides confidence in the performance of the cameras and may reduce development time required to implement the camera in the AOI system.

## 2.5 Calibration

The AO system requires a calibration source for verification of alignment and calibration of the AO system. The spot from the calibration source should be 2×2 pixels in size on the wavefront sensor and imaging camera to be Nyquist sampled. The calibration source will be coupled into the system via an optical fibre and the image at the WFS and imaging camera will be an image of the core, if the image is larger than the diffraction limit spot size.

The image size needed to produce a diffraction limited spot on the WFS and imaging camera is 48 µm and 32 µm respectively. A larger core fibre may be used for alignment of AOI as more light can enter the system and the beam can be physically observed. The size of the image produced will then be

$$s_{img} = s_{obj} \frac{F_{img}}{F_{obj}} \tag{2.2}$$

where $s_{obj}$ is the fibre core diameter, $F_{obj}$ is the F number of the calibration collimating beam, and $F_{img}$ is the F number of the imaging beam.

Chapter 3

# AOI Design

This chapter details the design of AOI to meet the design requirements and scientific goals that have been outlined. The AO system has been broken down into different subsystems and the function of each subsystem in AOI is described.

The optical design of AOI will be detailed, the optical design was completed using Zemax OpticStudio to model the entire system and determine the expected performance. The optical design and optical components used for each of the subsystems is discussed. Of particular importance is the performance of the imaging subsystem, aberrations must be reduced to below the diffraction limit over the desired imaging range. To achieve diffraction limited imaging custom lenses are used in AOI, which allowed diffraction limited imaging over 800 – 950 nm and close to diffraction limited imaging for 600 – 950 nm.

This chapter will also present the mechanical design for AOI. The mechanical design is needed to determine how all elements in the system will be mounted and to ensure the system will fit within the available bench space. The mechanical design was completed in Solidworks. A complete 3D model of AOI was built, which is used to guide assembly.

During the build and operation of AOI several elements were not possible to implement due to time constraints. The elements that were not included in AOI are discussed including the impact to the performance of the system.

## 3.1 Subsystem Breakdown

AOI has been broken down into 6 subsystems as shown in Figure 3.1. The components contained in each of the subsystems is highlighted in Figure 3.2 where the optical layout of AOI is shown with boxes around each of the subsystems.

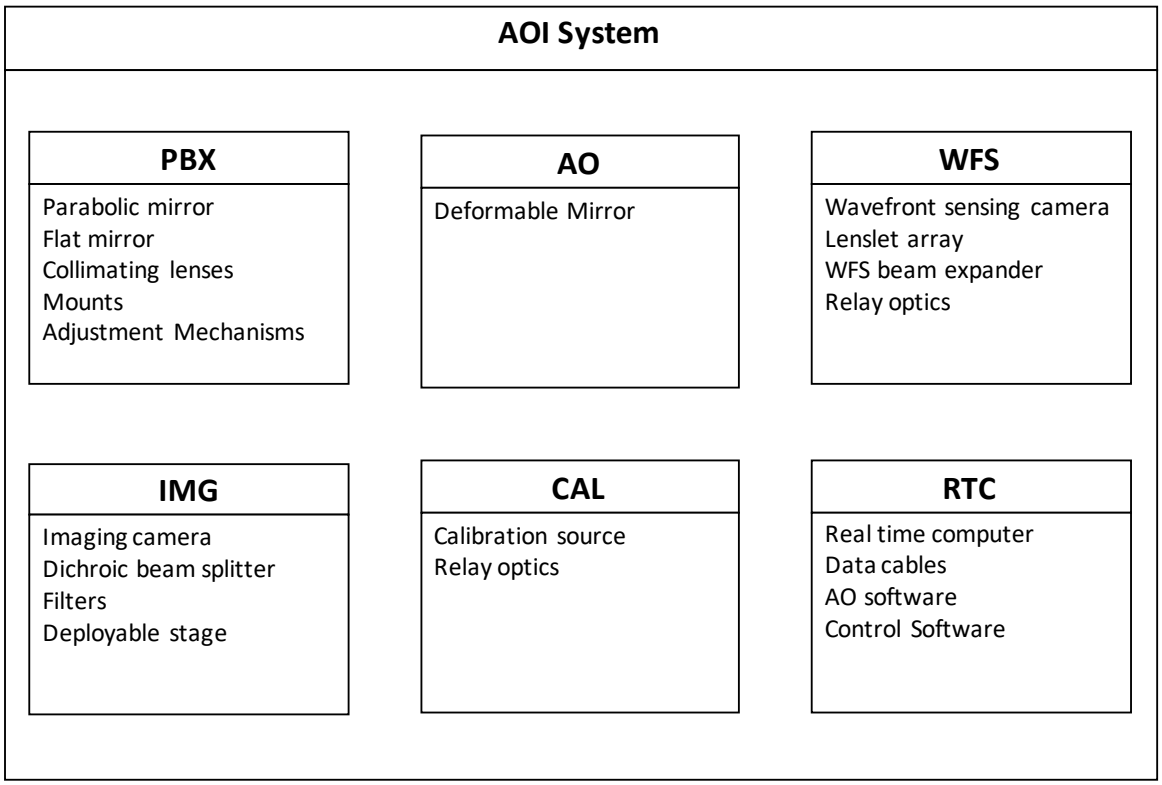


Figure 3.1: AOI Subsystem Overview

### 3.1.1 Primary Beam Expander

The primary beam expander (PBX) subsystem modifies the beam size from the coudé path to the AO system. The PBX uses a parabolic primary mirror to bring the input beam to a focus and two collimating lenses for collimating the beam at the desired size.

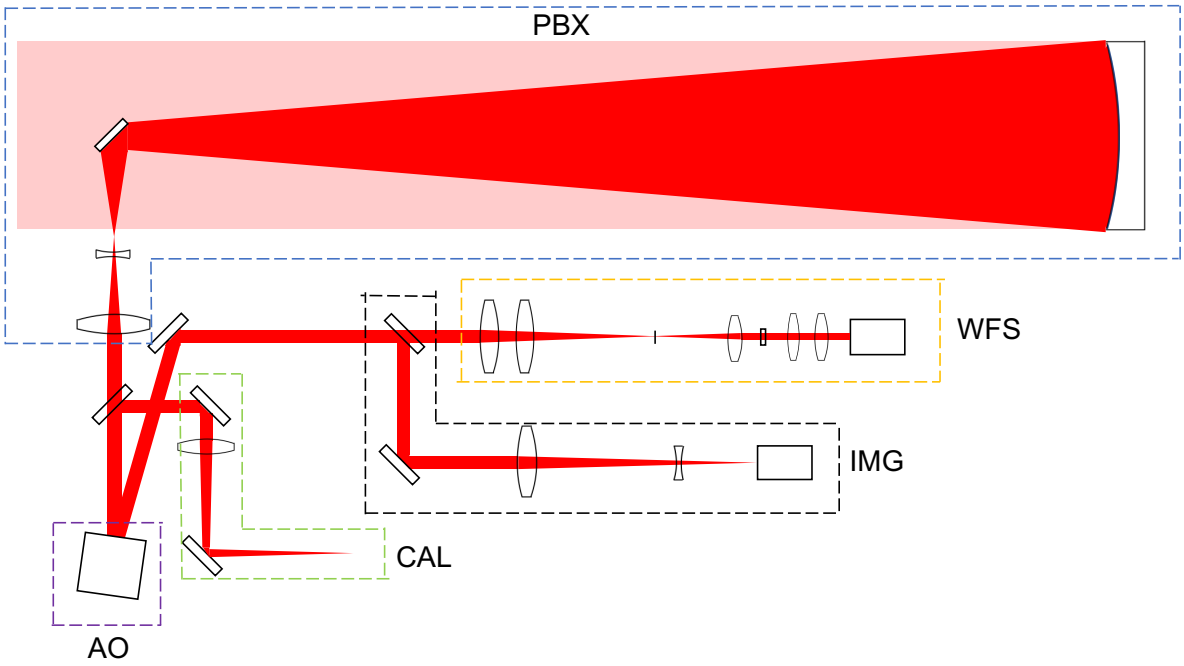


Figure 3.2: AOI Subsystem Overview

### 3.1.2 Adaptive Optics

The adaptive optics (AO) subsystem consists of the deformable mirror (DM) and fold optics required between the beam expander and imaging system.

### 3.1.3 Wavefront Sensing

The wavefront sensing (WFS) subsystem performs the measurement of the distorted wavefront. A refractive beam expander is used to modify the beam size between the DM and the microlens array. Wavefront measurements are performed with a microlens array and high speed camera.

Relay optics between the microlens array and camera may be required so the focus is on the detector plane.

### 3.1.4 Imaging

The imaging (IMG) subsystem captures the AO corrected images. A dichroic beam-splitter is used to split the light between the WFS and IMG. Filters block all wavelengths outside of the desired imaging wavelengths to cut background noise.

The imaging subsystem also includes a deployable stage that has fold mirrors and a lens mounted upon it. This deployable stage can move in an out of the beam path and is used to provide dual field of view modes while imaging.

### 3.1.5 Calibration

The calibration (CAL) subsystem is used to calibrate the AO system before operation. The calibration source is a broadband light source, which is coupled to the AO system through a collimating lens and flip up fold mirror.

### 3.1.6 Real Time Computer

The real time computer (RTC) subsystem provides the data interfaces and control for active items in the AO system. The RTC uses measurements from the wavefront sensor to provide control to the DM. The RTC subsystem is also responsible for the AO software and controlling components such as the imaging camera.

## 3.2 Optical Design

The optical design of the AOI system is detailed for the subsystems outlined in Figure 3.1. The optical design of AOI was completed using Zemax OpticStudio to model the entire system, including the 1.8 m telescope. Modelling the AOI in Zemax was performed to determine the optimal physical layout of the system and optimise the optical performance. Figure 3.3 shows a schematic of the entire optical layout of AOI.

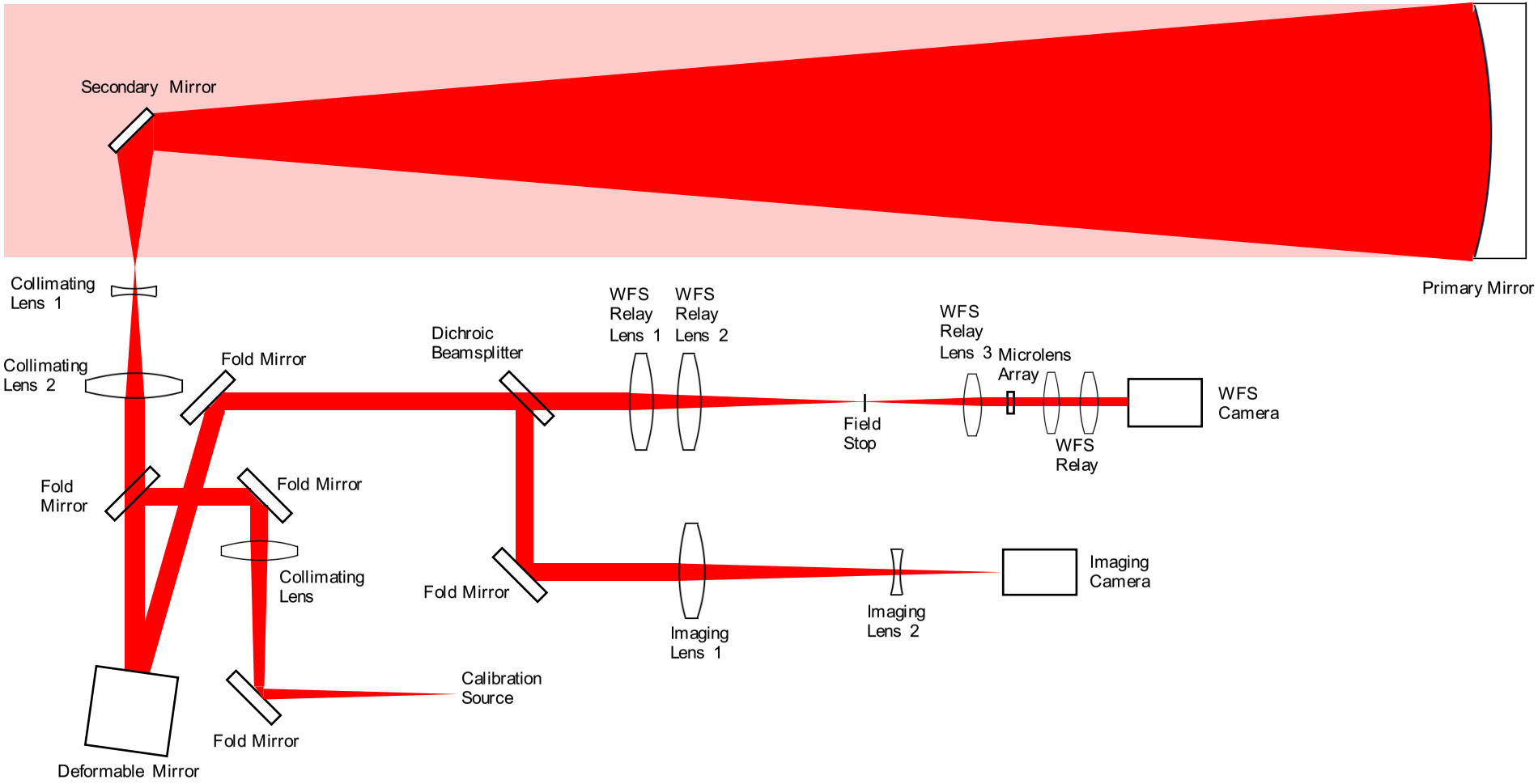


Figure 3.3: AOI optical layout. Light comes from the telescope via a 251 mm diameter coudé path. The beam is focussed by a parabolic mirror and picked off with a flat mirror at 45°. The beam is collimated by two lenses onto a deformable mirror. The light is reflected off the deformable mirror and is sent to a dichroic beamsplitter where 400 – 800 nm light is transmitted to the wavefront sensor and 800 – 950 nm light is reflected to the imaging system. A calibration beam can be coupled into the system by a flip up fold mirror which will reflect the calibration beam onto the deformable mirror and then to the wavefront sensor and imaging camera

## 3.3 Primary Beam Expander

The primary beam expander (PBX) reduces the beam size from the coudé path to the deformable mirror (DM). The design chosen is a Newtonian telescope with lenses to recollimate the beam. Several different designs were investigated such as off-axis parabolas and a Cassegrain telescope, however the design presented was chosen for simplicity and cost reasons.

The light from the coudé path is focussed by a 300mm diameter F/5.3 mirror, with a focal length of 1600mm. The beam is reflected by an elliptical flat mirror 1440 mm from the parabolic mirror. This elliptical mirror is 50×35 mm in size, which is the size of the telescope secondary obscuration. The elliptical mirror is at an angle of 45 degrees to reflect the focused beam perpendicular to the incoming beam.

After focus the beam is collimated to the deformable mirror (DM) pupil size. The magnification of the primary beam expander is 10.6. A single collimating lens of 149.8 mm focal length can achieve the magnification required for the PBX. However, with a single collimating lens the pupil is located <10 mm from the lens, where it is not possible to place the DM and therefore, a relay system would be required. To extend the pupil position after the collimating lens a compound lens system consisting of a negative lens and positive lens can produce an effective focal length of 149.8 mm and a pupil position of >200 mm. A lens system with focal lengths of f = -75 mm and f = 132 mm separated by 110 mm will produce a pupil plane 220 mm from the final lens. This pupil position is sufficient to avoid a relay system between the collimating lenses and the DM.

Each of the collimating lenses used in the PBX is custom designed achromatic doublets to reduce aberrations at the wavefront sensor and imaging camera. The radius of curvature, thickness and materials have been chosen to achieve the best possible image quality for a wide wavelength range. Acceptable performance from achromatic doublet custom lenses over a 450 – 950 nm wavelength range could not be produced. Improved performance is possible by using air spaced doublets and triplets; however, these lenses are not preferred due to high costs and tight tolerances required for the air spacing mounts. If the wavelength range is narrowed to 600 – 950 nm then custom achromatic doublets can deliver the required optical performance. Therefore, all custom lenses are designed for use with a wavelength range of 600 – 950 nm.

The layout of the primary beam expander subsystem is shown in Figure 3.4.

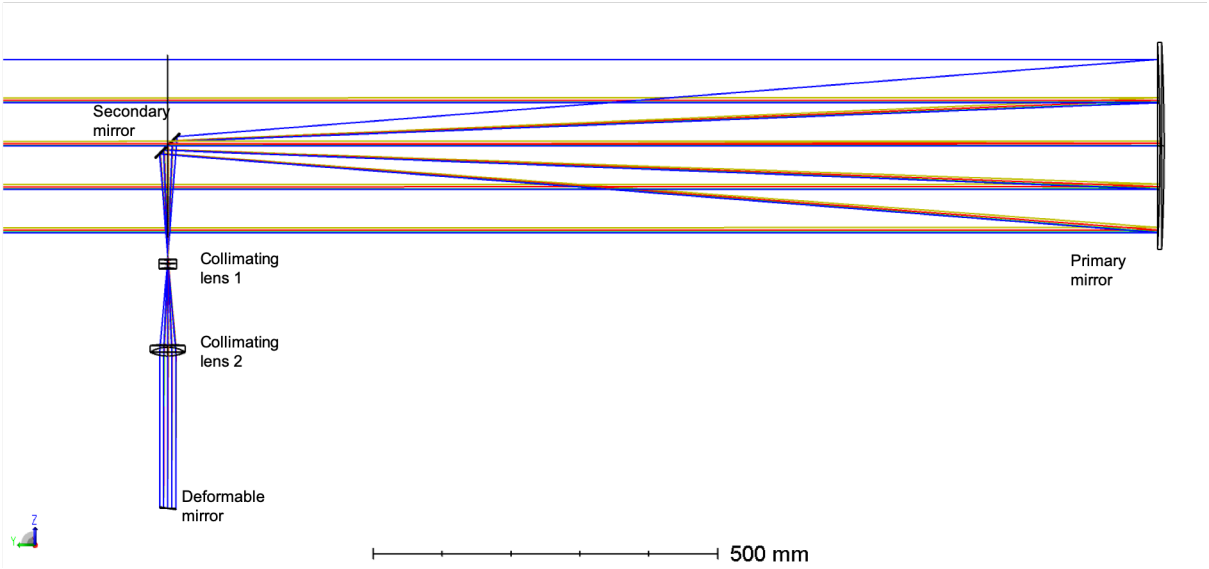


Figure 3.4: Optical layout of primary beam expander subsystem

### 3.3.1 Beam Expander Secondary Mirror

The secondary mirror reflects the focussing beam from the primary at a 45 degree angle to the AO system. As shown in Figure 3.4 the secondary is located on axis in the centre of the coudé beam.Thus it must be sized appropriately to avoid clipping the focussing beam while not cause a significant obscuration to the incoming beam.

The central obscuration of the 1.8 m telescope is 250 mm diameter, at the secondary of the beam expander this obscuration is 35 mm diameter. Therefore, if the secondary is sized at approximately 35 mm it should not cause significant vignetting to the beam from the telescope coudé path. However, as the PBX secondary mirror must be tilted at 45 degrees an elliptical mirror with a wider horizontal axis can be used without affecting the obscuration size. The maximum width is

$$width = \frac{height}{\cos\theta}. \tag{3.1}$$

With a height of 35 mm and angle of 45 degrees the width of the ellipse is 50 mm. Therefore, an elliptical mirror of 50 mm semi-major axis and 35 mm semi-minor axis could be used to match the telescope secondary obscuration.

### 3.3.2 Secondary Mirror Clipping

The secondary mirror will clip some light, with fields further off axis more strongly affected; however, the secondary should not cause significant clipping to light within the imaging field of view. Depending on the configuration the high resolution imaging field of view will lie between 22.5 and 30 arcseconds. An elliptical mirror of 50 mm semi-major axis and 35 mm semi-minor axis is sufficient to not cause clipping to fields less than 30 arcseconds. Therefore, a mirror of this size would be suitable as the secondary in the primary beam expander.

### 3.3.3 Other Constraints

The mechanical components also influence the size of the obscuration made by the secondary mirror. A kinematic mount is desired for the secondary to allow adjustment to the tilt of the mirror. No suitable commercial off the shelf mount is small enough to fit in a 35 mm footprint. Therefore, a custom mount would be necessary to provide kinematic mounting to the mirror.

### 3.3.4 Vignetting due to Central Obscuration

The optical system is modelled in Zemax, with the a $35\times50$ mm elliptical mirror used as the secondary. This mirror is treated as a transparent surface by Zemax and the rays are allowed to pass through the surface. To simulate the obscuration created by the secondary, an obscuration is placed at the surface to block rays in a defined region. A circular obscuration with diameter 35 mm was created at the location of the secondary and the vignetting caused by the obscuration was viewed.

The focussed rays at the secondary mirror are shown in Figure 3.5. The rays are produced for fields between $\pm0.01$ degrees, which corresponds to $\pm36$ arcseconds, and is approximately the maximum field of view of the system (75 arcseconds).

All rays are reflected by the mirror surface, which indicates there would not be clipping of fields with a secondary of this size.

The fraction of un-vignetted rays with a circular obscuration of 35 mm in diameter is shown in Figure 3.6. The plot is produced for fields between 0 and 0.01 degrees, with 0.1 degrees the maximum field within the 75 arcsecond field of view of the imaging camera.

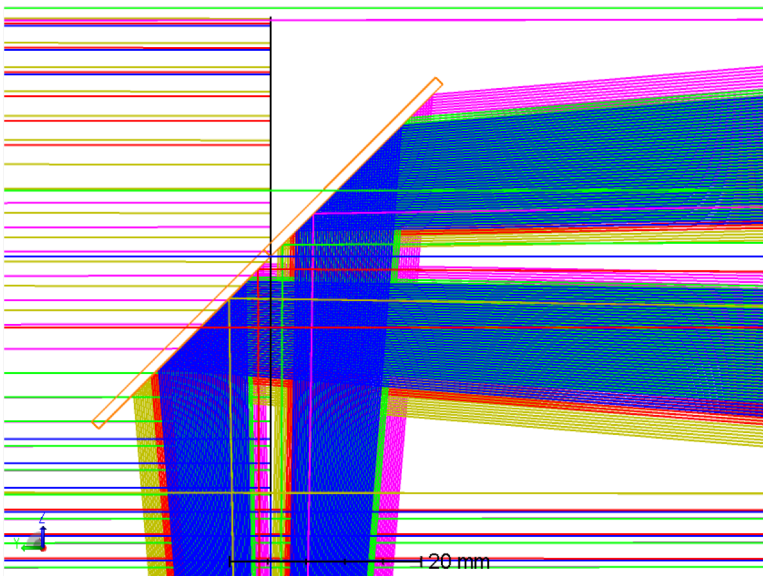


Figure 3.5: Ray trace at secondary mirror

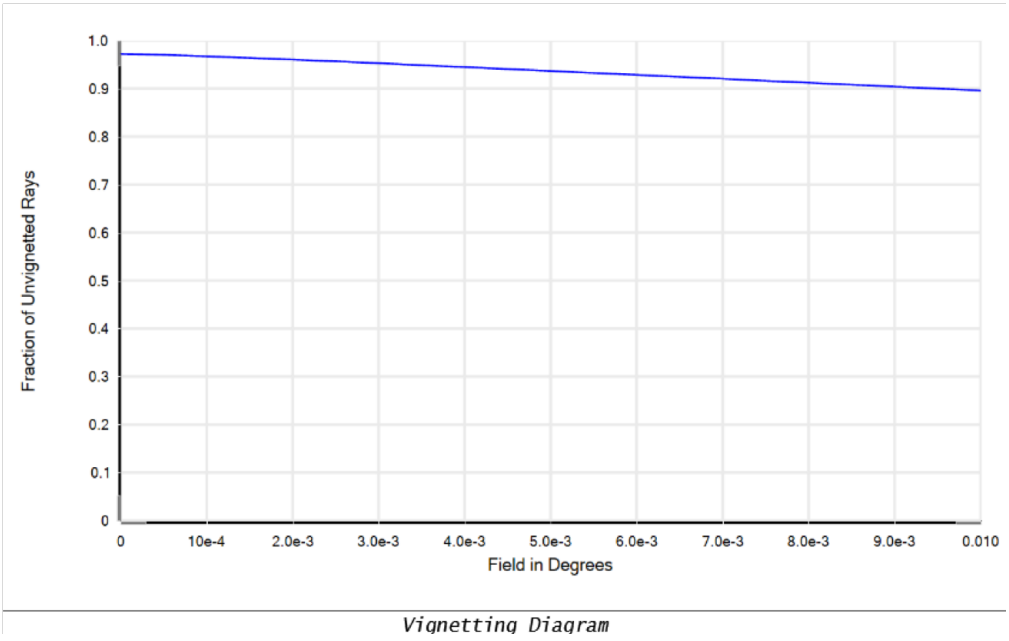


Figure 3.6: Fraction of un-vignetted rays with a circular obscuration

Table 3.1 provides the fraction of un-vignetted rays at different field angles for the obscuration. The vignetting is compared on axis, at 0.003 degrees, 0.004 degrees and 0.01 degrees.

Table 3.1: Fraction of un-vignetted rays with 35 mm obscuration

| Field Angle (degrees) | Fraction with circular obscuration |
|---|---|
| 0 | 0.972 |
| 0.003 | 0.953 |
| 0.004 | 0.945 |
| 0.01 | 0.896 |

### 3.3.5 Subaperture Blocking in the Wavefront Sensor

The PBX secondary obscuration can also block subapertures in the WFS if it is too large along with the spider vanes that support the secondary. The 35 mm diameter obscuration of 35 mm at the PBX becomes a 3.3 mm diameter obscuration at the DM due to the magnification of 10.6. The DM actuator spacing is 1.5 mm so there will be a 2×2 grid of actuators that is blocked by the telescope and PBX obscuration. The spider supporting the secondary mirror has vane thickness of 2 mm, at the microlens array this obscuration is 0.038 mm. Therefore, the PBX secondary vanes are blocking up to 12% of the subaperture area for subapertures, which are vignetted by the spider. Given the symmetry of the system there is a boundary between rows/columns where the spider blocks the subapertures as shown in Figure 3.7. As the vane is split between the two columns of the subaperture the vignetting experienced by the subaperture is due to half the width of the vane, which is approximately 6% of the subaperture.

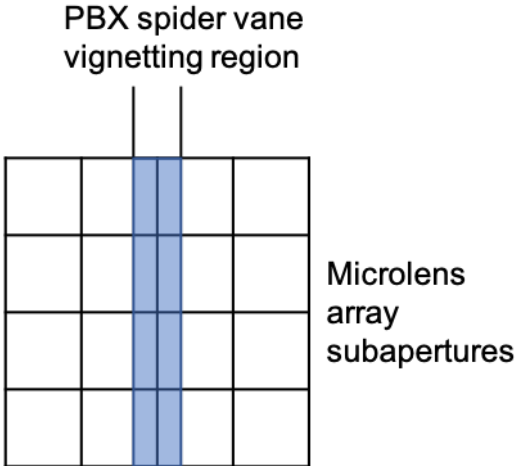


Figure 3.7: Vignetting of WFS subapertures due to PBX secondary spider

## 3.4 Adaptive Optics

The adaptive optics (AO) subsystem features the deformable mirror (DM) used to perform wavefront correction. The DM chosen for AOI is the ALPAO DM277, which features 277 actuators in a 17×17 grid. The choice of DM is discussed in Section 2.3.1.

The DM is located in the pupil plane of the optical system, which is 220 mm from the final beam expander optic as noted in Section 3.3. To prevent the incoming and reflected beam from the DM overlapping, the DM is angled at 8 degrees relative to the incident beam.

The AO subsystem also features a fold mirror between the DM and the dichroic beamsplitter. The optical layout of the AO system is shown in Figure 3.8.

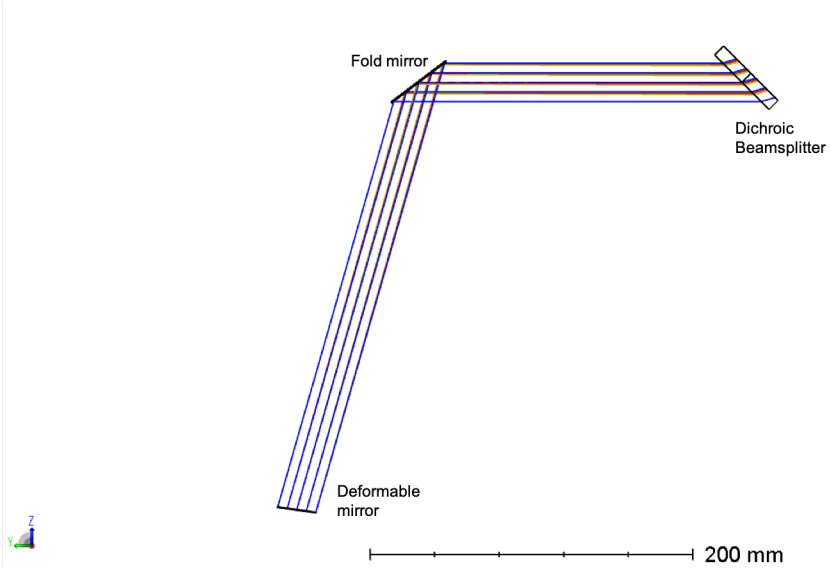


Figure 3.8: Optical layout of adaptive optics subsystem

## 3.5 Wavefront Sensing

The wavefront sensing subsystem performs measurement of the wavefront needed to control the DM. Light to the WFS is transmitted through the dichroic beamsplitter, with different wavelength ranges transmitted for NGS and LGS modes. In NGS mode the dichroic beamsplitter will transmit 450 – 800 nm wavelengths to the wavefront sensor, while in LGS mode the dichroic beamsplitter will transmit 589 $\pm$ 10 nm to the wavefront sensor.

In LGS mode the dichroic beamsplitter will transmit all wavelengths <650 nm to the wavefront sensor. To eliminate all wavelengths except the desired 589 nm a 589 $\pm$ 10 nm bandpass filter is placed in the beam path to cut out all the undesired wavelengths.

The beam transmitted through the dichroic beamsplitter is reduced in size by a refractive beam expander featuring 3 lenses. Magnification control can be performed by adjusting the position of the second and third lenses in the beam expander allowing for fine control of the beam size on the microlens array. Actuator pitch is 1.5 mm at the DM and the beam must be reduced so the spacing is 300 µm at the microlens array to maintain Fried geometry. Therefore, the beam expander requires a magnification of 5.

After the beam expander the beam is directed onto the microlens array. A different microlens array will be used for the NGS and LGS modes. In NGS mode a microlens array with 300 µm pitch and 20 mm focal length will be used. This gives a plate scale of 0.68 arcseconds/pixel. In LGS mode a microlens array with 300 µm pitch and 8 mm focal length will be used. The performance of the system is improved by increasing the plate scale of the WFS to approximately 1.3 arcseconds/pixel. The microlens array chosen gives a plate scale of 1.55 arcseconds/pixel. This plate scale is too large; however, no COTS microlens array with 300 µm pitch could be found that would give a plate scale of 1.3 arcseconds/pixel and a custom array was too expensive to consider.

At the focus of the beam expander a removable field stop is placed to limit the field of view of the wavefront sensor subapertures. The field stop prevents light from a subaperture moving into one of its neighbours, which would cause an error in the centroid measurement for the spot. This will also limit the background light that can

enter the wavefront sensor so fainter objects can be used for AO operations. Given the NGS mode plate scale of 0.68 arcseconds/pixel each subaperture has a field of view of 8.16 arcseconds. A pinhole with 600 µm diameter will limit the subaperture field of view to 8.16 arcseconds.

A pair of lenses is used to relay the beam between the microlens array and the wavefront sensing camera. The detector focal plane is approximately 20 mm from the front face of the camera; therefore, the LGS microlens array requires the relay to get the spot focus on the detector. A pair of 40 mm focal length lens and are used to relay the beam to the detector focal plane. To maintain consistency between the NGS and LGS modes the same relay will be used for both; however, the distance from the mircolens array to the relay will change so the focal plane remains the same.

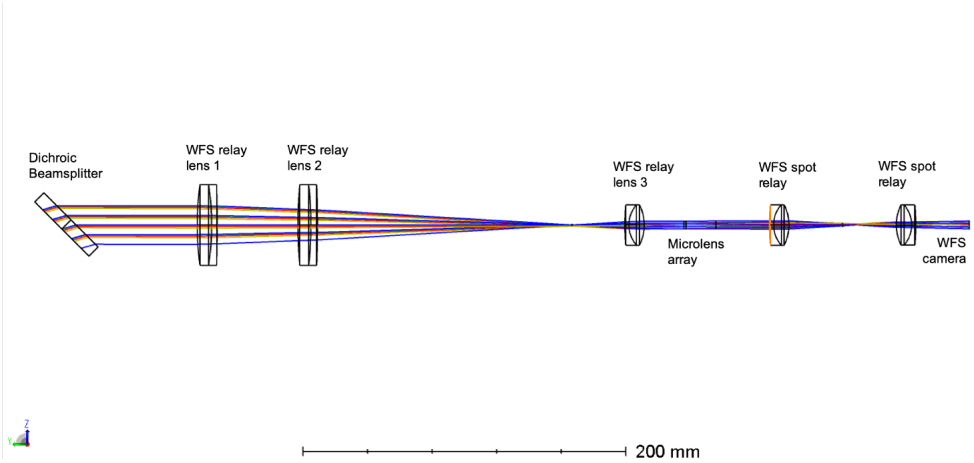


Figure 3.9: Optical layout of wavefront sensor

## 3.6 Calibration & Alignment

### 3.6.1 Calibration

The calibration subsystem is used to calibrate the DM to the wavefront sensor and build the interaction matrix. The calibration subsystem consists of two fibre sources, which are combined with a beamsplitter and collimated onto the DM. The two calibration sources are required for calibrating the wavefront sensor in LGS mode while only a single broadband source is needed to calibrate the NGS mode.

For LGS mode calibration one source is the broadband LED, while the other is a 589 nm LED. A notch filter centred at 589 nm will be placed in front of the broadband source to remove all 589 nm light. The two light sources are combined together with a beamsplitter cube.

The collimating lens for the calibration sources is selected so the image of the calibration source will be sized at approximately 2 pixels at the detector. The ratio of the size of the image created to the size of the object is equal to the ratio of input and output F numbers as given by

$$\frac{s_{im}}{s_{ob}} = \frac{F_{im}}{F_{ob}} \tag{3.2}$$

where $s_{im}$ is the spot size of the image, $s_{ob}$ is the size of the object, $F_{im}$ is the F number of the imaging lens and $F_{ob}$ is the F number of the fibre collimating lens.

To produce a spot approximately 32 µm in diameter (2 pixels) at the imaging detector a 10 µm fibre and 400 mm focal length lens is needed. A 200 µm core fibre will produce a spot approximately 48 µm in size at the wavefront sensor camera, which is the desired 2 pixels.

The layout of the calibration subsystem is shown in Figure 3.10. An iris is included after the collimating lens to control the beam size onto the DM.

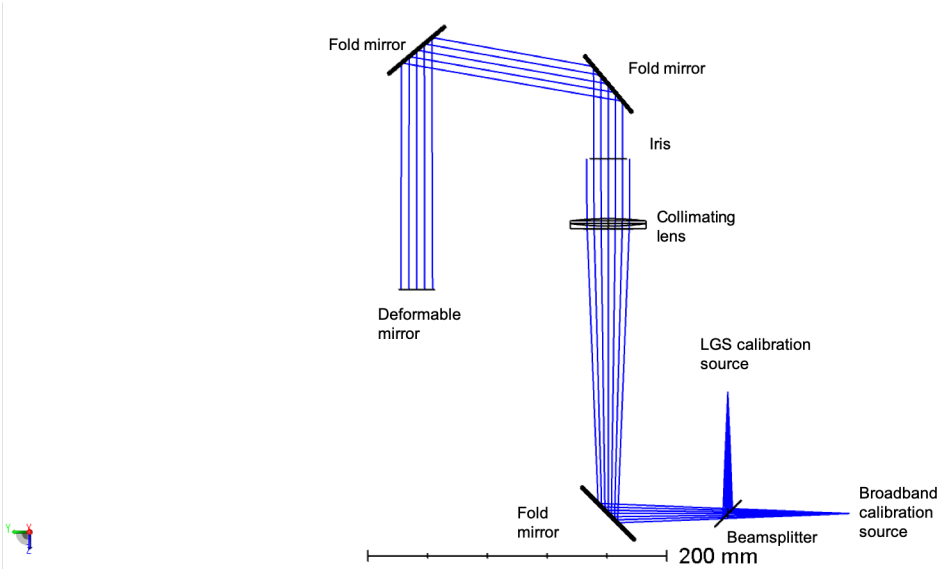


Figure 3.10: Optical layout of calibration

### 3.6.2 Alignment

The alignment subsystem is used to align all optical components in AOI and align the entire system to the telescope coudé path. Alignment is performed by a laser, which enters the system by a pellicle beamsplitter. To make the beam propagate in both directions through the system a mirror is placed after the pellicle to reflect the beam back upon itself and return to the pellicle.

To align the entire system to the telescope coudé path the laser beam must be allowed to propagate into the coudé path. In order to do this the elliptical secondary mirror of the primary beam expander must be replaced with a pellicle beamsplitter.

Neutral density filters will be placed at the laser output to limit the power transmitted to the system. A set of ND filters will be available to control the throughput, with OD of 0.5, 1, 1.5, 2 and 3.

## 3.7 Imaging Design Overview

The imaging subsystem captures images of the targets of interest using the light corrected by the AO system. A dichroic beamsplitter splits the beam between the imaging subsystem and the wavefront sensing subsystem. The dichroic beamsplitter will be interchangeable to allow operation in NGS or LGS mode.

In NGS mode the dichroic will transmit 450 – 800 nm light to the wavefront sensor and reflect 800 – 950 nm light to the imaging subsystem. The dichroic needed for a particular operating mode would be swapped in before changing modes.

In LGS mode only 589 nm light is sent to the WFS while all other wavelengths can be reflected by the dichroic to the imaging camera. As discussed in 3.3 the custom lenses have been optimised for 600 – 950 nm; therefore, only wavelengths >600 nm need to be sent to the imaging camera. The dichroic for LGS mode will be a 600 nm shortpass dichroic that sends 450 – 600 nm to the WFS and 600 – 950 nm to the imaging camera. The WFS is limited to only 589 nm by placing a 589 $\pm$ 10 nm bandpass filter before the microlens array.

### 3.7.1 Imaging Design Constraints

The imaging subsystem of AOI is used to capture high resolution images of the target object. Therefore, the optical design of the imaging subsystem is conducted to maximise image quality.

For best image quality a diffraction limited spot will be Nyquist sampled, where the spot is measured with a 2×2 pixel region. The pixel plate scale for Nyquist sampling was determined in Section 2.4 to be 0.047"/pixel. It is desired that the plate scale is to be half the telescope diffraction limit, and the spot size 2 pixels wide. Satisfying both of these conditions has proved to be difficult due to opposing requirements to meet the constraints.

The spot size diameter is related to the F number of the beam and wavelength,

$$spot = \lambda F \tag{3.3}$$

where $\lambda$ is the imaging wavelength and F is the F number of the beam ($F = f/d$).

The imaging plate scale is defined by

$$platescale = \frac{1}{M} \tan^{-1} \frac{s}{f} \tag{3.4}$$

where M is the magnification of the system, s is the camera pixel size and f is the imaging lens focal length.

The spot size and plate scale are influenced by the focal length of the imaging lens. The other parameters are not variable as the magnification is set by the telescope and DM, and the pixel size is fixed by the camera. To satisfy the spot size and plate scale requirements the parameters of the system are substituted into the equations and solved for the focal length. To obtain a spot size 2 pixels in diameter at 800 nm imaging wavelength the focal length required is 470 mm, while to obtain a plate scale of half the telescope diffraction limit a focal length of 940 mm is required. Therefore, there is a different focal length specification to satisfy each condition and the specification differs by a factor of two. Both of these conditions cannot be met so in one or both must be compromised in the final design.In order to maintain the resolution of the system it is preferred to set the plate scale for Nyquist sampling, so the diffraction limited spot may be oversampled.

### 3.7.2 Optical Design

To decrease the optical path length to the imaging camera a compound lens system was utilised. This compound lens has two achromatic doublets that can be placed a defined distance from each other to give the desired effective focal length. This effective focal length is also tunable, by altering the distance between the two lenses the optimal focal length can be investigated on the working system. It is likely the best solution will be approximately midway between desired spot size and plate scale, which is around 750 mm focal length. The plate scale, spot radius, and field of view that can be achieved for the different possible effective focal lengths are listed in Table 3.2.

Table 3.2: Imaging Configurations

| Effective focal length (mm) | Plate scale ("/pixel) | F/# | Spot radius (µm) | Field of View (') |
|---|---|---|---|---|
| 470 | 0.094 | 20 | 16 | 48.2 |
| 750 | 0.059 | 31.9 | 25.5 | 30.2 |
| 940 | 0.047 | 40 | 32 | 24.1 |
| 1000 | 0.044 | 42.5 | 34 | 22.7 |

The lenses used in the imaging subsystem have focal lengths of 300 mm and -75 mm. The two lenses will be custom design to minimise aberrations in the system. The -75 mm lens was chosen as a -75 mm lens was required as part of the PBX collimating lenses. Purchasing two of the same custom lenses will reduce cost of procurement. The 300 mm lens is chosen to obtain a large field of view to search for objects.

The imaging subsystem features two imaging modes; a large field of view acquisition mode, and a high resolution mode. The two modes are possible by using two imaging lenses with one removable from the beam path. The acquisition mode uses a single 300 mm focal length lens, which provides a field of view of 75 arcseconds. The high resolution mode uses a combination of the 300 mm and -75 mm focal length lenses to create an effective focal length of between 750 and 940 mm. The EFL is tunable by modifying the distance between the two lenses. The imaging camera position remains fixed for both imaging modes; therefore, path length differences between the two modes are made with fold mirrors, which can move in and out of the beam path.

Using the single 300 mm lens in the imaging subsystem will provide a 75.5 arcsecond field of view. If both lenses are used for imaging the field of view will be between 22.7 and 30.2 arcseconds, depending on the effective focal length of the system.

The optical layout of the imaging subsystem in the high resolution mode, with both imaging lenses, is shown in Figure 3.11. With this layout four fold mirrors are required to direct the beam to the second imaging lens and provide the necessary path length increase.

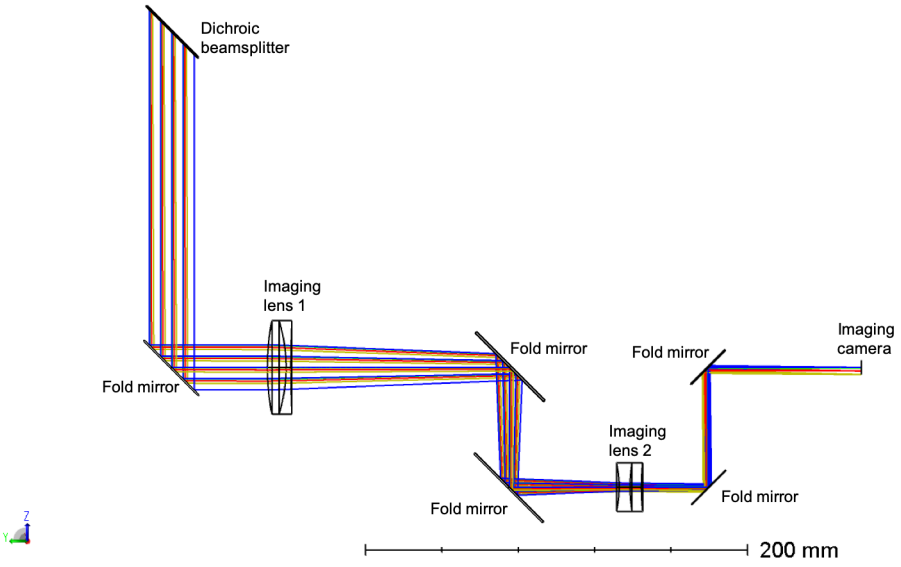


Figure 3.11: Optical layout of imaging subsystem in high resolution mode

The optical layout of the imaging subsystem in acquisition mode, with only one imaging lens, is shown in Figure 3.12. In this mode image is formed directly by the f = 300 mm lens.

#### 3.7.2.1 Imaging Performance

The custom lenses are designed to reduce aberrations in the final images to obtain the optimal imaging performance. The spots produced at the focus in both give an indication of the amount of aberration. The priority is the spots in the high resolution imaging mode which uses both of the lenses, the images captured using just the 300 mm lens are only for acquisition.

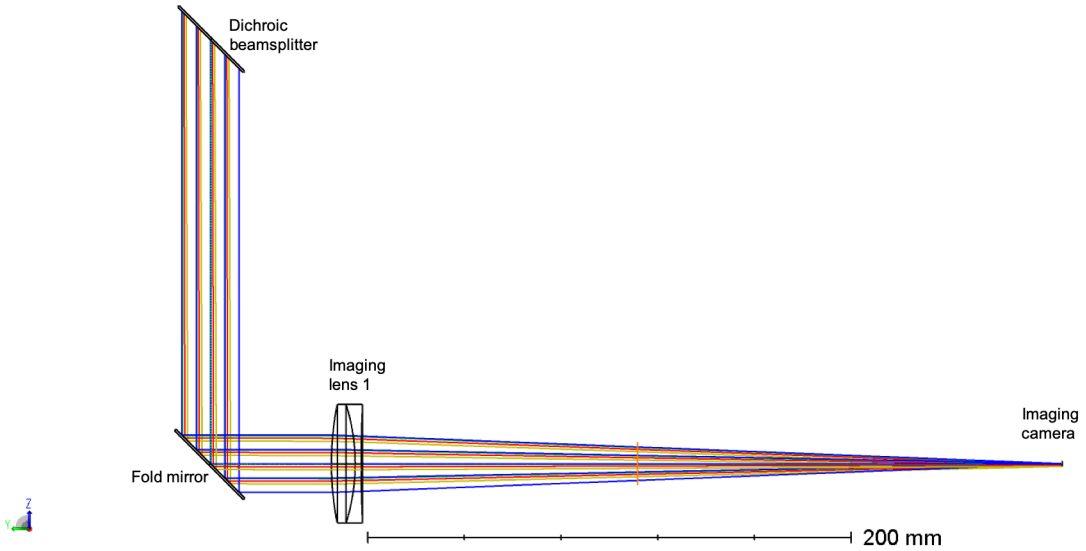


Figure 3.12: Optical layout of imaging subsystem in acquisition mode

The spot diagram for the high resolution imaging mode with an effective focal length of 750 mm is shown in Figure 3.13. This features the maximum wavelength range of the custom lens designs, 600 – 950 nm. The spots are given for three positions; on axis, 5" off axis, and 10" off axis.

In NGS mode only 800 – 950 nm are used for imaging. With a smaller wavelength range used for imaging there are less chromatic aberrations and the spots are contained within the Airy disk. The spot diagram with the high resolution mode and wavelength range of 800 – 950 nm is shown in Figure 3.14. The spots are given for three positions; on axis, 5" off axis, and 10" off axis.

The Strehl ratio in this configuration is 95%, which indicates that aberration in the design have been minimised. A Strehl ratio this high will not be achievable when operating AOI, the aim is to achieve 30% Strehl from closed loop AO operations.

The spots produced by the single 300 mm focal length lens in the acquisition mode are shown in Figure 3.15. This features the maximum wavelength range of the custom lens designs, 600 – 950 nm. The spots are given for three positions; on axis, 10" off axis, and 36" off axis.

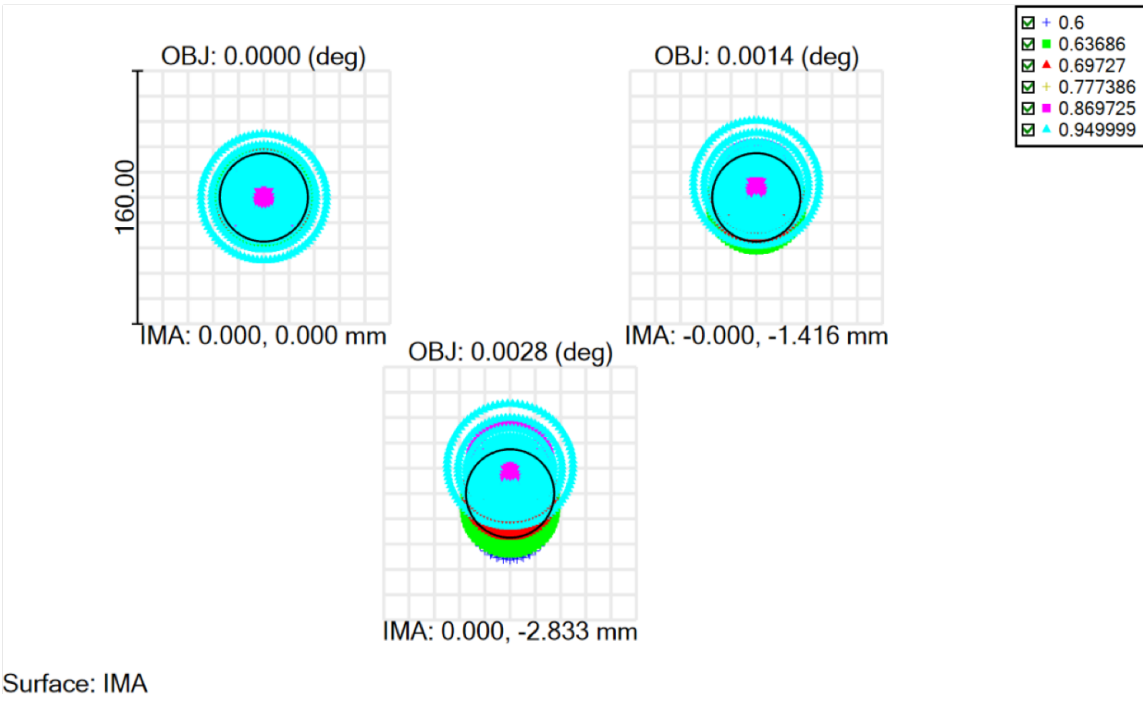


Figure 3.13: Spot diagram in high resolution imaging mode with EFL = 750 mm and wavelength range of 600 – 950 nm

The spot diagram for the acquisition mode shows there is considerable aberration in the spot at 36" off axis. This is the edge of the total field of view of the system and the mode is not used for capturing images so the distortion is not a concern. A small spot for the acquisition mode would be ideal to focus all the light to allow fainter objects to be found; however, the performance of the system is appropriate for the acquisition imaging mode.

The spot diagram in NGS mode with a wavelength range of 800 – 950 nm is shown in Figure 3.16. The spots are given for three positions; on axis, 10" off axis, and 36" off axis.

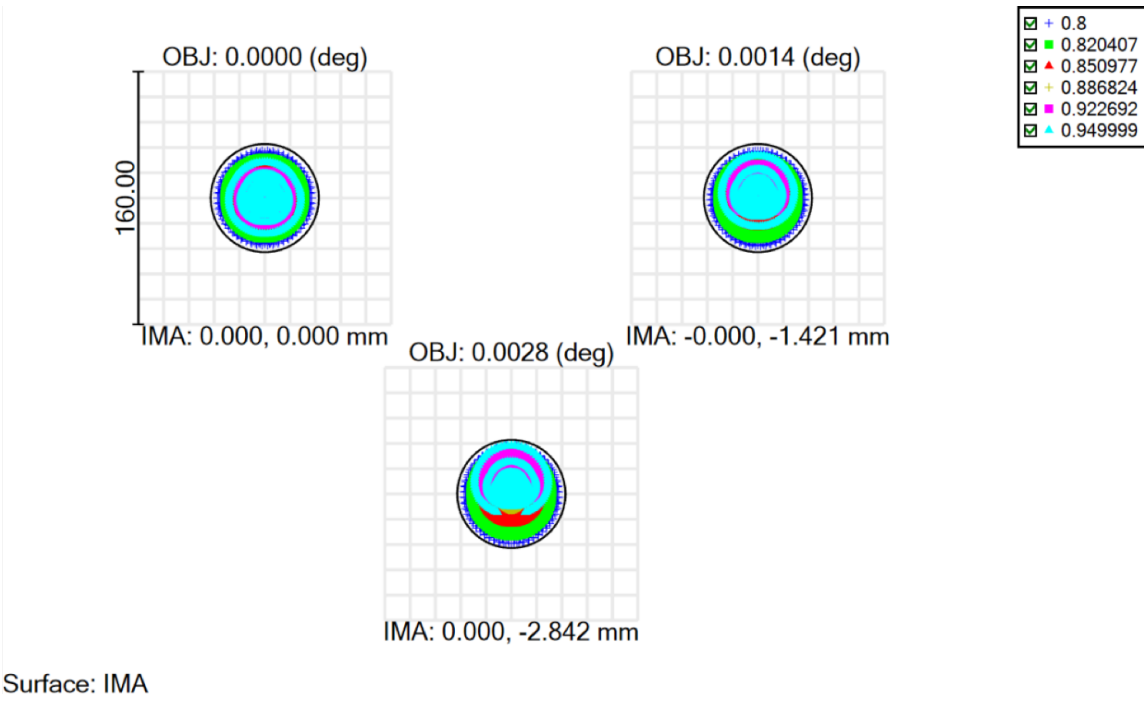


Figure 3.14: Spot diagram in high resolution imaging mode with EFL = 750 mm and wavelength range of 800 – 950 nm

## 3.8 Custom Lens Design

AOI requires four custom designed lenses to achieve the desired optical performance across a broad wavelength range. The nominal optical performance goal is diffraction limited imaging between 450 – 950 nm wavelength range, which is the sensitivity range of a silicon detector. Custom lenses are useful as they can be made to a specific focal length.

The four custom lenses in AOI are for the primary beam expander and imaging subsystems. During design the system was optimised with variables on all four lenses to ensure the final image quality was maximised. In each subsystem the two lenses are used as a compound system with a short focal length negative lens and a longer focal length positive lens. In the primary beam expander the compound lens gives the necessary effective focal length for magnification while also extending the pupil plane 220 mm from the lens so the DM can be placed without the need to relay the pupil.

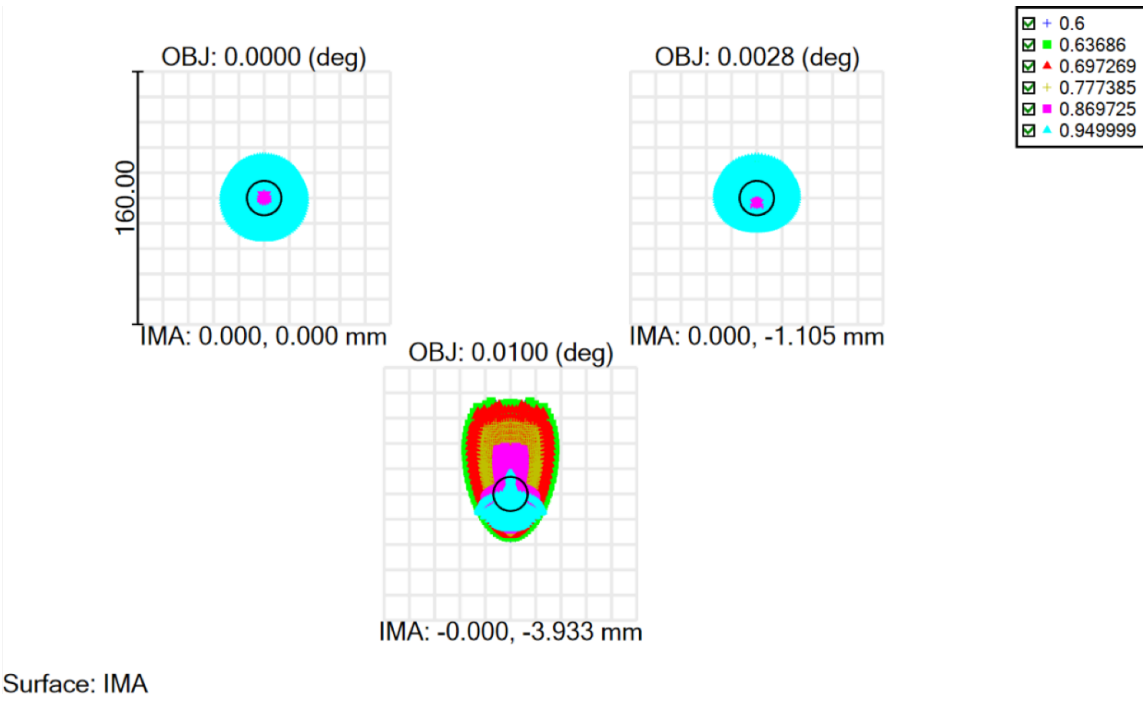


Figure 3.15: Spot diagram in acquisition imaging mode with wavelength range of 600 – 950 nm

In the imaging subsystem the compound lens can allow a long effective focal length of 940 mm but with a shorter physical length. The compound lens in the imaging path also provides an option to bypass the negative lens to reduce the effective focal length, which increases the field of view for acquisition purposes.

The approximate focal lengths and separation for the two compound lens were calculated using the thin lens equation and are shown in Table 3.3.

Table 3.3: Compound lens specifications

| | Effective focal length (mm) | Negative lens (mm) | Positive lens (mm) | Separation (mm) | Focus position (mm) |
|---|---|---|---|---|---|
| PBX | 149.8 | -75 | 129 | 110 | NA |
| IMG | 940 | -75 | 300 | 249 | 160 |

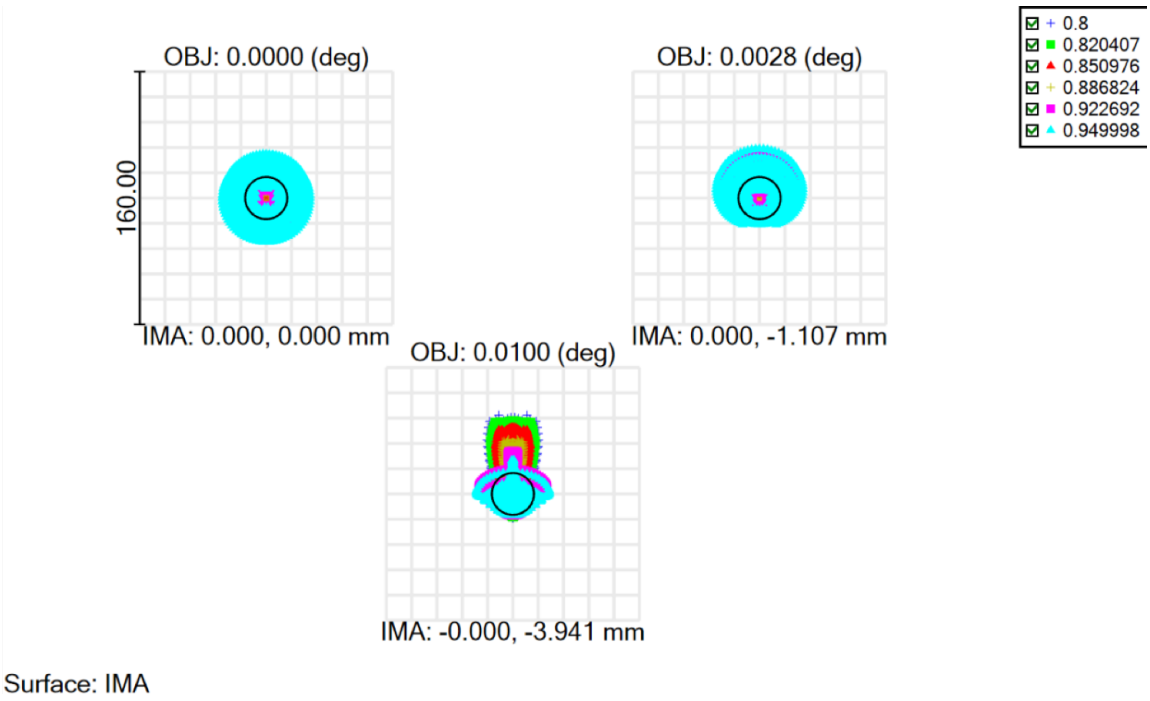


Figure 3.16: Spot diagram in acquisition imaging mode with wavelength range of 800 – 950 nm

As with the rest of the system the design of the lenses were designed using Zemax OpticStudio. The radius of curvature, thickness and material types for each part of the lenses were set to variable and inbuilt tools in Zemax used to optimise the parameters.

No solution was found for the desired imaging quality over the 450 – 950 nm wavelength range when using standard cemented doublets. If an air gap was added to the doublets and the system was optimised, a suitable solution could be found. Due to the additional cost and complexity in mounting a air-spaced doublet with precise separation of lenses a decision was made not to use air-spaced doublets. Each air-spaced doublet would require a custom mount so that the lenses could be spaced with the correct gap.

The imaging wavelength range was relaxed to 600 – 950 nm. The system was again optimised with the new parameters and acceptable imaging performance was achieved with cemented doublets as shown in Figure 3.13. When in the wavelength range 800 – 950 nm, which is used for the NGS mode, the spot is contained within the Airy ring thus diffraction limited imaging is achieved as shown in Figure 3.14.

## 3.9 Mechanical Design

The mechanical design of AOI was performed after the optical design was completed. The optical design set the parts that were needed such as lenses and mirrors in addition to each components size. The mechanical design encompasses mounted optics, camera mounts and the deformable mirror mount.

Where possible commercial off the shelf (COTS) parts were used to decrease cost and complexity. As the system is situated in a clean room all the parts are in a stable environment and therefore, COTS parts provide suitable performance and stability. Custom mechanical parts are only used when a COTS part is not available such as for interface plates and mounts for non standard components. COTS optical mounts and stages provide sufficient stability and precision for AOI, and as there was no strict space limitations they were suitable for most components. As the COTS parts are mass produced they are also cheaper to obtain over one off custom parts, which was a consideration when completing the design.

A complete 3D model was constructed using Solidworks. Each of the COTS parts used has a Solidworks model file available from the manufacturer, and parts were made for any custom parts. Figure 3.17 shown the top down view of the AOI Solidworks model which includes SCIDAR. Figure 3.18 shows an isometric view of the AOI 3D model.

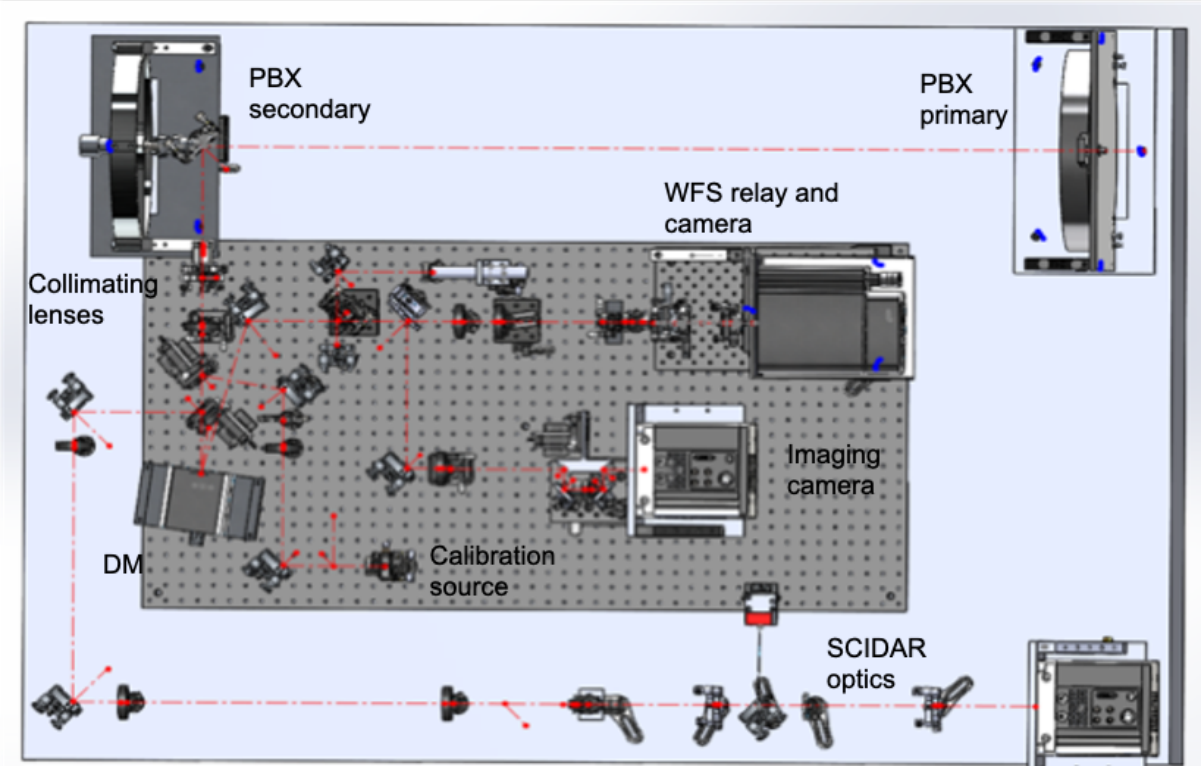


Figure 3.17: Top view of AOI model with SCIDAR

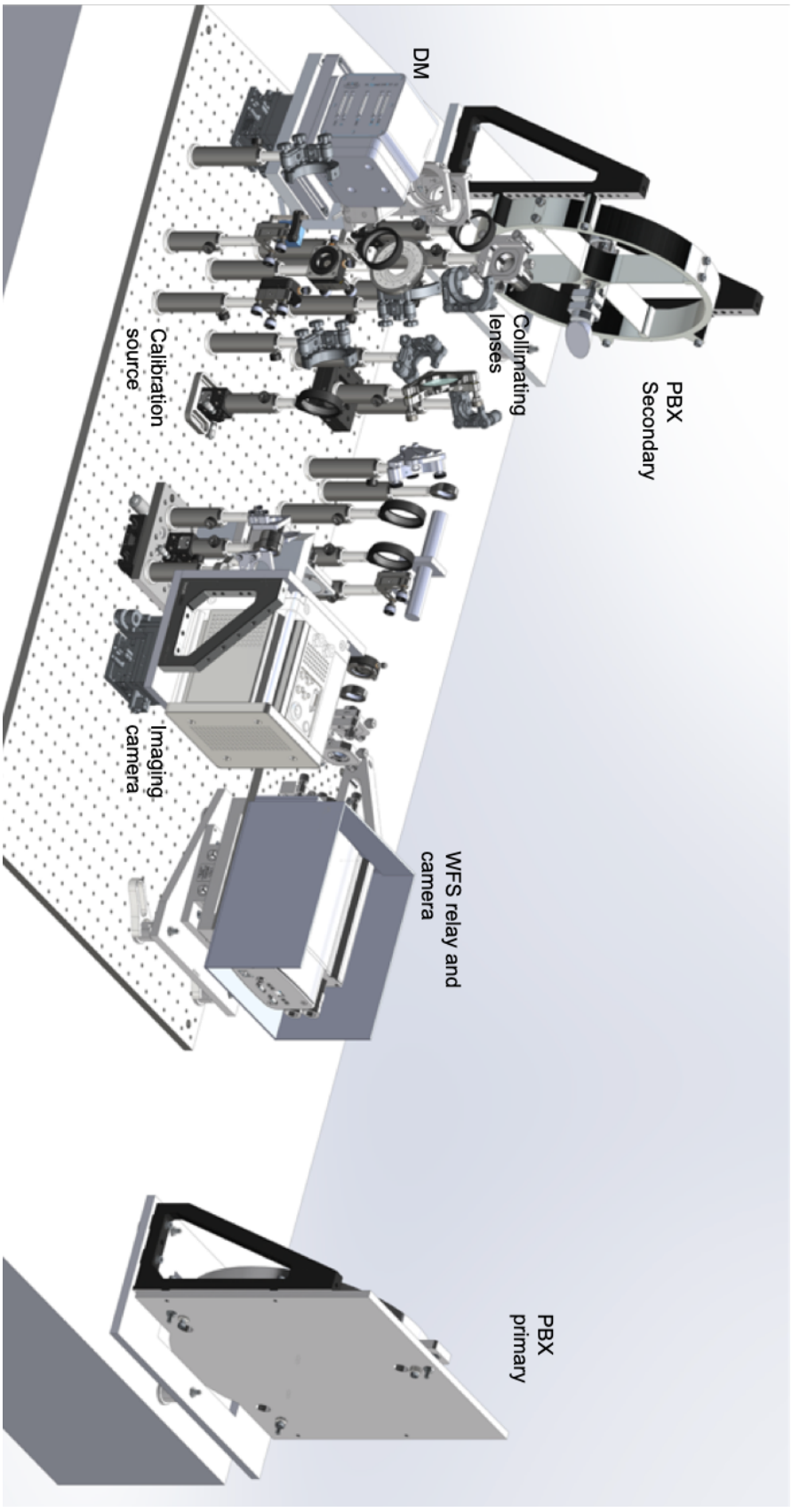


Figure 3.18: 3D model of AOI

### 3.9.1 Primary Beam Expander

The primary beam expander mechanical design consists of the primary mirror mount, secondary mirror mount and the collimating lenses mount. The primary and secondary mirror mounts are placed on individual kinematic bases, which provide tip, tilt, and piston adjustment.

#### 3.9.1.1 Primary Mirror

The mechanical mount for the primary mirror of the beam expander is shown in Figure 3.19. The 300 mm diameter mirror is contained in the mirror cell and attached to a fixed backboard with three points. Jackscrews are used to adjust tip-tilt and piston of the mirror with a restoring spring force to return it to the backboard.

The primary mirror cell is mounted onto a a base which lies on three kinematic feet as shown in Figure 3.19. Adjustment to the base is made with jackscrews. The base can be adjusted vertically by turning all three screws equally in the same direction with tip-tilt of the entire assembly also possible.

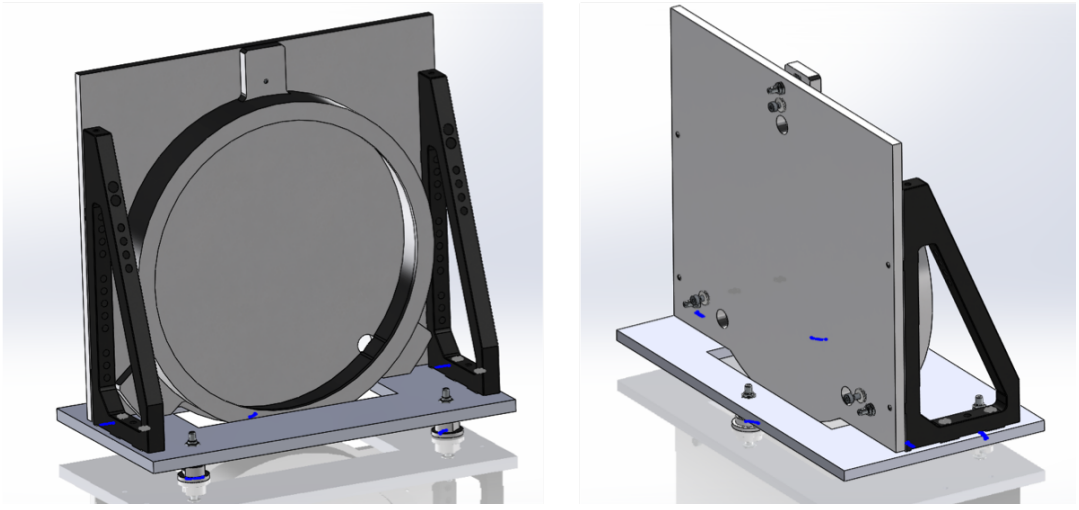

Figure 3.19: Primary mirror assembly

#### 3.9.1.2 Secondary Mirror

The secondary mirror is a small 35×50 mm elliptical mirror, which picks off the focussing beam from the primary mirror and reflects it at a 45 degree angle. Given that the secondary is within the incoming coudé path beam the mechanical mount must be made to reduce vignetting of the beam as much as possible. The secondary mount features a ring with spider vanes to support the centred mirror mount, the mounting for the secondary mirror, and a kinematic base as shown in Figure 3.20.

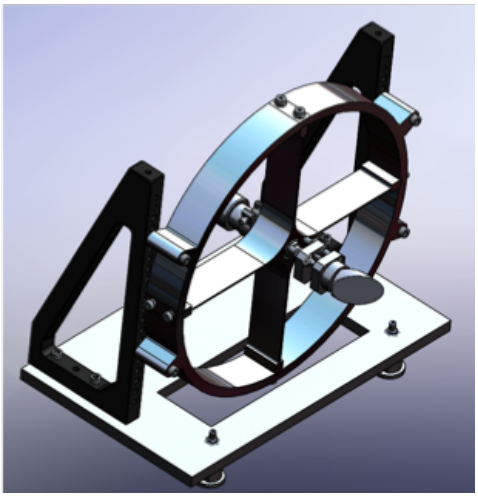

Figure 3.20: Secondary mirror assembly

The mirror mount features a compact kinematic design to allow for tip-tilt and piston of the mirror during alignment. This mount is attached to a shaft through the centre of the spider vanes to allow the entire mount to rotate about the optical axis. This can be used to align the mirror so the reflected beam will be parallel to the optical table. The secondary mirror mount is shown in Figure 3.21. To prevent the secondary mirror vignetting the coudé beam the secondary mirror mount assembly is restricted to a 35×35 mm area. This is the same size as the obscuration caused by the telescope secondary mirror as discussed in Section 3.3.1. The secondary mount also features a counterweight to maintain balance of the assembly.

The secondary spider features a large ring to allow the 251 mm coudé beam to pass through and 4 thin vanes to support the mirror mount. As discussed in Section 3.3.5 the spider will block the WFS subapertures. The 2 mm thick spider vanes will block approximately 6% of the affected subapertures.

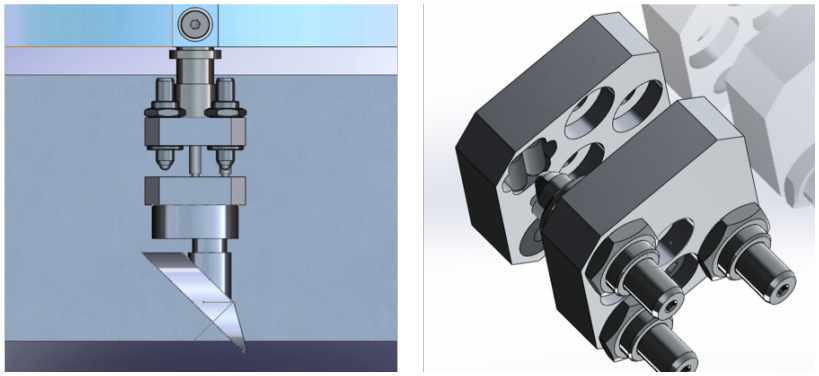

Figure 3.21: Kinematic and 45 degree angle mount for beam expander secondary mirror

The entire secondary mirror ring and angle brackets can be removed from the base so the beam expander can be aligned to the telescope coudé path. If the alignment laser from AOI is used to align the system to the coudé path it would be blocked by the secondary mirror. The secondary mirror is instead replaced with a pellicle beamsplitter, which is aligned into the same position as the mirror. This beamsplitter will allow the alignment laser to be transmitted to the coudé path.

Once the beam expander is aligned the secondary mirror assembly is replaced. The secondary base features four dowel pins, which register the angle brackets to the same position so the secondary mirror can be removed and replaced into the same position.

#### 3.9.1.3 Collimating Lenses

The two collimating lenses are mounted on the AOI breadboard using COTS parts. The negative lens is mounted in a lens barrel attached to a 5 dof kinematic mount that allows X, Y, Z translation along with tip-tilt. An iris is placed before the lens it the focal plane and acts as a field stop. The 2 inch positive lens is mounted in a fixed 2 inch lens mount and the post holder attached to two 5 mm travel linear stages orthogonal to each other that provides X, Y, Z adjustment.

### 3.9.2 Wavefront Sensor

The wavefront sensor mechanical mount houses the WFS camera, microlens array, and the relay from the microlens array to the camera as shown in Figure 3.22. The WFS mechanical design is adapted from a previous instrument and the camera mount, relay, and microlens array mount was maintained. The microlens array is glued to a custom mount that is mounted to a 1 inch kinematic mount with X, Y, Z translation along with tip-tilt. The kinematic mount is mounted to a goniometer to give rotational adjustment. The WFS mount is placed on an X, Y translation stage and kinematic base for Z and tip-tilt adjustment.

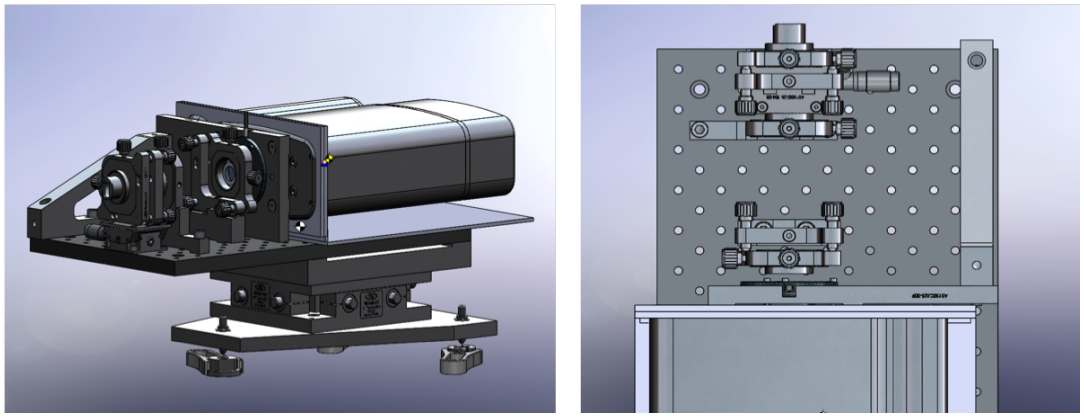

Figure 3.22: WFS mechanical assembly. The assembly contains the WFS camera, microlens array and two relay lenses. The assembly sits on three kinematic feet for tip, tilt, and piston adjustment, in addition to registration for replacing the assembly if it is removed.

The entire WFS mount is shared with a separate AO system for space debris manoeuvre using photon pressure. The three kinematic feet provide a reference for the position of the WFS mount and remain on the AOI breadboard. There are an identical set of feet in the other AO system, which provides the same function.

### 3.9.3 Breadboard

All components of AOI but the primary and secondary mirror mounts are contained on a 1200×600 mm breadboard. The optics are mounted using COTS parts and custom parts are used where required. All mirrors are mounted in kinematic mounts allowing for tip-tilt and piston of the mirror during alignment. The lenses are contained in fixed mounts as precise tip-tilt is not required.

### 3.9.4 Imaging Camera

The Nuvu Hnu 512 camera has four M5 tapped holes on the front for mounting. An interface plate was built to mount the camera and attach a X, Y, Z translation stage to position the camera in the focal plane of the optical system. The mechanical mount for the imaging camera is shown in Figure 3.23.

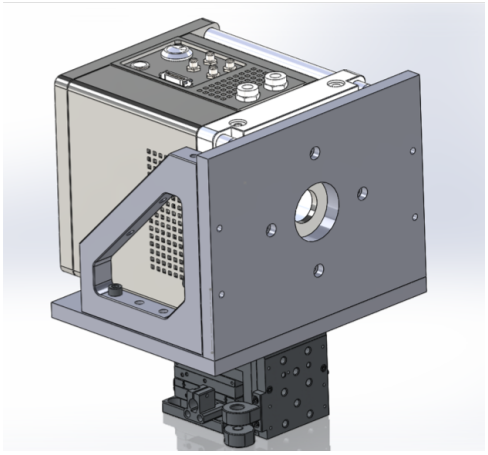

Figure 3.23: Imaging camera assembly. The Nuvu Hnu 512 is bolted to the front plate and and interface plate mounts this to an X, Y, Z translation stage

### 3.9.5 Deformable Mirror

A tip-tilt mount was purchased with the ALPAO DM277. An interface plate is used to attach the tip-tilt mount to a X, Y, Z translation stage, giving five degrees of freedom for the DM alignment.

### 3.9.6 SCIDAR Interface

In order to accommodate the SCIDAR instrument on the optical table and retain the capability to operate it concurrently with AOI an interface was implemented to allow quick switching between the two instruments. A 2 inch flipper mirror was placed between the calibration source flipper and the DM, which allows the collimated beam from the beam expander to be picked off and sent to SCIDAR. A 1:1 relay follows the fold mirror and relays the pupil plane into SCIDAR. The interface to SCIDAR is shown in Figure 3.24.

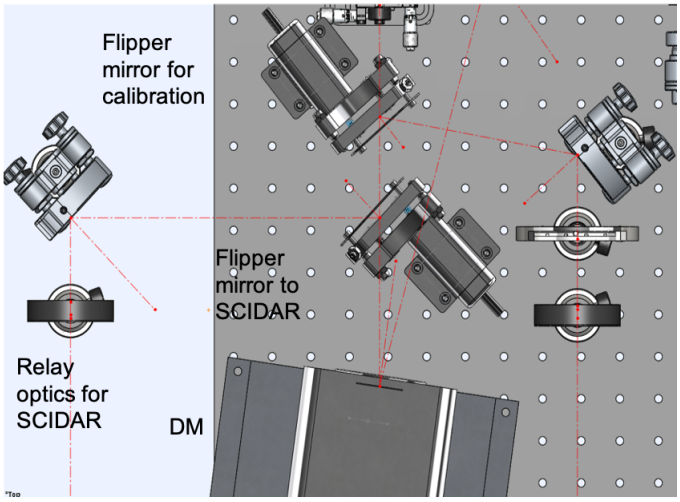


Figure 3.24: SCIDAR pick off with flipper mirror before DM

## 3.10 AOI Build and Telescope Integration

Upon completion of the optical and mechanical design of AOI the system was built and then moved to the telescope where it was integrated. Figure 3.25 shows the completed AOI instrument installed in the clean room.

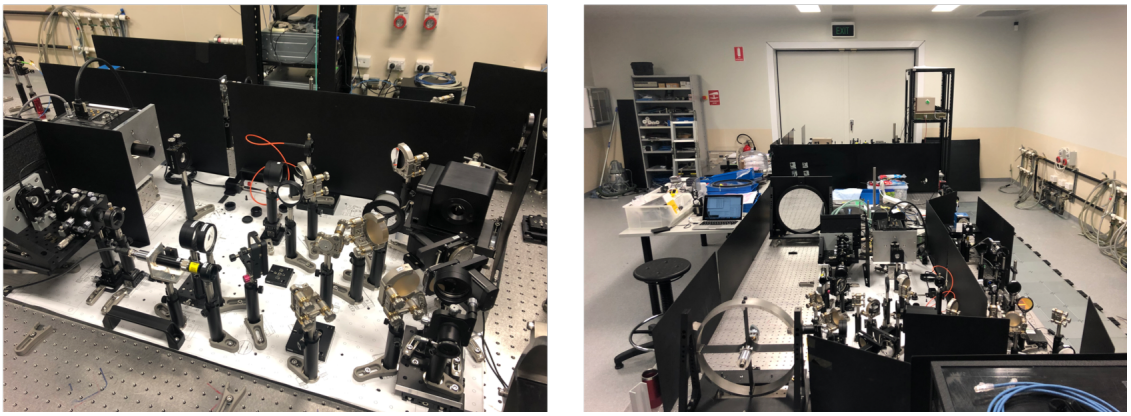

Figure 3.25: Left: Components installed on AOI breadboard. Right: Photo of entire AOI system with primary beam expander to the left, breadboard in the centre and SCIDAR on the right

### 3.10.1 Baffling

Due to background light in the clean room where AOI is located steps were taken to baffle the entire bench and reduce background light entering the system. The background light present in the lab includes an SLR laser that is in continual operation and causes obvious background signal throughout the entire room where AOI is located. There is also an IR security camera which overlooks the optical bench and emits IR light which can be detected by the cameras. There is also light from electronics such as computers and phone that are visible in the lab. To reduce stray light falling on the imaging camera a lens tube has been attached between the camera and final imaging lens. Black foil is also placed around the entire WFS assembly, which significantly reduces the background light on the WFS camera.

To further reduce background light the AOI breadboard and beam expander have been surrounded by laser shielding and a cover placed over the top to shield the entire system as shown if Figure 3.26.

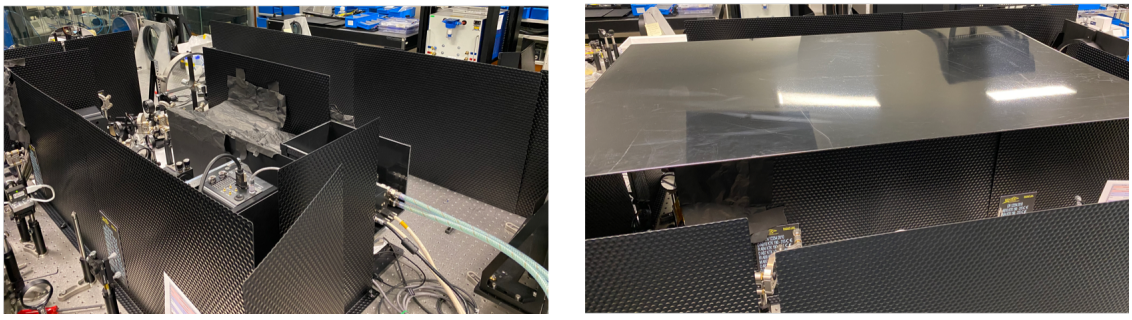

Figure 3.26: Left: laser shielding surrounding AOI Breadboard and beam expander. Black foil also covers the WFS optics. Right: Cover placed over the AOI breadboard

### 3.10.2 AOI Implementation Compromises

Due to time constraints during assembly some parts of AOI were not implemented so the system could be made operational. There was time pressure to begin on-sky operation to obtain results and to gather data so results were obtained to complete PhD work during the four year enrolment time. Additionally the SERC cooperative research centre funding was coming to an end, which would restrict operational effort and access to the telescope.

The FOV switching mechanism was not implemented, and instead the system was built with only the high resolution imaging mode. The FOV switching method would be difficult to implement and align so that both focal planes were in the same location. Additionally maintaining the alignment could have presented issues. As there was also time pressure to complete lab testing and begin on-sky operations it was decided to not use the large FOV acquisition mode and instead only use the high resolution mode. The acquisition mode was not essential to operation of AOI and therefore, could be discarded without any impact on performance. Finding objects, particularly LEO satellites would be more difficult without the acquisition mode; however, alternative solutions to search were available such as using the WFS. Each subaperture of the WFS has a small FOV of approximately 8" and the field stop restrict the FOV to this. If the field stop is removed then the total FOV of the WFS is $8\times16$ = 128". This field stop is mounted on a magnetic kinematic base so it can be removed and returned without losing alignment so this method was appropriate for acquiring the objects during operation.

The laser guide star mode of AOI was also not implemented due to delays in the laser guide star facility (LGSF) and guide star laser (GSL). When AOI was first built and commissioned on-sky the LGSF and GSL were not available. During all observations for work during this thesis they remained unavailable, thus it was not possible to operate in the LGS mode. The LGS mode required a different microlens array to change the plate scale of the WFS and a different dichroic which reflects a larger wavelength range to the imaging camera. Work on the LGSF and GSL was beyond the scope of this work, thus the delays in these programs resulted in the full capability of AOI not being demonstrated.

Chapter 4

# Image Processing

This chapter details the processing that is performed on images before they are analysed. The images that are collected are raw frames and some processing is required to remove the camera bias and background noise. During an observation night >60,000 frames were typically captured. It would not be feasible or efficient to analyse all of the images captured so techniques such as lucky imaging are used to filter the data so that only the best quality frames are selected. Frames are also stacked together for improved signal to noise and the different techniques used are discussed in this chapter.

## 4.1 Image Bias and Background Subtraction

Each image that is captured features signal that is not from the object of interest. This comes in the form of camera bias and background light imaged by the system. The camera bias is generated by the camera electronics and is seen when there is no light input to the system. The background signal comes from sky background and stray light within the lab while AOI operates. The amount of stray light entering the system is minimised by using baffling and a cover however there are numerous light sources within the lab which could provide background. These light sources include; satellite laser ranging system outputting 1 W average laser power, IR security camera directed towards the optical table, and light from electronics in the lab.

To effectively process images all signal except those from the desired target must be removed. The camera bias can be removed by capturing bias frames and subtracting from the raw images. The Nuvu Hnu 512 features a mechanical shutter, which allows for all light to be blocked from the sensor and bias frames to be captured. A bias frame is shown in Figure 4.1. In this frame the bias signal is not uniform, which would impact analysis of images if it were not removed.

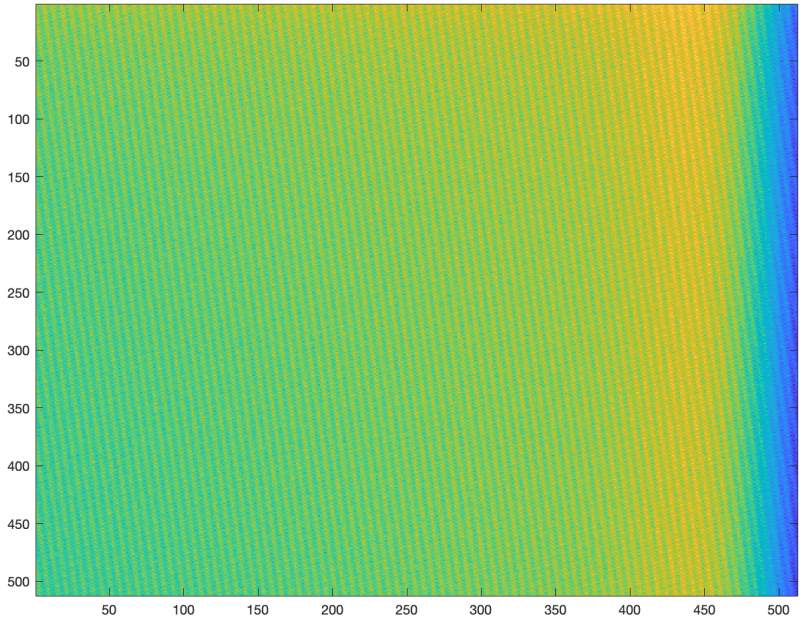


Figure 4.1: Bias frame captured from Nuvu Hnu 512 imaging camera

Removal of background signal is also necessary to avoid analysis of images with unwanted signal. Background signal can be corrected in a number of ways. The simplest method is to look at a patch of dark sky and capture images. If the bias frames, such as in Figure 4.1 are removed then the resulting frame is a combination of the sky background and lab background. Background levels may change over the different parts of the sky and over time. Background sources including the moon, light pollution from neighbouring suburbs, and laser operation can all change over time.

Removal of background is instead based on information obtained from each raw frame. The imaging target is always centred in the frame; therefore, the outer edges of the frame should not be receiving signal from the target. The background is measured by averaging the first 10 – 20 rows of the frame to obtain the x axis profile and the first 10 – 20 columns to obtain the y axis profile. The profiles can then be extrapolated to compute the background frame, which is removed from the raw frames. Figure 4.2 shows the profiles of the background signal in x and y from a image. The profiles are then converted into a background frame shown in Figure 4.3.

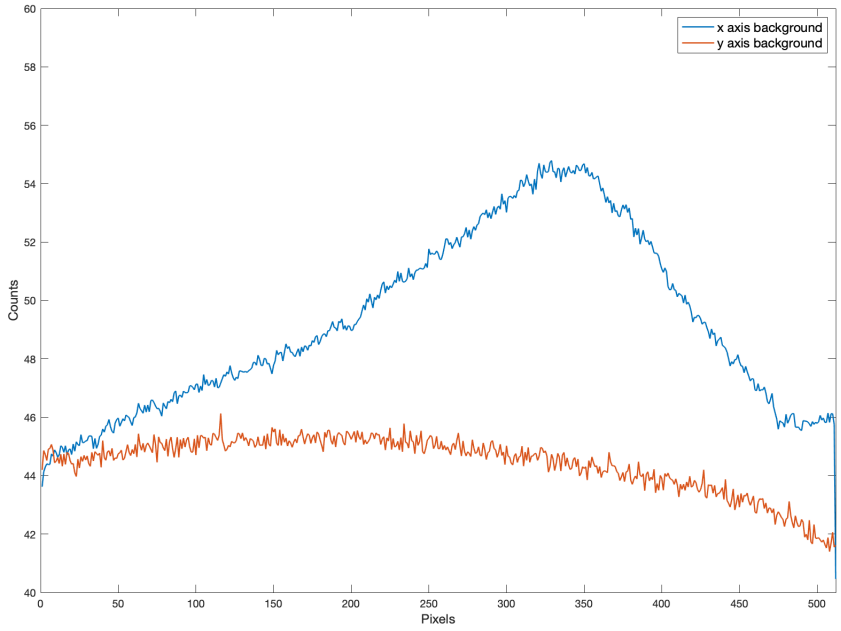


Figure 4.2: x and y profiles of background signal in image

## 4.2 Lucky Imaging

The concept of lucky imaging came from Fried in 1978. Given the time varying nature of the atmospheric turbulence there are instances where the seeing is better or worse than usual. If images are captured on a small time scale the instances of good seeing conditions can be isolated and superior image quality can be achieved. Fried predicted the probability of achieving a good quality frame based on the ratio of the telescope diameter to the Fried parameter ($D/r_0$). When $D/r_0 = 7$ the probability

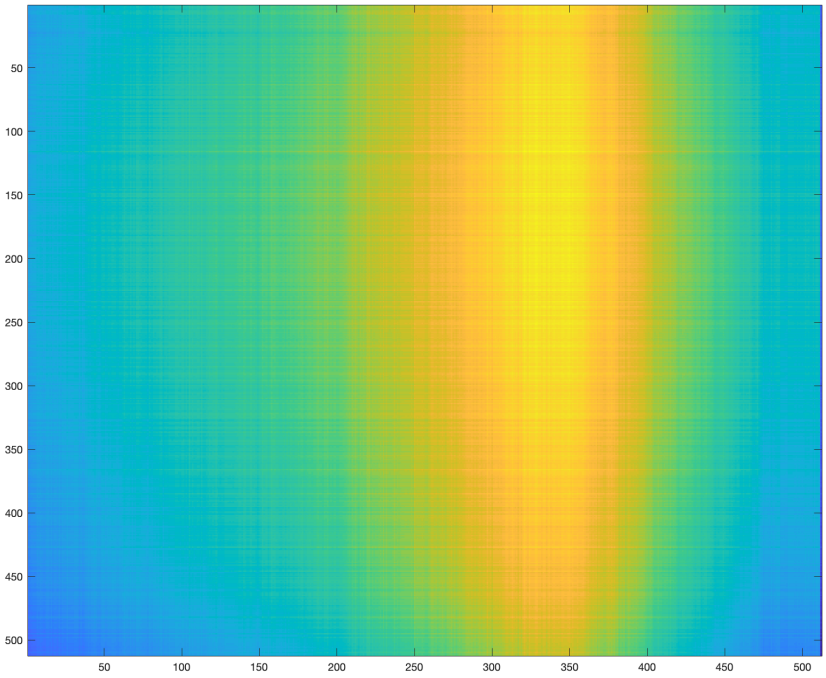


Figure 4.3: Background frame used for correction

is $(2.87 \pm 0.57) \times 10^{-3}$, and as $D/r_0$ becomes larger the probability of capturing a lucky frame decreases [Fried, 1978]. With modern camera and computer systems a probability on the order of $10^{-3}$ is entirely feasible, particularly with high frame rate cameras capable of operating at kHz speeds with low noise.

AOI is designed to operate with an $r_0$ value of 11 cm. With the 1.8 m telescope diameter the $D/r_0$ value for the expected operational conditions is 16. The probability of obtaining a good frame at $D/r_0 = 16$ using Fried's analysis is less than $3.4 \times 10^{-15}$, which is very unlikely. Therefore, there is a low probability that AOI could capture a good frame without the assistance of adaptive optics.

Lucky imaging is combined with the AO correction from AOI to select only the best images for analysis. The combination of lucking imaging and AO has been done previously with the Adaptive Optics Lucky Imager (AOLI) instrument. Operating on the 4.2 m William Herschel Telescope, AOLI was able to produce 0.15" FWHM images with just lucky imaging and no AO [Colodro-Conde et al., 2018]. With an adaptive optics correction the single frame star images were significantly improved.

When operating the system in open loop there is no AO correction so the images captured are degraded by the atmospheric turbulence. Using lucky imaging on open loop images will allow us to select only the images where the influence of the atmosphere is less. The 'lucky' images are selected by setting a threshold on the peak value, and only using images with a peak value above the threshold. Filtering the images based on the peak value is an effective technique as poorer atmospheric conditions result in the energy being distributed over a larger area on the detector and therefore, a lower intensity in the core.

Closed loop images are selected in the same way as open loop. Lucky images can be a result of good AO correction and reduced atmospheric effects. Filtering out the best images was necessary for closed loop operation due to issues experienced with the telescope. A failure of the elevation axis encoders meant that observations were made with only one encoder functioning. This resulted in the telescope movement in the elevation axis being jittery, which was at times introducing more tip-tilt than the AO system could correct. When the AO system would offload tip-tilt to the telescope a noticeable shaking in the image would occur and would appear as if the image was smeared over a large area. This would typically happen at intervals with the same period as the tip-tilt offload setting in the AO system. This confirmed the issue was worsened when a pointing correction was made. The effect of the encoder failure was worse when tracking a LEO object as the telescope would be slewing quickly across the sky, particularly in elevation.

To obtain the images that were not impacted by the jitter and received a good AO correction a threshold based on the peak value was set. Given the telescope shake would smear images the threshold method was effective at filtering out the affected images.

## 4.3 Image Stacking

Image stacking is used to stack multiple frames of the same object to improve signal to noise ratio and image quality. A number of image stacking techniques were used.

### 4.3.1 Peak Pixel

Peak pixel image stacking is a simple method to implement and can be processed quickly. The peak pixel method of stacking involves locating the peak pixel location of each image and using this location as the reference to stack all the images together.

The peak pixel method is most effective on images containing a single star. A star is a point source with a airy pattern PSF expected as the image which has a single peak; therefore, the peak pixel location typically corresponds to the centre of the PSF peak.

Multiple sources or extended objects may not stack correctly when using peak pixel stacking. In a binary star system where the magnitude of the stars was similar the peak pixel in the frame may occur at the centre of the PSF of either star. This can result in the images being incorrectly registered and cause a stacked image where there are three stars. Similarly an extended object image may be equally bright over an extended area and the peak pixel is in a random location resulting in a blurred image when stacking.

### 4.3.2 Centroid

Centroid image stacking relies on computing the centroid of the image as the basis for the stacked images. The centroid can be measured to sub pixel accuracy, meaning that stacking can be performed more precisely. To stack the images with sub pixel precision the images have to be re-sampled, stacked, and then re-sampled to return to the original resolution.

The centroid of the images is measured using the Matlab function regionprops, which can measure a number of properties in an image including the centroid. The weighted centroid property of regionprops is used to find the centroid of the spot of interest. The images are stacked based on the location of the centroid and averaged to normalise the pixel values.

### 4.3.3 Cross Correlation

The cross correlation method performs a cross correlation on each image to find the position where the correlation coefficient is a maximum. Each image in the series is successively cross correlated with the stack so it is registered correctly when it is added to the stack.

The cross correlation is performed using the xcorr2 function in Matlab. In order to allow for offsets in the image location the images are padded with several rows and columns on each side with zero values. The xcorr2 function provides the indices where the correlation coefficient is maximum and the frame added to the stack is aligned with the indices. After the all the frames are stacked the image is resized to a 512×512 pixel frame.

The cross correlation stacking technique provides the best improved results when the image is of an extended object such as a satellite.

## 4.4 Image Analysis

When imaging a point source such as a star a PSF close to an Airy function is expected if there is no aberrations. The inclusion of the telescope secondary and spider will mean the diffraction pattern is not a perfect Airy function; however, it will be very similar. The performance of the system can therefore be measured by comparing the PSF to an ideal case. The ideal PSF is approximated by a Gaussian function, which can be constructed based on the known parameters of the system. The ideal PSF in 1 dimension is

$$psf = a_0 \exp -\frac{(x - x_0)^2}{2\sigma^2} \tag{4.1}$$

where $a_0$ is a scaling factor, $x_0$ is the centre of the PSF, and $\sigma$ is the standard deviation. The value of sigma is related to the spot size of the image with the full width half maximum (FWHM) defined by

$$FWHM = 2\sigma\sqrt{2\ln 2} \tag{4.2}$$

The FWHM of the spot is also related to the system parameters by

$$FWHM = 2\lambda F \tag{4.3}$$

where $\lambda$ is the imaging wavelength and $F$ is the F number of the imaging system. Therefore, the standard deviation of the ideal PSF will be

$$\sigma = \frac{\lambda F}{\sqrt{\ln 2}} \tag{4.4}$$

### 4.4.1 Strehl Ratio

The Strehl ratio provides a measure of the performance of the system relative to the ideal PSF that is modelled. An ideal PSF is generated with the peak value ($a_0$) calculated such that the integral of the ideal psf is equal to the sum of the spot in the captured image. The Strehl ratio is given by

$$Strehl = \frac{I_{measured}(p)}{I_{ideal}(p)} \tag{4.5}$$

Where $I_{measured}(p)$ is the peak value of the measured intensity profile of the image and $I_{ideal}(p)$ is the peak value of the ideal PSF intensity profile.

## 4.5 Blind Deconvolution

Blind deconvolution is an image processing method where an image can be recovered without any prior knowledge of the underlying PSF [Lam and Goodman, 2000]. Some knowledge may be known about the PSF but an approximation is still made. In the case of imaging an object through the atmosphere, blind convolution can provide improvement of image quality. The true PSF of the object is not known and also the effects of the atmospheric turbulence are constantly changing and not known. Therefore, to perform the deconvolution and remove the blur an estimation must be made.

From a single frame it is difficult to restore an image to its true form as there are an infinite number of possible solutions. One way to solve this issue is to use multiple frames and iteratively solve to remove the effects of the unknown turbulent distortions [Ayers and Dainty, 1988]. The process of using a set of images to iteratively restore an image is known as multi-frame blind deconvolution (MFBD). These methods have been applied to astronomical observations, and also for space situational awareness purposes. MFBD has shown it can significantly improve image quality on satellite images. Schulz in 1997 was able to restore an image of the Hubble Space Telescope from a set of 656 images capture on the Air Force Maui Optical Station. This telescope is located at the top of Haleakalã, which is one of the best sites in the world for astronomical observations, so seeing conditions would be excellent reducing the atmospheric effects compared to a site like Mount Stromlo. The effectiveness of MFBD has been further demonstrated with satellite imagery where distorted images are restored to reveal the structure of the satellite [Fan and Nagy, 2012; Hope et al., 2019].

For the MFBD performed in this thesis the online multi-frame blind deconvolution algorithm developed by M Hirsch et al. is used [Hirsch et al., 2011]. This has been demonstrated on both astronomical and satellite images. The online blind deconvolution (OBD) function is available as a Matlab script and is used to obtain MFBD processed images from a set of AOI collected data.

Chapter 5

# AO System Operation

This chapter details the results that are obtained from operation of AOI. First the results of running the system in the lab utilising the calibration source to illuminate the system. This process was used to verify the operation of the AO operation and identified several issues, which were rectified before meaningful results could be obtained from on-sky operations. The DM was found to be introducing defocus to the system and was given a command to produce a flat surface. The dichroic beamsplitter also presented issues as it was introducing astigmatism, and this optic was changed to remove the astigmatism.

Initial on-sky operation of AOI began by imaging stars. The performance of the AO system was analysed by comparing images captured in open loop to those with an AO correction. Significant increase in performance was obtained when operating in closed loop. Observation of binary star systems was also used to determine the plate scale of the system, which was necessary for making angular measurements.

Results from data recorded of satellites in LEO are presented in Section 5.3. The process to select objects for observation and the steps to make those observations are outlined. AO corrected images of several objects were obtained, which revealed features that were not apparent without the adaptive optics. The use of MFBD further improved the detail in images captured of a satellite, which allowed for features to be resolved and their size measured.

Tracking of geostationary satellites using astrometry was also implemented. The method in which a satellite position can be determined by measuring the image location relative to a known reference star is outlined. Simulated tracking is performed by adding a moving signal at the rate a GEO satellite would pass through the frame.

## 5.1 Calibration

Verification of the AO system operation was done using the calibration source. The calibration subsystem uses a broadband light source input to the system via a 10 µm diameter core fibre that is then collimated onto the DM. The calibration source is used to register the DM actuator grid to the wavefront sensor. A poke matrix is applied to the DM where it successively pokes each actuator in and out and measures the effect on the wavefront sensor. The interaction matrix generated can be used to test how well the actuators are aligned to the edge of each subaperture. The wavefront sensor beam expander relay lenses can be adjusted to modify the magnification between the DM and WFS and the WFS mount translated in x and y for registration.

The calibration source was also used to flatten the DM when powered on. When AOI was first put together there were aberrations seen on the WFS and the quality of the image on the imaging camera was poor. A collimated laser beam was reflected off the DM and viewed on a shear plate. The test showed that the beam was no longer collimated indicating the DM was introducing defocus to the system. A series of commands were applied to the DM so a reflected beam would remain collimated when viewed on the shear plate. Figure 5.1 shows the DM commands needed to flatten the DM. The colour bar represents the actuator stroke in microns, with a 5 µm peak to valley shape required to flatten the DM. Some astigmatism, coma, and spherical aberration is also seen.

The surface figure obtained was decomposed into Zernike modes to determine if any modes are dominating. Figure 5.2 shows the scale of each of the first 12 Zernike modes. The most significant mode is the fourth mode, which is the defocus term.

After flattening the DM the beam transmitted to the WFS showed minimal aberrations; however, the poor image quality at the imaging camera remained. The beam is split to the imaging arm by reflecting off the dichroic beamsplitter. The effects of a dichroic coating to image quality have been documented by Semrock who supply optical coatings [Prabhat and Erdogan]. They found that the dichroic coating could cause bending on the optic surface resulting in a defocus. When the beamsplitter is placed at a 45 degree angle, as it is for AOI, the resultant aberration is astigmatism. Figure 5.3 shows an image taken with the dichroic beamsplitter in place.

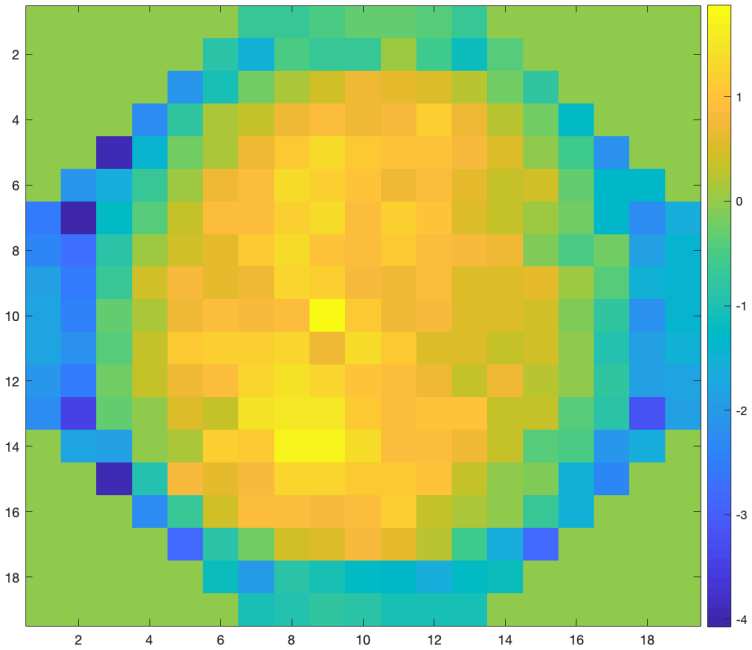


Figure 5.1: DM commands required to flatten the DM

This image was captured when the imaging camera was placed at the optimal focus position and the intensity was highest. If the camera was moved out of the focal plane the image became elongated horizontally or vertically, which occurs when the system has astigmatism. The two elongated spots that are observed show a significant deviation from the expected image of a single bright spot, which is circularly symmetrical. A non common path aberration (NCPA) correction was used in an attempt to eliminate the aberrations introduced by the dichroic beamsplitter reflecting surface. The NCPA correction iteratively applied a disturbance to the DM and used the spot on the imaging camera as a metric for the correction. The peak intensity of the spot was maximised with the NCPA correction. With the NCPA there was still considerable astigmatism seen in the images, which indicated that the compensation was not enough. The dichroic beamsplitter was removed from the AOI and the beam reflected off the dichroic surface was measured with an interferometer. It was found the dichroic has a defocus with a peak to valley of six waves at the testing wavelength. Such a large deformation cannot be pre compensated with the DM, thus a decision was made to replace the dichroic mirror.

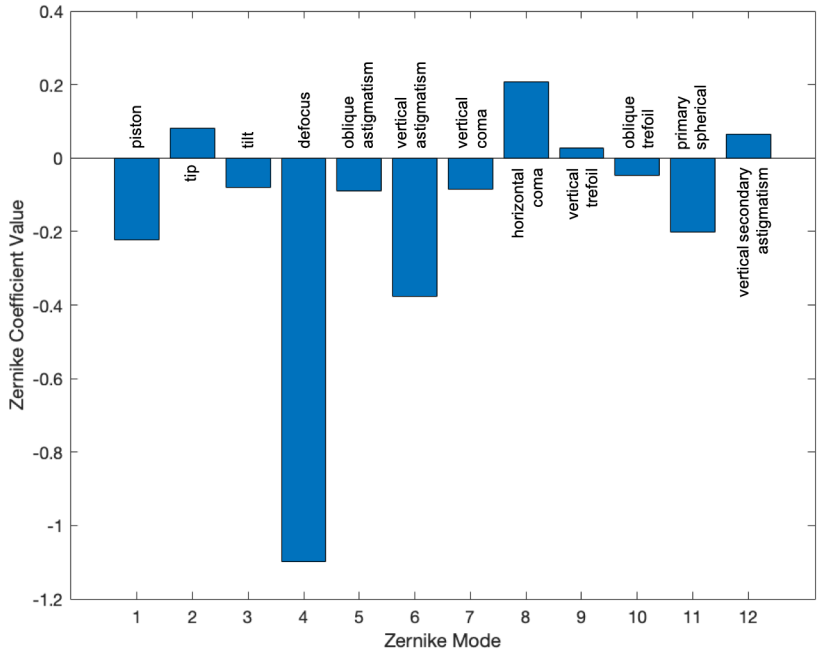


Figure 5.2: Zernike mode coefficient for DM flattening

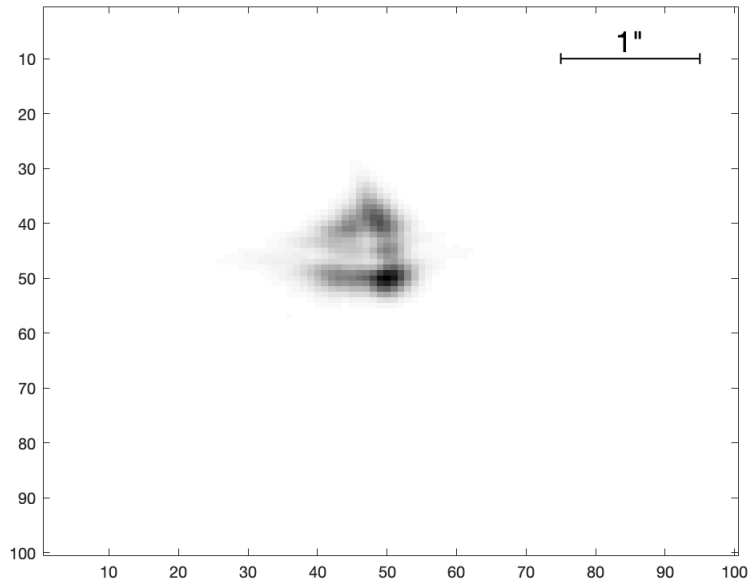


Figure 5.3: Image of calibration source with astigmatism caused by dichroic beam-splitter

To avoid the negative effects of the dichroic coating a decision was made to place a standard broadband beamsplitter that would transmit 70% of the light and reflect the remaining 30%. A longpass filter would be used so only 800 nm and above wavelengths would be transmitted to the imaging camera. This beamsplitter would compromise the flux to both the wavefront sensor and imaging camera with 30% less flux to the WFS and 70% less flux to the imaging camera; however, time and cost constraint prevented purchasing a new dichroic beamsplitter with higher optical quality. With the 70/30 beamsplitter in place the image quality was significantly improved. Figure 5.4 shows an image of the fibre source with the new beamsplitter with the cross sectional profile showing a spot that would be expected for a system with minimal aberrations.

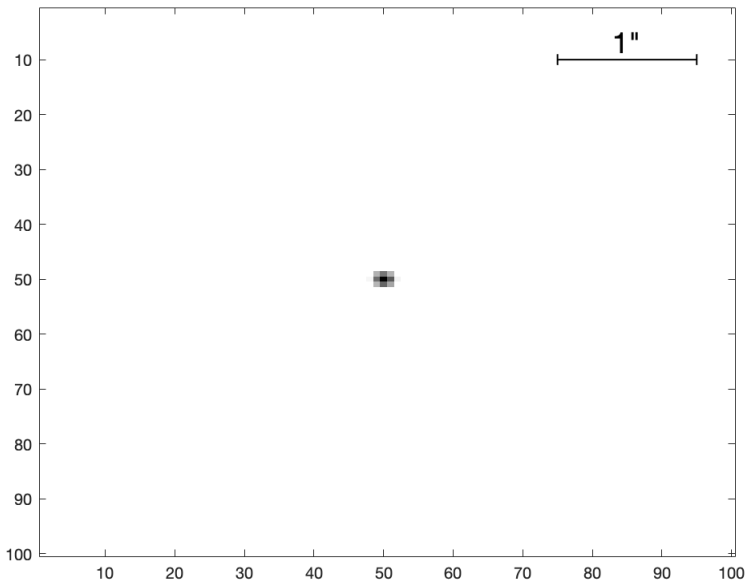


Figure 5.4: Image of calibration source with 70T/30R beamsplitter

Once alignment between the DM and WFS is complete a reconstructor is built. An interaction matrix is built by pushing and pulling each actuator and is used to generate the reconstructor. The interaction matrix is a $240 \times 408$ matrix which gives the slope measurement for each of the 204 subapertures in x and y for the 240 active actuators across the pupil. The reconstructor is generated by inverting the interaction matrix; however, as it is not square a pseudo inverse is made via SVD.

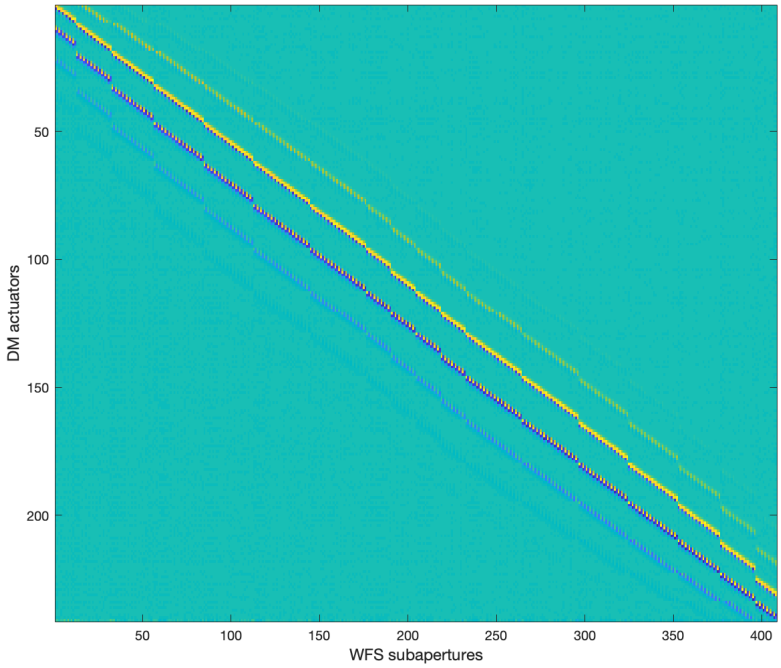


Figure 5.5: Interaction matrix generated from single actuator poke

## 5.2 Star Observation

On-sky testing of AOI was conducted using bright stars. These were ideal candidates for AO performance testing as they are point sources allowing for imaging performance comparison to an ideal PSF. Stars are also easy to locate and move slowly at the sidereal rate so the maximum 2 kHz rate of the AO system is not required to maintain a good AO correction.

### 5.2.1 Open Loop

Open loop images of a star represent the images expected with no AO correction. The images were captured at the maximum imaging frame rate of 60 Hz, and a threshold was used to select the top 1% of frames based on peak pixel value. Figure 5.6 shows a single frame, which has been bias and background corrected. Compared to the images of the calibration source in Figure 5.4 the open loop star image has

significant degradation in the image quality. The energy is much more dispersed with the light from the star spreading over a 50×50 pixel region. When viewing a series of images the location of the image is also moving between frames due to the jitter introduced by the atmospheric turbulence.

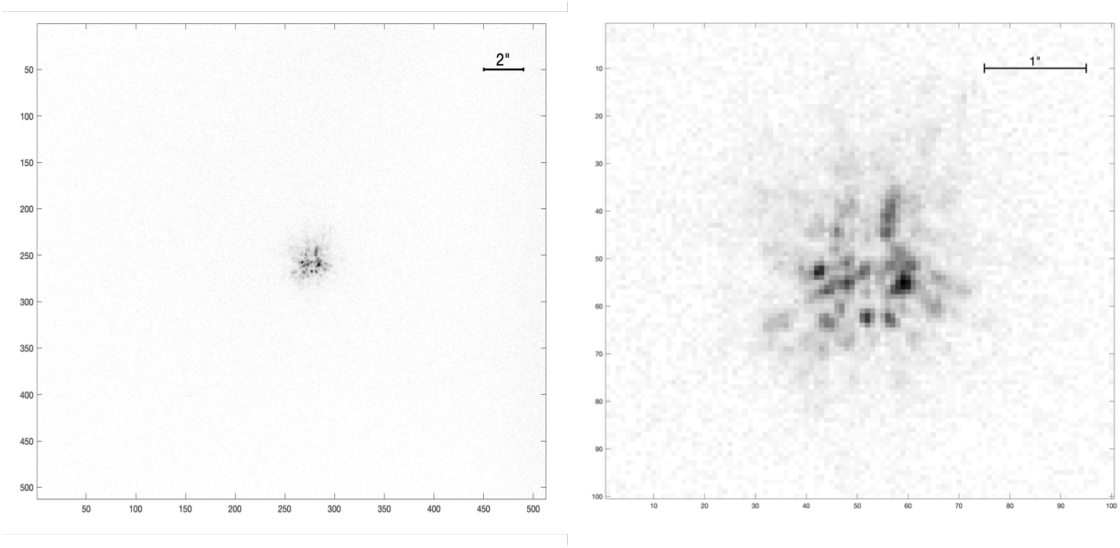


Figure 5.6: Left: Full frame image of star in open loop. Right: 100×100 pixel section of open loop star image

Thresholding based on peak pixel and stacking frames as discussed in Chapter 4 is used to improve the quality in the images. Figure 5.7 shows the effect of stacking multiple images above the threshold for 'lucky' images. By shifting and stacking the images the jitter that is seen in Figure 5.12 is removed so each star image is stack onto each other. The spot itself is still much larger than the diffraction limited spot size due to the amount of speckle in a single open loop frame.

### 5.2.2 Closed Loop

Closing the AO loop allows AOI to correct for the atmospheric turbulence and improve the images produced. Figure 5.8 shows the result of closed loop operation on the same star as in Figure 5.6. As with the open loop data, lucky imaging has been applied to the image to filter out only the best frames, and these frames have been stacked together.

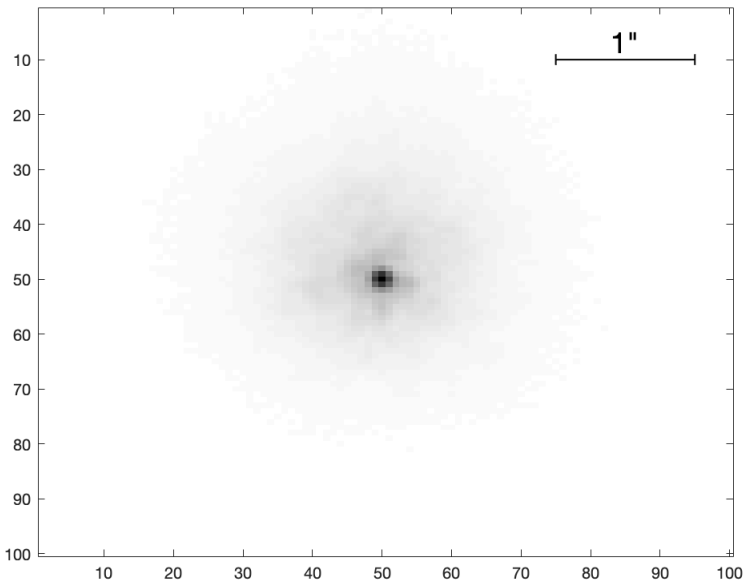


Figure 5.7: Stacked open loop image of star

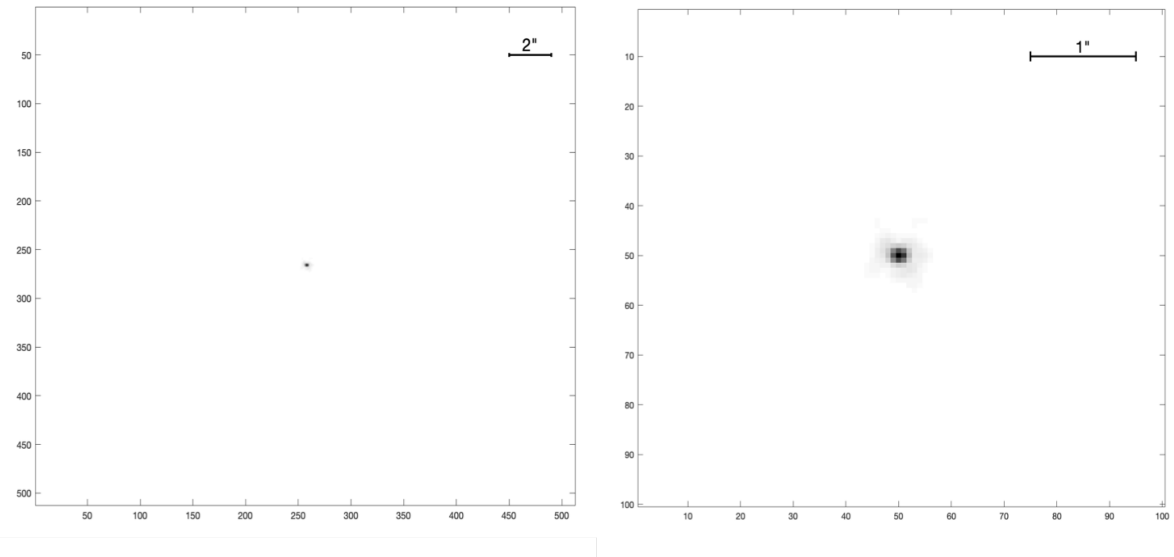


Figure 5.8: Left: Full frame image of star in closed loop. Right: 100×100 pixel section of closed loop image

### 5.2.3 Binary Stars

Binary star systems were observed to confirm the plate scale of AOI. If the angular separation of two stars is known then the measured separation in an image can be translated to an on-sky angle. Figure 5.9 shows a stacked image of a binary system in closed loop.

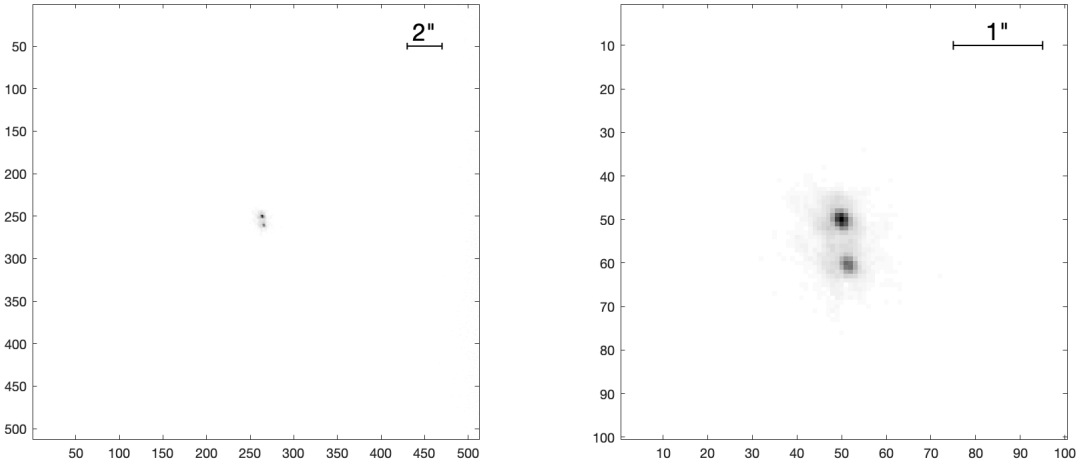


Figure 5.9: Left: Full frame closed loop image of binary star system. Right: 100×100 pixel frame closed loop image of binary star system

Separation of the two stars was measured by determining the centroid of the two stars. The regionprops function of Matlab was used to find the weighted centroid. The total distance between the two centroid positions was calculated to be 10.59 pixels. The star separation was known to be 0.5 arcseconds meaning the plate scale of the system is 0.0472 arcseconds/pixel.

It is noted that to get an accurate measure of the plate scale the separation of multiple binary star systems should be measured. Due to time constraints and telescope access restrictions this did not occur; however, in future operation of the system these measurements will be made.

When the plate scale is known the effective focal length of the compound imaging lens can be calculated by

$$ps = \frac{1}{M} \tan^{-1} \frac{p}{EFL} \tag{5.1}$$

where M is the magnification of the system from the telescope to imaging lenses, p is the pixel size on the imaging camera, and EFL is the effective focal length. The magnification of the system is known as the telescope primary mirror is 1.752 m diameter and the beam size in AOI is set by the DM so is 24.5 mm. The imaging camera has 16 µm pixels, so using equation 5.1 the effective focal length of the imaging lenses is calculated to be 893.6 mm.

### 5.2.4 Analysis

Stacking the open loop frames results in an improved image as shown in Figure 5.7. As each of the selected frames are shifted and stacked, the resultant image is better as what would be expected for a long exposure as the tip-tilt influence is reduced. Figure 5.10 shows a cross section of the stacked image in Figure 5.7. There is a central peak and is surrounded by a large halo due to the speckle in each of the open loop images.

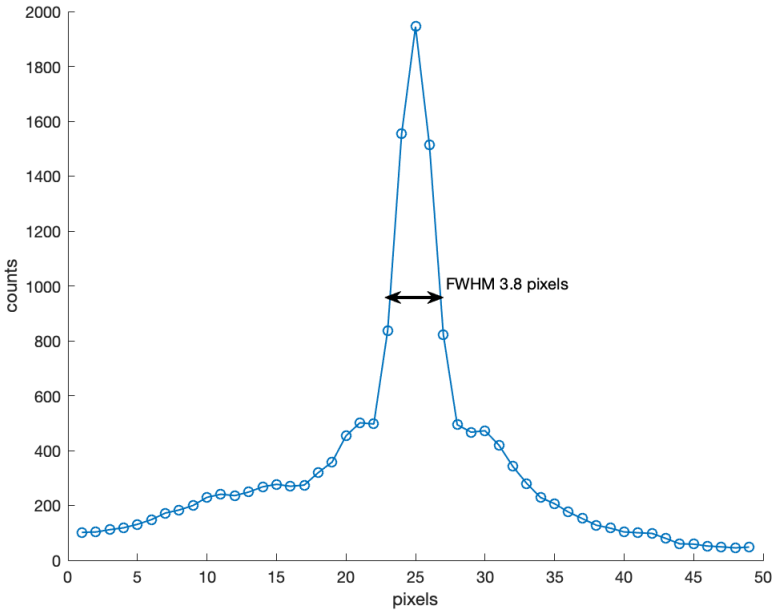


Figure 5.10: Cross sectional profile of stacked open loop image of star

The Strehl ratio for the stacked open loop image was calculated to be 4.2%. There is significant energy contained in the halo surrounding the central peak, which causes the Stehl ratio to be so low. The FWHM of the central peak is 3.8 pixels.

The adaptive optics correction results in significantly improved star images compared to open loop. We can easily see the effect of the atmosphere causing large amounts of speckle and significant tip/tilt in the image. The peak intensity in the closed loop image is greater by a factor of 4 over the open loop, which indicates that the energy is more concentrated into a smaller area. When viewing the 100×100 pixel region of the closed loop image in Figure 5.8 the first Airy ring is visible. This indicates the AO correction is effective as there are artefacts of diffraction rather than the image dominated by the aberrations introduced by the turbulence. The cross sectional profile in Figure 5.11 also shows the bump, which is likely the first diffraction ring. The Gaussian fit applied to the cross section has good agreement in the central peak and the FWHM of the peak is 2.81 pixels.

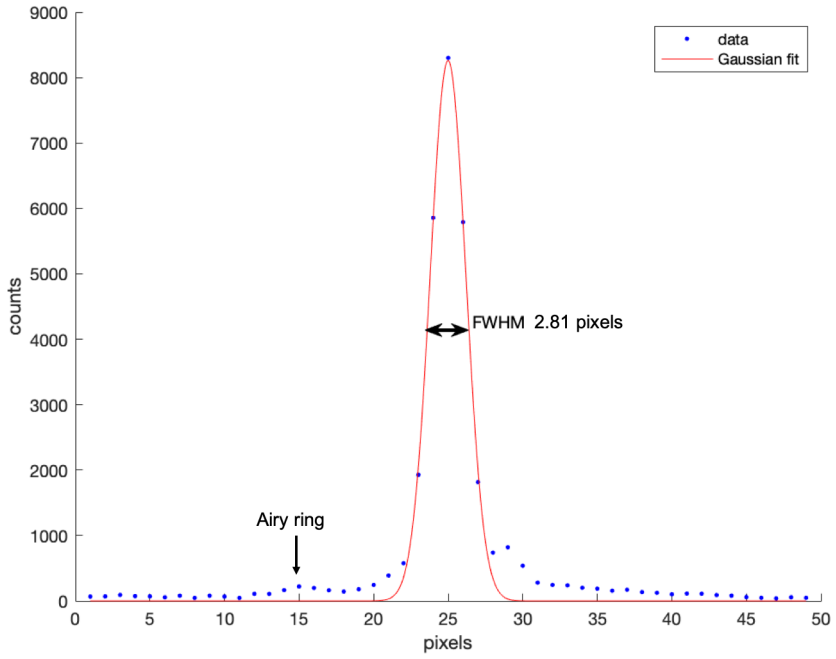


Figure 5.11: Cross sectional profile of stacked closed loop image of star

The Strehl ratio of the closed loop image is calculated to be 34% which is in agreement with the design specification of 30%. When compared to the Strehl ratio achieved for a stacked open loop image of 4.2% there is a clear improvement made by the adaptive optics. The peak intensity of the stacked closed loop image is larger than the stacked

open loop image by a factor of 4. This is due to the energy being concentrated onto fewer pixels. The FWHM of the closed loop image is 2.81 pixels compared to 3.8 for the open loop stacked peak. Given the plate scale of 0.0472 arcseconds/pixel the FWHM of the closed loop image is 0.13 arcseconds.

The magnitude of the jitter in open and closed loop is shown in Figure 5.12 where the change in the centre of the star is plotted for an image session. The movement of the spot is measured in arcseconds relative to the mean position in the image session. The first half of the data is with open loop operation, which then transitions to closed loop. In this plot lucky imaging has been applied so only frames above a specified threshold are met. This removes the effects of the telescope shake when applying tip-tilt offload and extremely bad cases of turbulence. The cumulative mean of the image distance to the average position is also overlayed for the open loop and closed loop data. The cumulative mean position is 0.43 arcseconds, which is a shift of approximately 8 pixels. There are also large jumps in the position of the star up to 1 arcsecond which is a >20 pixel shift in position.

Figure 5.12 shows that the stability of the star image on the detector was improved by the adaptive optics correction. The variation in the position becomes much smaller when the loop is closed and the largest deviation from the average position is <0.3 arcseconds. The cumulative mean is 0.08 arcseconds, which is an improvement by a factor of 5 over the open loop image motion.

The error transfer function (ETF) was plotted when observing a star in Figure 5.13. The WFS was running at the maximum rate of 2067 Hz and the slopes were recorded for open and closed loop observations on the same star. The ETF was determined by computing the ratio between the DM error and commanded shape, and the power spectrum density was plotted as a function of frequency along with analytical fit of the data. The error rejection bandwidth was measured to be 95 Hz, and is where the measured ETF crosses ideal curve.

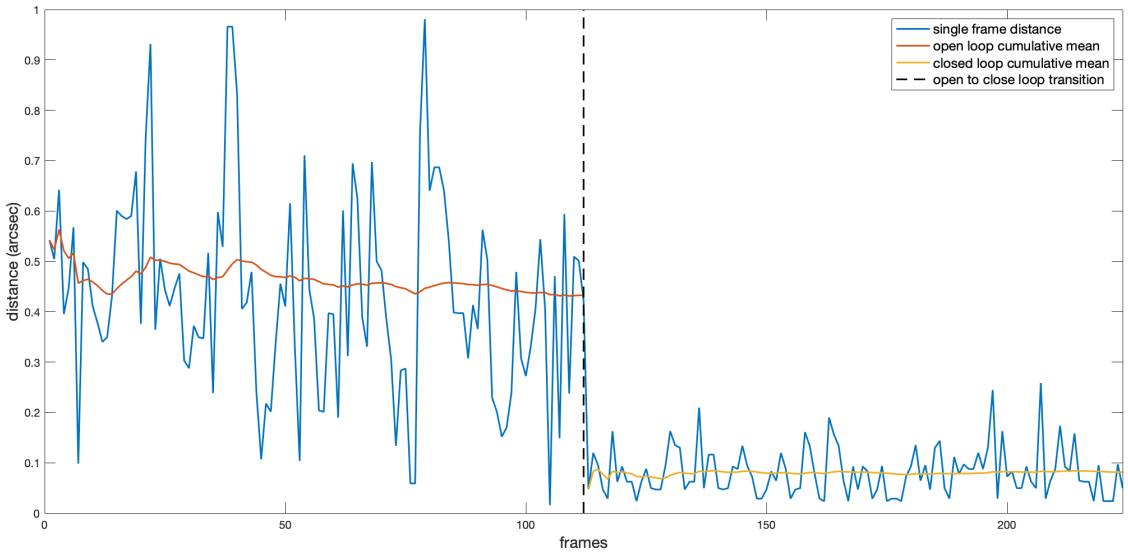


Figure 5.12: Star position in each frame relative to mean position of open loop session

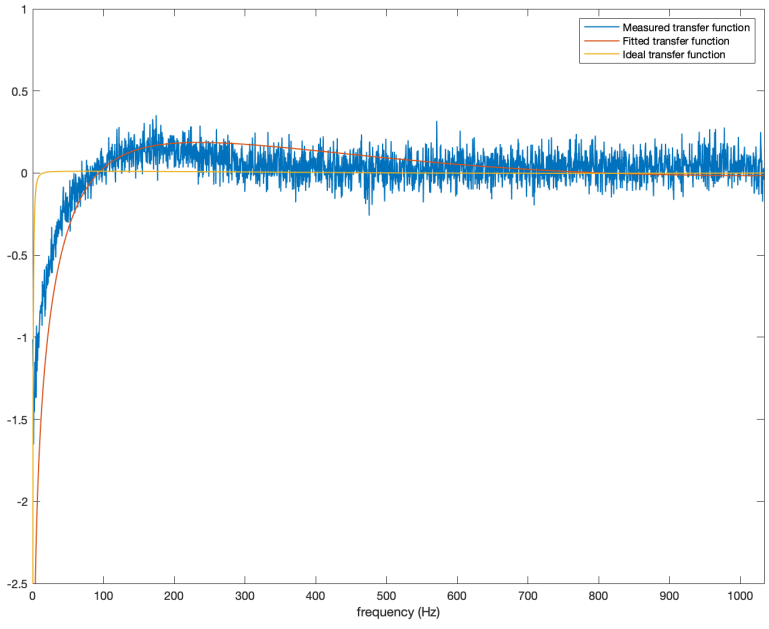


Figure 5.13: Error transfer function of star observation at 2067 Hz

### 5.2.5 Operational Limitations

Several operational issues occurred that prevented the AOI from operating at its optimal potential. The outer subapertures of the WFS could not be illuminated when observing stars or satellites through the telescope. The illumination of the subapertures is shown in Figure 5.14. No clipping was evident with any optics on the optical table it is likely caused somewhere along the coudé path. The ring of subapertures was either poorly illuminated or not at all, which resulted in the issues with the AO correction.

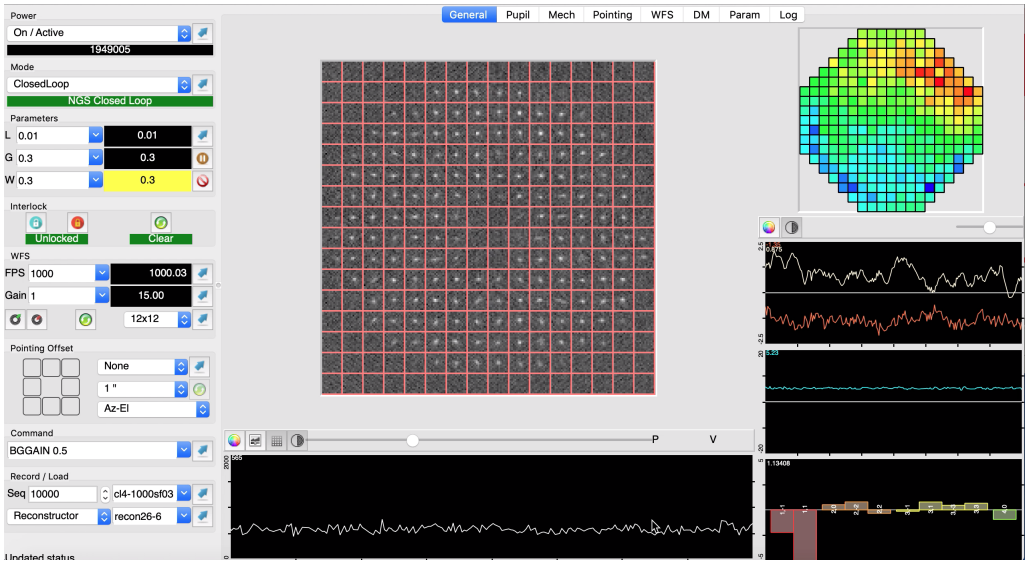


Figure 5.14: Screenshot of RTC GUI with outer subapertures not illuminating

Operations were also hampered by poor seeing conditions, and suitable AO corrections were not possible on some observation nights. The system is designed to work in seeing conditions of 2 arcseconds or better; however, some nights had seeing as bad as 4 arcseconds. Some of the poor seeing conditions may be attributed to dome seeing. During observing nights the dome was opened as early as possible to reduce this effect; however, this was not always possible as handover of the telescope was sometimes just before observations began. Figure 5.15 shows a screenshot of the RTC GUI during very poor seeing conditions. Each of the subapertures is almost completely illuminated by the star rather than a 2×2 pixel region in ideal conditions.

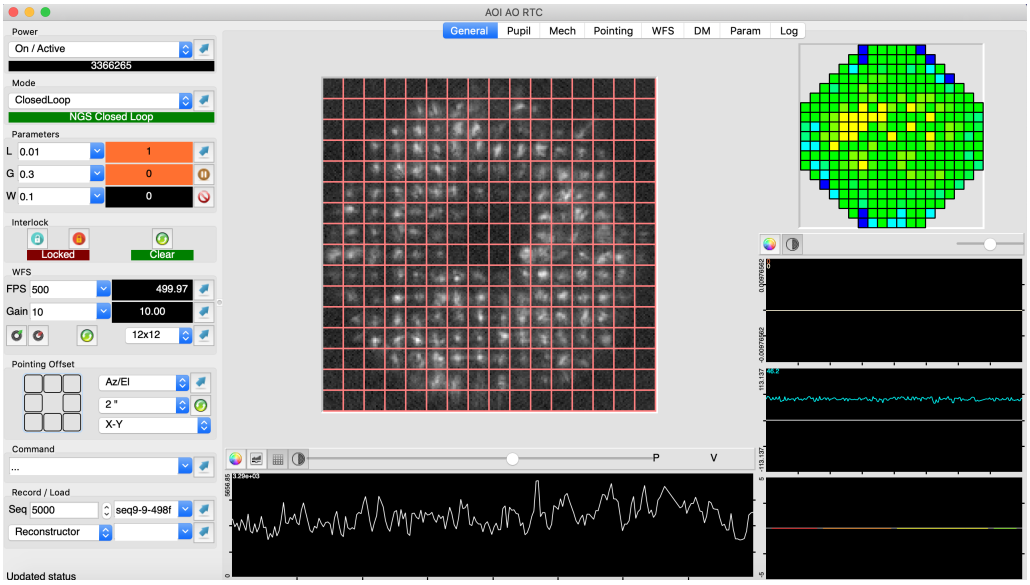


Figure 5.15: Screenshot of RTC GUI during poor seeing conditions

Operations were also impacted by limited availability of clear nights. After AOI became operational there was routine cloud that prevented any operations. Large bushfires within the region also had a significant impact in operations. The fires created a hazardous smoke haze, which persisted over a period of at least two months. The smoke was often thick enough to completely block out starlight. Operations were also limited to prevent contaminates such as ash settling on the telescope mirrors.

The issues discussed with the inability to smoothly offload tip-tilt to the telescope impacted the correction of the AO system. The process of offloading tip-tilt to the telescope would cause a smearing effect on the image as the telescope moved and the AO system attempted to recover. Figure 5.16 shows the effect of the telescope shake when observing a binary star. The two star images become streaks as the position changes over the integration of the camera. Images such as these would be filtered out during the lucky imaging process; however, as the telescope shake was a regular occurrence the number of usable images was diminished.

Tip-tilt would routinely build up on the DM and consume most of the available stroke. If it was offloaded, the shake of the telescope resulted in the DM using more tip-tilt stroke to maintain stability of the image position. Figure 5.17 shows an example of the DM when the tip-tilt had built up during observations. The DM was close to its maximum tip-tilt stroke conditions at this point of 15 µm.

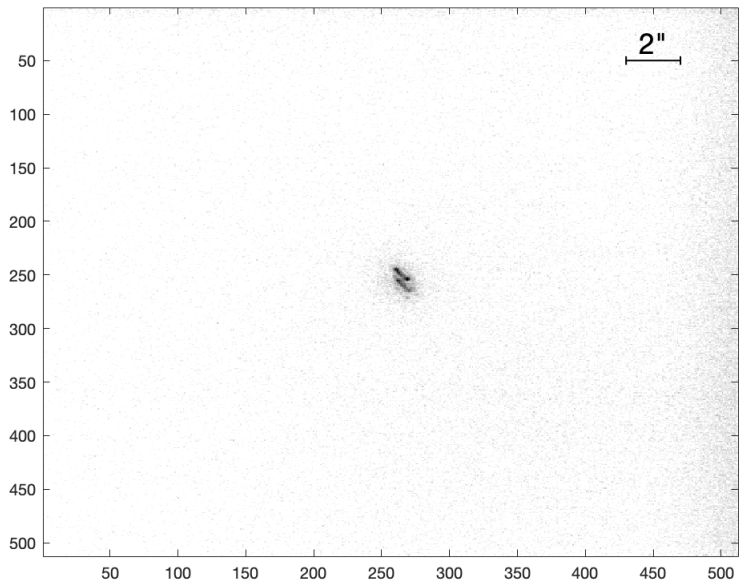


Figure 5.16: Binary star image when tip-tilt offloaded to the telescope

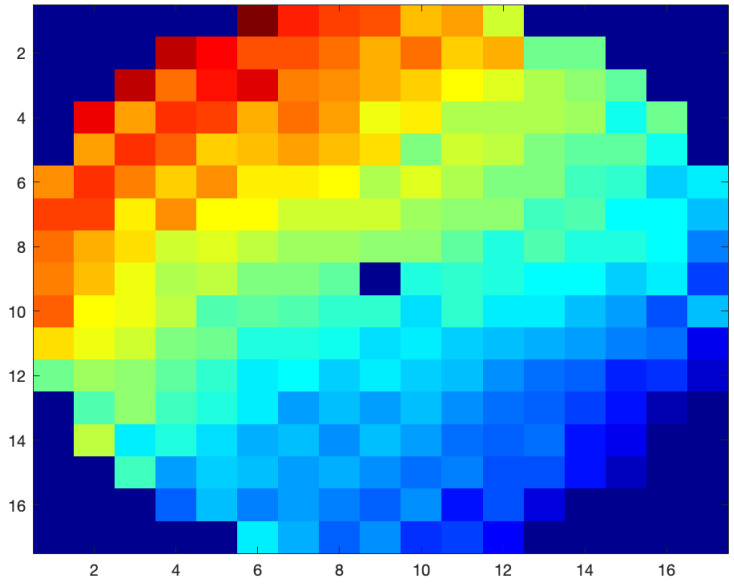


Figure 5.17: DM shape with large tip-tilt during observations

The DM shape in Figure 5.17 is visually dominated by tip-tilt. This is confirmed by decomposing the DM shape into Zernike modes in Figure 5.18. The left image shows the contribution of the first 12 modes to the DM shape. Each of the modes is plotted on the same scale with the tip and tilt modes contributing the most. The right image shows the Zernike coefficient value with the tip and tilt modes much larger than the others.

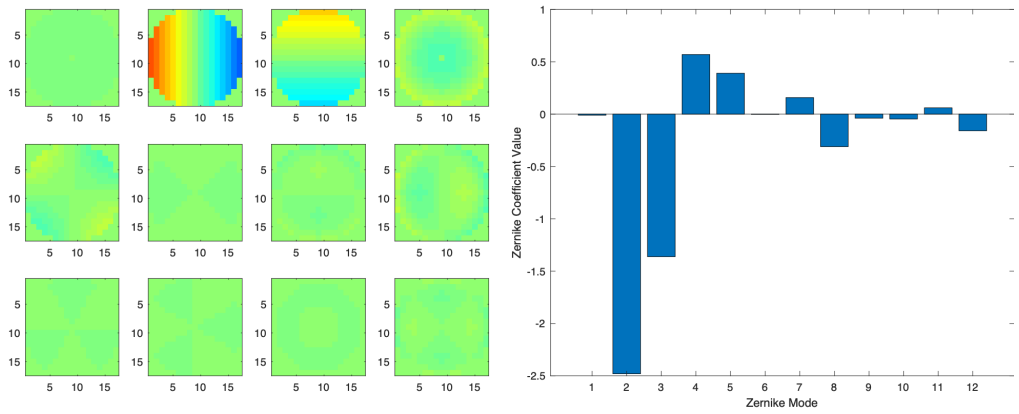


Figure 5.18: Left: Visualisation of first 12 Zernike modes for DM shape plotted with the same scale. Right: Zernike coefficients of the first 12 modes

## 5.3 Low Earth Orbit Imaging

Imaging of low Earth orbit (LEO) targets is conducted to capture high resolution images and determine characteristics of the object. This section will describe the criteria for selecting a target, the process to capture images, and the results obtained for AOI operation.

### 5.3.1 Target Selection

Prior to observations a list of suitable targets were selected. The 'Heavens Above' website was used to determine which satellite will be viewable from Mount Stromlo [Heavens-Above, 2019]. There are several considerations used when constructing the target list:

- Brightness – The Maximum apparent brightness is predicted for each satellite, which will occur at its maximum altitude. Brighter objects are preferred and a threshold of between 3.5 and 4.0 is used for filtering the list for suitable targets.

- Maximum elevation – The track of the satellite over the observatory will see it rise, track across the sky, and set over a time frame of approximately 10 minutes. Satellites that reach a high elevation as they pass over the telescope are preferred as they typically have a longer track time allowing for more data collection. Additionally the elevation of the object affects the amount of airmass

the telescope must look through. The higher the elevation the closer the airmass is to 1, which will reduce the effect of the turbulence and allow improve performance of the AO system. Objects with an elevation above 70 degrees are preferred.

- Time of track – Only one satellite can be tracked at any given time so targets are selected so that there are no concurrent tracks and minimal overlap between the tracks. When an object is setting and is below 40 degrees elevation the AO system is not effective so no usable data can be collected, thus the track can be abandoned if another target of interest is about to rise. In situations where two objects are visible at the same time then the one with higher brightness or maximum elevation will be chosen. Additionally, satellites are generally preferred over rocket bodies or debris as they will have more complex structure making it easier to see the effects of the AO correction.
- Range – The orbit altitude affects how quickly an object transits the sky. If a satellite has a low altitude the wavefront sensor needs to run faster to make an effective correction. There have also been issues with the telescope tracking at high slew rates so objects with an altitude of 800 km or higher are usually selected.

When the suitable targets are selected a list is created which includes the name of the object, NORAD ID number, rise time, set time, and peak brightness. The NORAD ID number is a unique number assigned to every object that is tracked. This number is needed to set the telescope to track the object of interest.

### 5.3.2 Telescope Operation and Data Collection

Imaging of objects with AOI in LEO is only practical during terminator, which is a period of time shortly after sunset or before sunrise. In this period some objects in LEO are still sunlit, which allows the reflected sunlight to be collected by the telescope, and the sky is dark so the signal can be seen over the background. The process for tracking a satellite and closing the adaptive optics loops is described below.

The NORAD ID and time the track is active are entered into the telescope computer before the track is set to begin. The telescope control computer will collect the track of the specified NORAD ID. If the track is entered before the object rises above the horizon the telescope will move into position so it is pointing in the direction of

where the satellite will rise from and begin to move once the satellite begins to rise. If the satellite has already risen the telescope will immediately go to the current position and follow the track. The wavefront sensor speed is lowered to 200 – 500 Hz and EM gain set to 300 so the object can be seen if it passes within the field of view. If the object cannot be seen on the wavefront sensor a spiral search in conducted with 30 arcsecond steps until the satellite becomes visible. If nothing is found after moving more than 4 arcminutes off the track the offset is reset and another spiral search is started.

When the satellite is visible on the wavefront sensor the telescope is offset with 1 – 2 arcsecond biases in azimuth and elevation to centre the spots on the wavefront sensor. After this the frame rate of the wavefront sensor is increased to at least 1 kHz and the EM gain adjusted so there is sufficient flux in each subaperture. With the spots centred on the wavefront sensor there should also be an image at the centre of the imaging camera. The AO loop is then closed, which will work to keep all the spots centred in each subaperture. The leak, gain, and spatial filtering is adjusted manually after the loop is closed. The camera speed and gain is also adjusted as necessary.

Once the loop is closed on the AO system imaging data is recorded. The imaging camera is nominally run at 60 Hz and the EM gain used to increase the signal. If an increase in EM gain does not result in sufficient flux the frame rate can be dropped to 30 Hz. Images are recorded with the NORAD ID number in the name for identification when processing the images. Sequence data is also recorded from the wavefront sensor while the loop is closed.

When the telescope is close to zenith tracking can become difficult and the loop is opened. Once above 80 degrees elevation the telescope is tracking so quickly that it sometimes cannot keep up with a LEO satellite. Additionally the movement can become unstable due to the high slew rate which causes too much jitter in the image.

The best AO correction has occurred when the object had an elevation between 40 and 60 degrees. It was expected that better AO correction would be at elevations close to zenith due to the minimum in airmass; however, the telescope had difficulty tracking smoothly when slew rates were high resulting in additional tip-tilt that the AO system could not compensate. During observations the telescope had a fault with the elevation axis encoders and was operating with only one functioning. When offsets were made in elevation the movement was very coarse and is likely the cause

of the additional tip-tilt observed when the telescope is required to slew quickly in elevation. During closed loop operation the AO system is continually providing az-el adjustments to the track to offload tip-tilt from the DM. As discussed in Section 4.2 when the tip-tilt was offloaded to the telescope this typically resulted in significant shake in the observed images and any images captured during the tip-tilt offload were rejected.

### 5.3.3 LEO Imaging Results

Initial closed loop images were captured of Envisat, a defunct environmental testing satellite launched by the European Space Agency (ESA). The closed loop images captured of Envisat are shown in Figure 5.19. Cross correlation stacking is used to stack the top 1% of frames based on peak pixel value. In the image there are two distinct features that can be resolved. These are likely to be the body of the satellite and the solar panel array which extends out from the body as shown in Figure 1.9. The overall correction of the image is poor and only allows the two large features to be resolved. The shape of the two features cannot be seen in the image. Atmospheric conditions on the night of the observations was very poor with seeing estimated to be between 2 and 4 arcseconds. AOI is designed to operate in seeing conditions of less than 2 arcseconds; therefore, the conditions were beyond where the AO correction can be expected to be effective.

Observations in good seeing conditions yielded improved performance over what was seen with the correction applied to the Envisat images. Figure 5.20 shows a stacked image of Cosmos 1656 while running in open and closed loop where the seeing was estimated to be 1.5 arcseconds. The individual frames were again stacked together using cross correlation to determine the location where they best match each other for both open and closed loop.

The left image in Figure 5.20 shows the image captured with no AO correction. Stacking is done with cross correlation using the best frames using a peak pixel threshold. In the open loop image there are no features of the satellite which can be resolved. There is evidence of something extending at the top of the satellite but the blurring effect would make it difficult to confirm that feature without prior knowledge from the closed loop image.

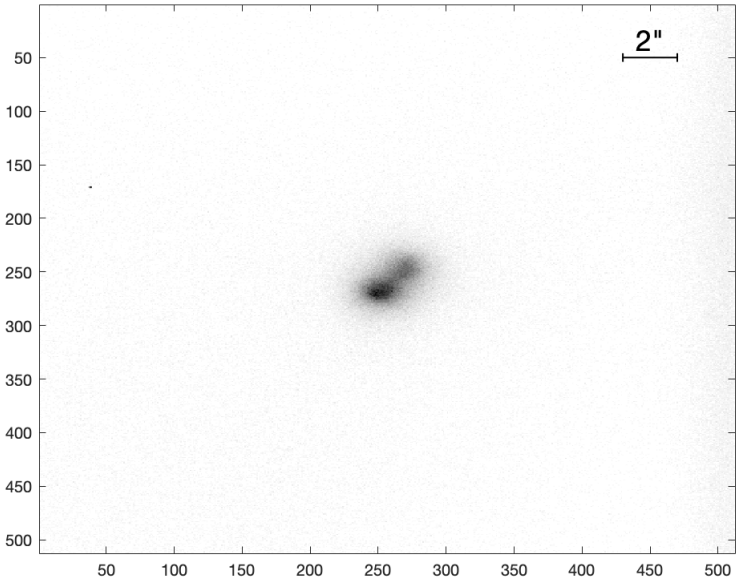


Figure 5.19: Closed loop image of Envisat with cross correlation stacking

The closed loop image on the right of Figure 5.20 shows the stacked closed loop image. The AO loop was set to a rate of 1 kHz during the image capture of Cosmos 1656 and the images were captured while the satellite was at an elevation of 48 degrees. At this elevation the range to the satellite was approximately 1050 km. Images were captured at a rate of 60 Hz, as they were for the open loop images. Several features are evident in the AO corrected image of Cosmos 1656. There is an array of panels which appear to be in a cross pattern at the base of the satellite which could be solar panels or for communications. The body of the satellite is above the cross array and there is a long thin object which appears to be extending from the top of the satellite body.

Cosmos 1656 was identified as a Tselina 2 satellite that was launched in 1985. Detailed information of the satellite such as dimensions could not be found; however, a render of the satellite was found and is shown in Figure 5.21. The Tselina 2 has a cross pattern array at the base as seen in the closed loop image in Figure 5.20. It also has has a long thin gravity boom that extends out from the top of the body. The Tselina 2 image has two solar panels which come out of the main body. These panels

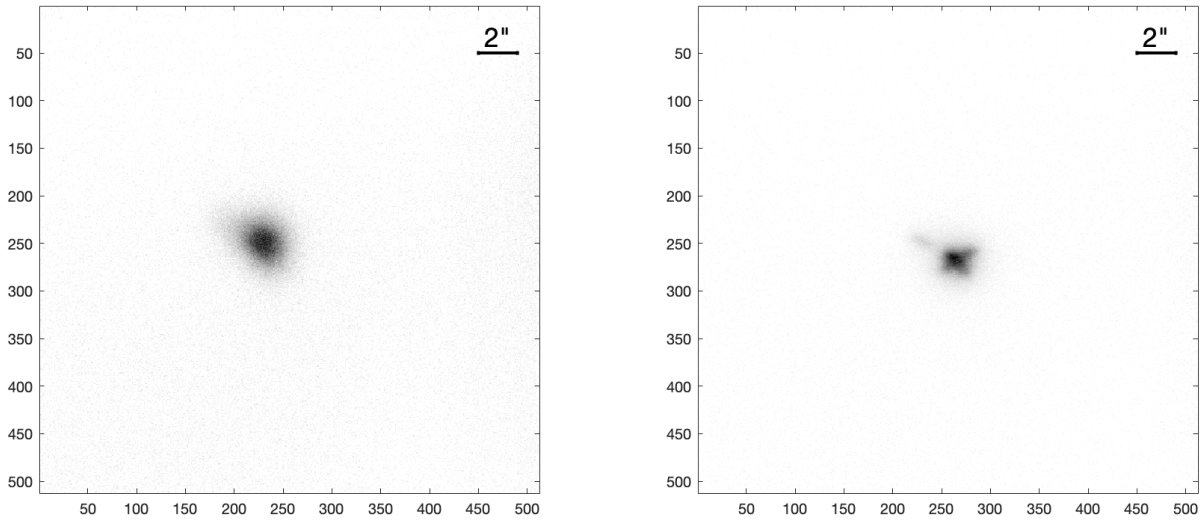


Figure 5.20: Left: Open loop image of Cosmos 1656 with cross correlation stacking. Right: Closed loop image of Cosmos 1656 with cross correlation stacking

are not seen in the closed loop image which could be due to the aspect the satellite was viewed, or the panels had been folded back into the body. Given the age of the satellite it is not likely to still be operational and thus it is a reasonable assumption that the solar panels were folded in at the end of life.

Figure 5.21: Image of Tselina 2 satellite [Dirk Krebs, 2017]

### 5.3.4 Multi-frame Blind Deconvolution

While the adaptive optics correction allows for more of the Cosmos 1656 structure to be seen, the image quality can be further improved using the multi frame blind deconvolution method outlined in Section 4.5. The same frames used to construct the cross correlation stacked image were fed into the MFBD algorithm. Although it should be possible to use all captured images in blind deconvolution as they will contain some information of the true underlying image, many frames in the data set were impacted by distortions not induced by the atmosphere. As discussed in Section 4.2 where there is offload to the telescope there can be significant shake in the telescope, which causes a smearing effect on the captured images. In addition to the telescope shake there were several frames where a column or row of the WFS spots were pushed into a neighbouring row or column resulting in a saddle shape on the DM. When the saddle occurred on the DM this would cause two images of the satellite to appear as shown in Figure 5.22. This was an unrealistic scenario, so all of these frames were discarded as they would corrupt the final image.

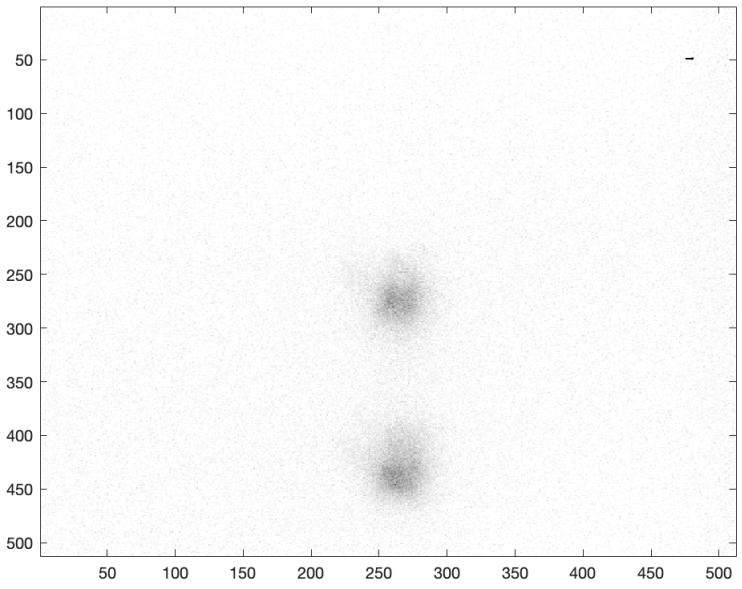


Figure 5.22: Image of Cosmos 1656 with DM saddle causing split image

The resulting image from the MFBD algorithm is shown in Figure 5.23. The image generated from the blind deconvolution has resulted in much sharper features becoming visible. The lower array of panels can be distinguished from the body more easily and the body width can be seen to be much smaller compared to the span of the panels which was less clear in the stacked image in Figure 5.20. Some of the antenna does not have any signal making it look like it is not connected to the satellite. This may be due to less signal coming from this part of the antenna as it is in shadow.

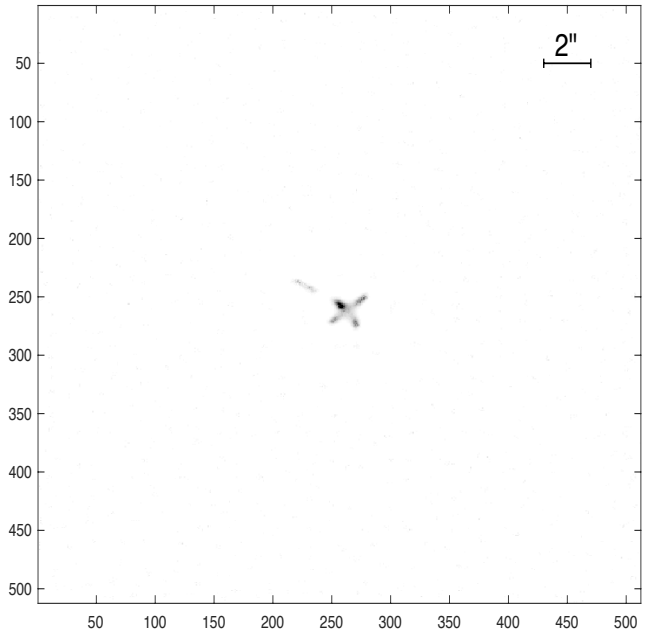


Figure 5.23: Cosmos 1656 after processing with multi-frame blind deconvolution

A visual inspection indicates the MFBD image has resulted in a sharper image. Figure 5.24 shows a comparison of the absolute value of fast Fourier transform for the stacked image and MFBD image. There is more high frequency information contained in the MFBD image of the satellite which is why there is more detail and sharpness.

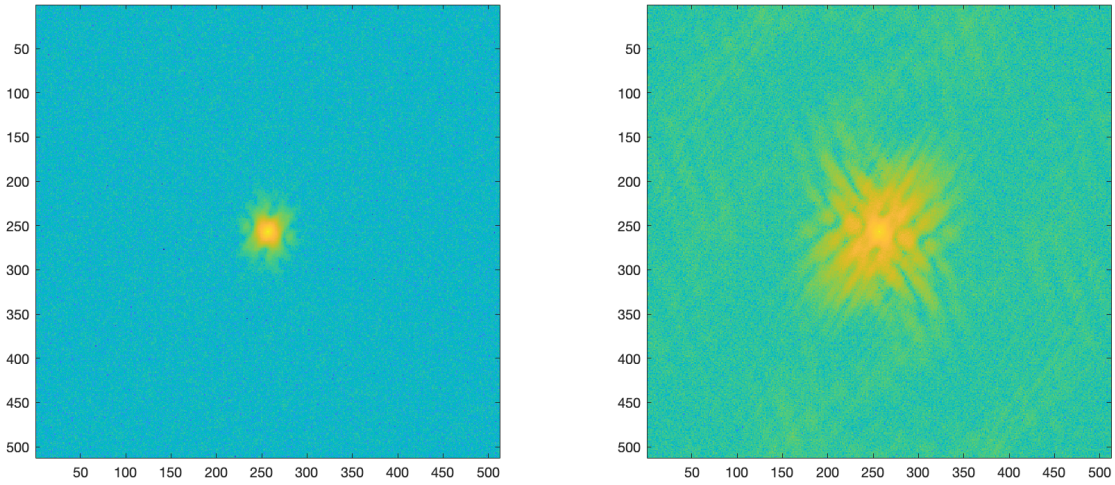


Figure 5.24: Left: FFT of closed loop image with cross correlation stacking. Right: FFT of MFBD image

### 5.3.5 Analysis

Measurements of the Cosmos 1656 were made using the MFBD image. There are several features which can be measured to find an angular size. Given the range to the satellite at the time of observation is known any angular size measurement can be transformed into a physical size. Features are measured by determining the full width half maximum of a cross sectional slice. As the object is extended the FWHM is found in the region where there is a rise from the background and again where it drops back to the background. Uncertainty in the measurement is estimated by finding the 20% and 80% point of the rise and fall in the feature. The true edge of the feature is likely to lie within this region. There were 6 features measured on the Cosmos 1656 satellite including lower panel width, panel span, body width, body length, gravity boom length, and gravity boom width which are shown in Figure 5.25. The cross sectional profiles of each of the features used to make the measurements is shown in Figure 5.26. Each of the profiles shows the FWHM along with the 20% and 80% representing the upper and lower bounds for the feature edge.

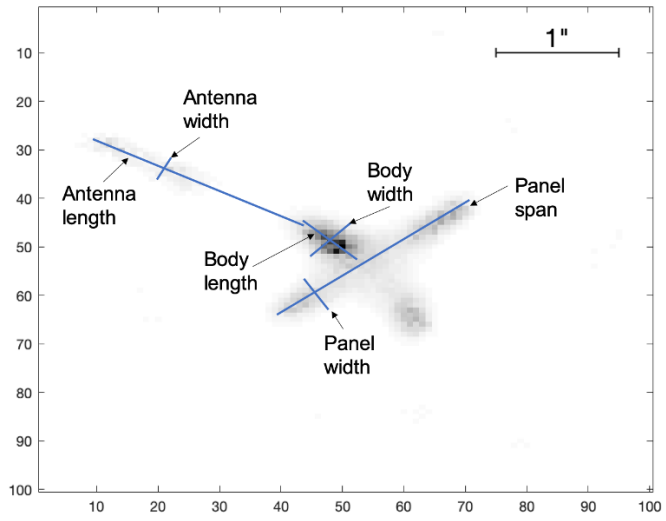


Figure 5.25: Features measured on Cosmos 1656 image

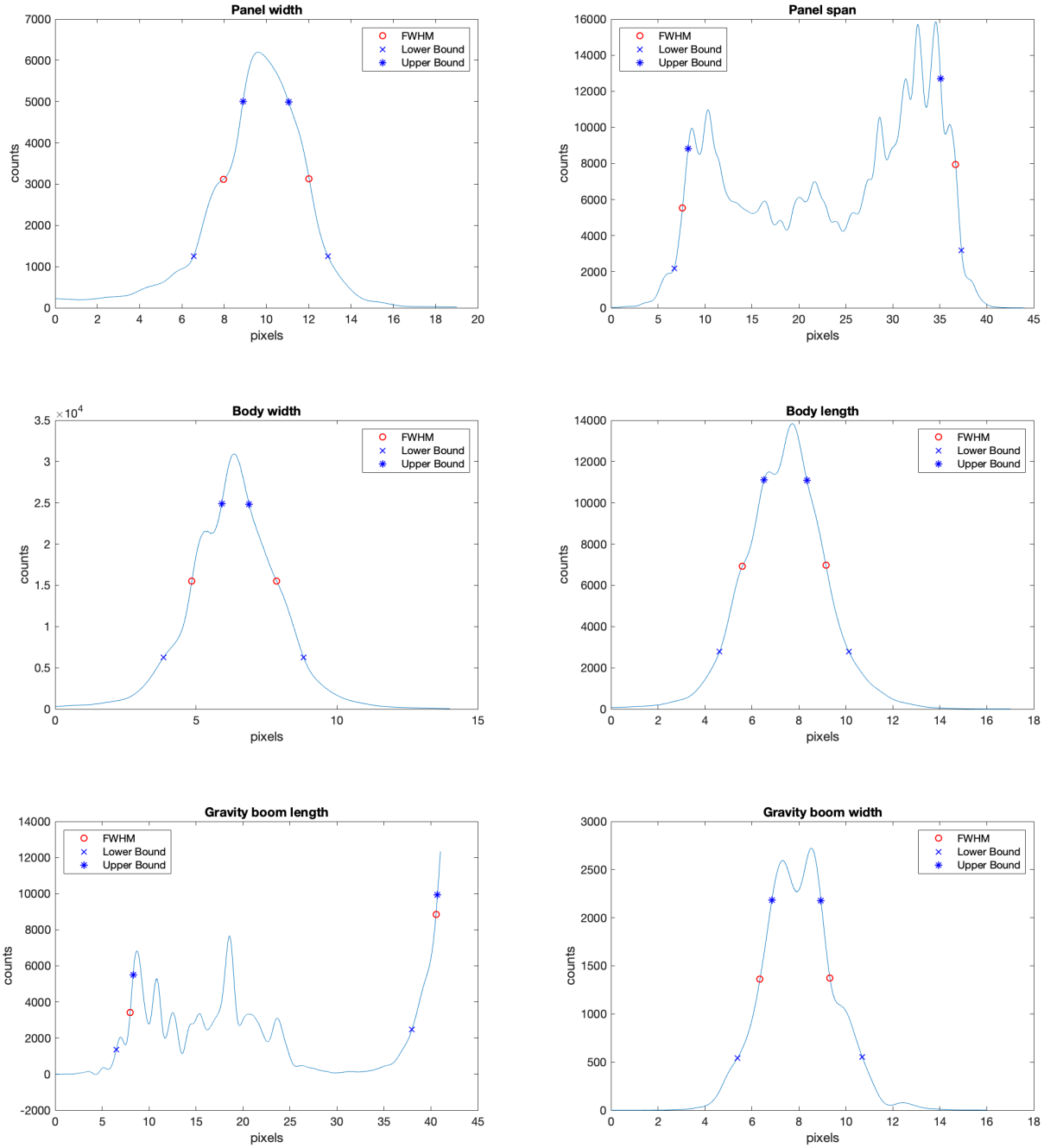


Figure 5.26: Cross-sectional measurements of Cosmos 1656 features

The measurements made for each of the features in Figure 5.26 is shown in Table 5.1. Given the known plate scale of AOI the size measured in pixels was transformed into an angular size by multiplying by the plate scale of 0.0472"/pixel.

Table 5.1: Size measurements of Cosmos 1656 features

| Description | Size (pixels) | Error (pixels) | Angular size (arcseconds) | Error (arcseconds) |
|---|---|---|---|---|
| Lower panel width | 4.06 | 2.1 | 0.192 | 0.099 |
| Lower panel array span | 29.1 | 1.85 | 1.37 | 0.087 |
| Body width | 3.01 | 2.01 | 0.142 | 0.095 |
| Body length | 3.55 | 1.85 | 0.168 | 0.087 |
| Gravity boom length | 32.6 | 2.25 | 1.54 | 0.106 |
| Gravity boom width | 2.98 | 1.61 | 0.141 | 0.076 |

The physical size can be determined from the angular size measurements in Table 5.1 as the distance to the satellite at the time of observations is known to be 1050 km. The physical size will be

$$x = d \tan \theta \tag{5.2}$$

where d is the distance from telescope to satellite and $\theta$ is the angular size. Given the very small angles the small angle approximation can be used so $x = d\theta$. The size of each feature is shown in Table 5.2.

## 5.4 Geostationary Orbit Tracking

### 5.4.1 Traditional Tracking

Tracking of objects in GEO has is performed by inferring position based on the position of the telescope and also using astrometry. Tracking of GEO satellites is typically done with small aperture telescopes, around 0.4 – 0.7 m diameter, and with large field of view. This allows for multiple objects within the GEO belt to be tracked simultaneously. Satellite positions are measured by determining the spot position in a frame

Table 5.2: Size measurements of Cosmos 1656 features

| Description | Size (m) |
|---|---|
| Lower panel width | $1.0 \pm 0.5$ |
| Lower panel array span | $7.0 \pm 0.4$ |
| Body width | $0.7 \pm 0.5$ |
| Body length | $0.9 \pm 0.4$ |
| Gravity boom length | $7.8 \pm 0.5$ |
| Gravity boom width | $0.7 \pm 0.4$ |

and relating that to an on-sky position. If the imaging plate scale is known then a distance from the centre of an image or the known reference star positions can be transformed to an actual position based on pointing information from the telescope. Astrometry measurements provide higher precision over telescope pointing and are more commonly used for GEO tracking.

Tracking GEO objects with passive imaging has drawbacks which can affect accuracy of the measurements. As with any other ground observation the atmospheric turbulence degrades the performance of the system. High order aberrations are of less concern as the only desired metric is the spot centroid. Low order modes such as tip-tilt can cause the spot to jump around and therefore, introduce error into measurements of the position. Such effects are minimised with GEO tracking systems as the pixels are relatively large meaning small movement in the spot are contained within the same pixels and therefore, not picked up. The issue with a large plate scale is a loss of precision with the measurements.

### 5.4.2 Astrometry

Astrometry is a method used in astronomy for measuring the position and movement of objects. When trying to measure an object of interest an image can be captured with known stars in the background. By measuring the distance and direction to the known star locations the position of the object can be measured very precisely. This same method could also be used to measure the location of satellites by measuring position relative to reference stars. AOI will be used to track GEO satellites by capturing images when a satellite passes by a known reference star. Figure 5.27 shows a

concept of how a satellite could be tracked while moving past a reference star. As the satellite nears the reference its position is jittery due to the atmospheric turbulence. When the satellite enters the isoplantic patch the wavefront distortions are corrected by the AO system and the path becomes more stable and the position relative to the star can be measured.

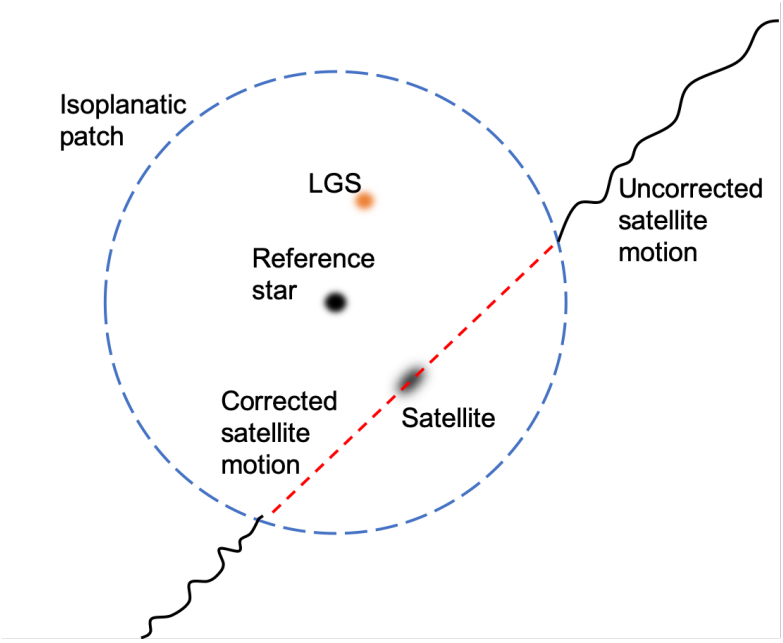


Figure 5.27: Concept of GEO object tracking. The telescope is tracking the reference star and as the satellite pass close to the star it is corrected by the adaptive optics and the position relative to the reference can be measured

Using astrometry for tracking satellites has unique challenges compared to traditional astrometry. If a GEO satellite is observed it is stationary in the sky relative to the observer and the stars are moving across the sky at the sidereal rate of 15"/sec, meaning there is a relative motion between the satellite and the stars. There will therefore only be short windows where the star and satellite are close to each other to make a measurement so the timing of observation is critical. Due to the relative movement the images a long exposure to collect sufficient light results in the stars imaged as a streak.

### 5.4.3 Tracking with Adaptive Optics

AOI provides an opportunity to use the same methods to track GEO satellites, but use AO to correct the atmosphere and take advantage of the small plate scale to make high precision measurements. The small field of view of AOI means that only one GEO satellite would be captured within a frame, the entire 25" FOV is approximately a 4.4 km square region at GEO. The addition of the AO correction would remove tip-tilt induced jitter allowing for a more consistent and accurate measurement of the position of the satellite in the frame.

The imaging frame rate of AOI will also mean that the stars would not become streaks as the exposure time is small enough to stop the star light moving over an extended number of pixels. This could provide higher precision measurement of the star position in the frame, which improves the accuracy of the satellite measurement.

### 5.4.4 Simulation of GEO Tracking

The tracking of a GEO satellite was also simulated by adding the transit of a satellite to images captured of a star during AOI operations. Stars move across the sky at the sidereal rate of 15"/sec while objects in GEO are stationary relative to the observer. Therefore, the star and satellite are moving relative to each other at a rate of 15"/sec. In this scenario the telescope is tracking the star so it will remain stationary in the images and the satellite will move across the field of view. As GEO satellites are typically magnitude 10 – 13 it is very difficult to get enough flux on the wavefront sensor to be able to close the AO loop. A bright enough star can be selected to enable stable closed loop operation so it is a better solution to track the star and allow the GEO object to transit through the frame. We use the star position as the astrometric reference and compute the position of the satellite based on the separation between the two objects.

With a 25" FOV the transit will be 1.7 seconds, which is approximately 100 frames if operating at the maximum speed of 60 Hz. The satellite position will move by 5 pixels/frame, which means that image stacking would not be possible. Instead each frame must be processed individually to identify the centroid of the star and satellite.

The position of the star is measured by locating local maxima in the image. The star will be brighter than a GEO object as it must be bright enough to be detected on the WFS; therefore, it will be brighter than magnitude 9. The Matlab function regionprops is used to locate local peaks in the image. When dealing with real data featuring noise, multiple local peaks are often found. However, most local peaks will not be from a real object. To filter out any unwanted identification of peaks a threshold is put in place for the brightness of the peak and size of the spot. The FWHM of a diffraction limited spot is approximately $3\times3$ pixels in size, so a local maximum that does not cover at least a 9 pixel area is likely not a real source and is disregarded. Once the peaks of the star and satellite are identified a weighted centroid is used to determine the position of each in the frame. This allows the position to be computed with sub-pixel precision. Figure 5.28 shows the identification of the star position and passing simulated satellite.

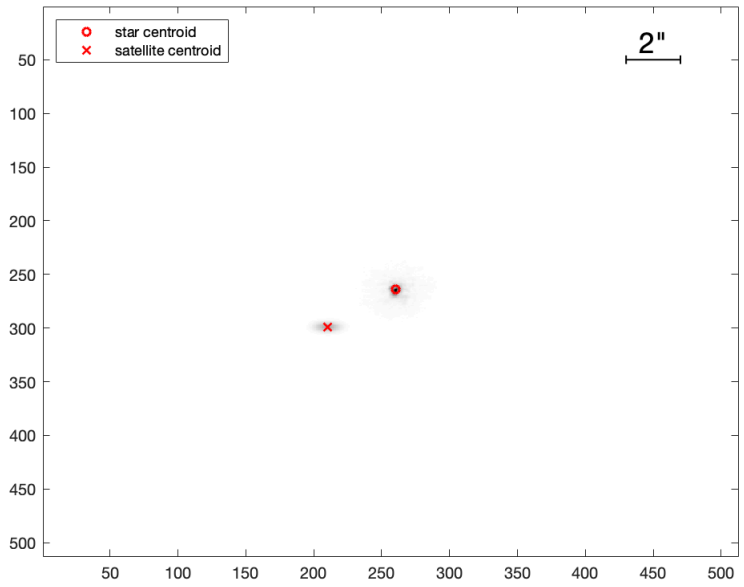


Figure 5.28: Simulated image of satellite passing by star. The centroids of the star and satellite have been measured and are marked

If correction of the star is poor and speckle remains in the image this speckle can be detected and the centroid found. To avoid false identification on the speckle a circular mask is applied to the image, which will set all values to zero within a 10 pixel radius of the star peak.

Once the centroid of the reference star and satellite are known the difference between the two centroids in the $(x, y)$ coordinate system is found by

$$\begin{aligned} \Delta x &= x_1 - x_2 \\ \Delta y &= y_1 - y_2 \end{aligned} \tag{5.3}$$

where $(x_1, y_1)$ is the coordinates of the satellite centroid and $(x_2, y_2)$ is the coordinates of the star centroid. The distance between the two centroid in pixels will be

$$dist = \sqrt{\Delta x^2 + \Delta y^2} \tag{5.4}$$

Additionally the angle between the two points is

$$ang = atan2(\Delta y, \Delta x) \tag{5.5}$$

The plate scale of the system is known to be 0.0472"/pixel so the distance calculated in Eq. 5.4 is multiplied by 0.05/3600 to determine the angular distance in degrees. A transform is then applied using the field rotation to find the separation in the $(Az, El)$ coordinate system

$$\begin{aligned} \Delta Az &= adist \times \cos(ang - frot) \\ \Delta El &= adist \times \sin(ang - frot) \end{aligned} \tag{5.6}$$

Given that the position of the star is known for each frame the position of the satellite can be found by

$$\begin{aligned} Az_{sat} &= Az_{star} + \Delta Az \\ El_{sat} &= El_{star} + \Delta El \end{aligned} \tag{5.7}$$

### 5.4.5 GEO Satellite Passing Reference Star

Measuring the position of a satellite as it passes by a reference star requires some knowledge of when the two will be in close proximity. The position of a GEO satellite is almost static relative to a ground observer, but some movement over time is expected. To determine the actual position of a GEO satellite at any given time the orbit is propagated using SGP4 and the latest TLE for the satellite. A Matlab package SGP4 OrbProp by Damon P. DeLuca is used for orbit propagation. These scripts include the SGP4 from [Vallado et al., 2006] and a script where satellite TLE and observer location can be entered via a GUI to output the satellite azimuth and elevation from the observers location.

The Orbprop Matlab script outputs a text file containing the azimuth and elevation of a satellite with specified time granularity. The position variation in azimuth and elevation is on the scale of $\pm 0.1$ degrees. Although the satellite remains stationary to the observer the sky is moving at the sidereal rate of 15"/sec so the region of stars chosen to compare positions must be chosen appropriately such that the patch of sky passes through the satellite position over the observation time frame. The Az/El coordinates obtained for the satellite are converted to RA/Dec to determine the box of sky that the satellite will occupy during the observation period. Over the period of 1 night the satellite will typically move over the 360 degree right ascension but be contained within a <1 degree region of declination.

The Gaia catalogue is used to search for stars that will be in the region of the satellite over the observation period. Gaia provides very accurate star positions with sub milliarcsecond error, which can be used for precision astrometry [Prusti et al., 2016; Brown et al., 2018]. The catalogue is filtered based on the RA/Dec region that the satellite occupies during the observation period and further filtered by only searching for stars with a visible magnitude of between 6 and 9, which is the range of magnitudes that can be used for adaptive optics operation. A list of stars that meet the search criteria is generated and contains the stars identifying number, RA, RA error, Dec, Dec error, and magnitude. This filtered list will contain 600 – 1500 sources and is downloaded for comparison with the satellite position.

The satellite position is calculated with a time step of 0.3 seconds. The RA/Dec position of the satellite at each 0.3 second interval is compared to the RA/Dec position of each star in the filtered catalogue downloaded from the Gaia archive. A proximity threshold of 30 arcseconds is used to determine when a star will pass close by the satellite and if the two objects are within this threshold the star information and time of proximity is recorded. This is calculated by finding the angular distance between the satellite and reference stars by

$$\theta = \cos^{-1}\left[\sin\delta_1 \sin\delta_2 + \cos\delta_1 \cos\delta_2 \cos\left(\alpha_1 - \alpha_2\right)\right] \tag{5.8}$$

where $\theta$ is the angular distance, $\delta_1$ and $\delta_2$ is the declination of the two objects, and $\alpha_1$ and $\alpha_2$ is the right ascension of the two objects.

When a star and satellite are identified to come in close proximity, the star identifying number, location in Ra/Dec, separation from satellite, magnitude, and time are recorded. This generates a list of possible targets for tracking a GEO satellite and the stars observed are selected from this list.

The number of identified events with a star and satellite passing within 15" of each other varies for each observation. There can be hours where there are no events followed by multiple events within minutes of each other. Based on observations a pass by of a star will occur on average every 30 minutes.

#### 5.4.5.1 Gaia Catalogue Acknowledgement

This work has made use of data from the European Space Agency (ESA) mission *Gaia* (https://www.cosmos.esa.int/gaia), processed by the *Gaia* Data Processing and Analysis Consortium (DPAC, https://www.cosmos.esa.int/web/gaia/dpac/consortium). Funding for the DPAC has been provided by national institutions, in particular the institutions participating in the *Gaia* Multilateral Agreement.

### 5.4.6 Tracking Results

Satellite TLEs are retrieved from the catalogue provided by www.space-track.org. The TLEs are retrieved on the day of observation so the most up to date TLE will be used for orbit propagation. The entire GEO belt is not visible from Australia and each TLE must be processed individually to determine the track so a selection of

GEO satellites known to be visible were chosen. The satellites chosen are shown in table 5.3. Also shown are the satellite ID and the approximate azimuth and elevation of the satellites. The satellites will move slightly over time but the deviation will be small.

Table 5.3: Satellites chosen for GEO tracking

| Satellite | NORAD ID | Azimuth (°) | Elevation (°) |
|---|---|---|---|
| Optus 10 | 40146 | 12.0 | 48.3 |
| Optus C1 | 27831 | 11.9 | 49.4 |
| Optus D1 | 29495 | 18.7 | 47.3 |
| Optus D2 | 32252 | 5.3 | 48.9 |
| Optus D3 | 35756 | 12.1 | 48.3 |
| Sky Muster 1 | 40940 | 345.0 | 47.9 |
| Sky Muster 2 | 41794 | 352.7 | 48.7 |

The 7 satellites in table 5.3 were chosen as they were the brightest visible GEO objects from Mt Stromlo Observatory. Choosing bright satellites would give a higher likelihood that a satellite would be detected in an observation. Optus are also a partner in SERC so it is possible to ask for precise location data to compare with tracking from AOI. All of the satellites are at a similar elevation of 47 – 49° and also lie within a 33° azimuth range. Optus 10 and D3 are particularly close together, located within 0.1° of each other. Although they are very close together, a separation of 0.1° is 360" so it would not be possible to capture an image of both in the same frame given the FOV of AOI is 25".

The elevation of the visible GEO satellites is not ideal for AO operations due to the higher air mass compared to objects close to zenith. If the elevation is 48° then the zenith angle is 42° and the AM is 1.35. The larger column of air the light passes through will induce more aberrations in the wavefront so more correction is required from the AO system. The latitude of Mt Stromlo Observatory means that no GEO satellite will be close to zenith.

During observations images were recorded when the expected proximity between a star and GEO satellite would occur. During one observation night there were 4 instances of a satellite being in close proximity to a star. The star magnitudes were between 7.3 and 8.8. For the magnitude 7.3 stars, the star could be easily acquired

on the WFS and loop could be closed at a rate of 1 kHz; however, it was difficult to close the loop on the magnitude 8.8 star. The WFS had to be slowed to 50 Hz at the maximum EM gain to see any spots. At this rate the signal was still very faint and the AO correction was extremely poor.

In all observations a satellite could not be seen passing by the reference star in the images that were captured. It is likely there was not enough signal from the magnitude 9.5 or dimmer GEO satellites that it could be seen above the background and camera noise. The images were captured on a night when the moon was almost full so there was significant background noise.

### 5.4.7 Discussion

The difficulty in detecting GEO satellites with AOI is due to the low flux entering the system. Replacing the dichroic beamsplitter with a broadband beamsplitter significantly impacted the flux that was reflected to the imaging camera. If the longpass filter remains in place to maintain the chromatic performance of the imaging system only 30% of the available flux will go to the imaging camera. As the flux to the imaging camera is approximately 3.3 times smaller then originally designed when using the dichroic beamsplitter, the detectable magnitude of the system is decreased. A magnitude interval of 1 will have a difference in brightness of $\sqrt[5]{100} \approx 2.512$ times, so there is a loss of more than 1 magnitude when using the beamsplitter over the dichroic.

During star observations it was difficult to see stars on the imaging camera for magnitudes of 8 and larger. Figure 5.29 shows a single frame image of a magnitude 8.40 star while running in closed loop. As with other observations of dim stars the WFS was slowed so there was enough flux in each subaperture to close the loop. The WFS was running at a rate of 200 Hz with an EM gain of 600. Images were captured at a rate of 60 Hz with an EM gain of 1000.

The image of the star is evident, although the correction is poor due to the lack of flux on the WFS. The noise surrounding the star is at similar intensity to the signal so it would be difficult to detect objects that are dimmer. If it were not necessary to use the broadband beamsplitter in place of the dichroic beamsplitter then it is possible objects 1 magnitude dimmer would be detectable and therefore, a 9.5 magnitude GEO satellite may be possible to track.

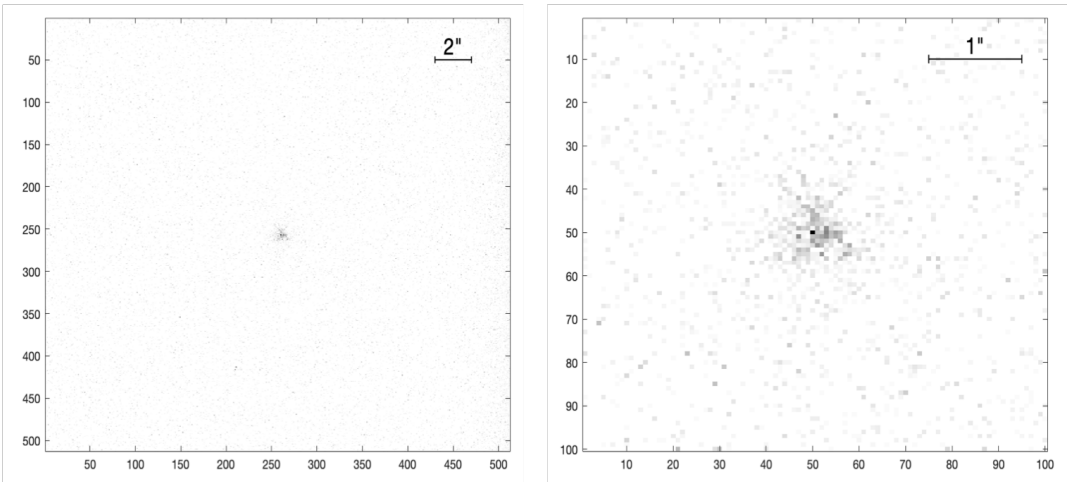


Figure 5.29: Left: Full frame closed loop image of magnitude 8.40 star. Right: 100×100 pixel section of closed loop image of magnitude 8.40 star

Reducing the imaging frame rate is a method to detect dimmer objects as the camera has a longer period to collect light. In the case of tracking a GEO satellite it is unlikely to aid in detecting the satellites as the system is tracking stars and the satellites are moving relative to the stars at 15"/s. A lower frame rate will collect more flux but as the satellite is moving during the integration period this flux will be spread over a large streak so it will be no easier to detect.

Observation of GEO satellites with AOI is also made difficult due to the high resolution of the system. GEO satellites can be easily detected with a smaller 0.4 m telescope due to longer exposure times and much wider field of view. A traditional GEO tracking system can have a FOV >1 degree, which results in a plate scale of >10"/pixel. Therefore, even when observing through a turbulent atmosphere the light is concentrated into 1 – 2 pixels so it is easier to detect a dim object. As the AOI plate scale is 0.047"/pixel a spot can be spread over a 50 pixel diameter in 2" seeing conditions making it extremely difficult to detect a dim object without an AO correction.

The unsuccessful attempts to observe the GEO satellites were all made in the same night. Operations were halted due to the bushfire smoke, and shortly after a major fault was found with the azimuth drive of the telescope. This fault could not be fixed within the time-frame of this thesis so no further observations were possible. Therefore, it was not possible to preform any troubleshooting to get the system to work. If further observations were possible, a simple test was planned to point and

track a GEO satellite to determine if it was visible in the system. In this situation the exposure time of the camera could be adjusted until a signal is received. Due to the limited opportunities it is not possible to say the unsuccessful results are due to limitations of the system, or because the system required some adjustments.

Chapter 6

# Conclusion

In this thesis I have presented the design and operation of the Adaptive Optics Imaging system for space situational awareness. AOI was used to successfully improve the image of a star through the adaptive optics correction. Images of low Earth orbit satellites were captured with the adaptive optics correction allowing for features to be resolved and measurements of the characteristics to be made. Multi-frame blind deconvolution image processing further improved image quality.

AOI is an adaptive optics system for satellite and debris imaging for characterising and tracking objects in LEO and GEO. AOI was designed to operate on a 1.8 m telescope at Mt Stromlo Observatory in Canberra, Australia. The key components of the AO system were chosen so AOI would work effectively at the site. A 277 actuator deformable mirror with 17×17 actuators across the pupil allowed for a WFS with 16 subapertures across the telescope primary mirror. The WFS camera operates at up to 2 kHz so correction can be applied to fast moving LEO objects where the telescope must slew quickly to track. A 512×512 pixel imaging camera that can operate at up to 60 Hz is used to capture high resolution images.

The optical design of AOI was completed to meet the performance requirements of the system. To reduce cost and complexity commercial optics were used where possible, however four custom achromatic doublets were needed for acceptable chromatic performance. The custom lenses were used in the beam expander and imaging arm to give diffraction limited imaging for 650 – 950 nm wavelengths. AOI was built using mostly COTS mechanical parts, and some custom parts where necessary. The system was integrated on an optical table in the telescope clean room.

Significant improvement of a star image was achieved by running AOI in closed loop. A Strehl ratio of 34% during closed loop met the performance expectations of the system. The AO correction also stabilised the image of the detector by removing the large tip-tilt, the average motion was reduced by a factor of 5 from 0.43 to 0.08 arcseconds.

An image of a LEO satellite was successfully captured using AOI. Cosmos 1656, a defunct Russian satellite, was observed in open and closed loop. Several features of the satellite became apparent when using adaptive optics such as the communication panels, satellite body, and antenna. These features could not be seen without the adaptive optics. The images were further improved by using MFBD which resulted in more detail. Several measurements of the features was made to determine the overall size of the satellite and the size of the specific features.

A method was developed to track geostationary orbit satellites by measuring their position relative to a reference star from the Gaia catalogue. This method was tested by adding a simulated satellite passing through images collected from a star. The centroid of the satellite and star were determined so their relative separation could be measured. Several attempts were made to observe a GEO satellite as it was passing by a star, however the satellites could not be seen in any images as they were too dim to detect.

## 6.1 Future Work

Further on-sky operations can be used to identify objects in LEO and track objects in GEO. External issues prevented proper troubleshooting in the GEO tracking observations and further on-sky time could allow the system to be adjusted and optimised.

The addition of a LGS to the telescope will enable dimmer objects to be imaged as the WFS is not relying on the brightness of the object to measure the distorted wavefront. The LGS mode of AOI will utilise more of the reflected sunlight so dimmer objects can be imaged. This could allow for GEO objects to be more easily detected and allow for tracking of a GEO satellite as it passes by a reference star.

An experiment will soon be conducted to attempt manoeuvring a piece of debris in LEO to demonstrate photon pressure pushing for collision avoidance. AOI can provide support for this experiment by identifying suitable candidates for pushing. The experiment requires high area to mass ratio objects such as flat sheets. This maximises the momentum that can be transferred by the photons, making the object more likely to move.

AOI could also be used as a test bed for ground to space optical communications. Propagating a laser beam through the atmosphere to transmit data faces the same issues any other telescope due to the atmospheric turbulence. Pre-compensating a laser beam so the aberrations in the beam after propagating through the atmosphere are minimised can increase signal strength and stability leading to more effective communications. AOI optics are coated for the standard optical communications wavelength of 1550 nm, and thus could be utilised to as a communications system.

# Bibliography


ALPAO, 2019. Deformable Mirros. https://www.alpao.com/adaptive-optics/deformable-mirrors.html.

Anselmo, L. and Pardini, C., 2009. Analysis of the consequenses in low Earth orbit of the collision between cosmos 2251 and Iridium 33. , 1 (2009).

Ayers, G. R. and Dainty, J. C., 1988. Iterative blind deconvolution method and its applications. *Optics Letters*, 13, 7 (1988), 547. doi:10.1364/ol.13.000547.

Babcock, H. W., 1953. The Possibility of Compensating Astronomical Seeing. *Publications of the Astronomical Society of the Pacific*, 65 (1953), 229. doi:10.1086/126606.

Beckers, J. M., 1993. Adaptive optics for astronomy: Principles, Perfomance and Applications. *Annu. Rev. Astron. Astrophys.*, 31 (1993), 13–62. doi:10.1146/annurev.aa.31.090193.000305.

Bennett, J. C.; Sang, J.; Smith, C. H.; and Zhang, K., 2013. Accurate orbit predictions for debris orbit manoeuvre using ground-based lasers. *Advances in Space Research*, 52, 11 (2013), 1876–1887. doi:10.1016/j.asr.2013.08.029. http://dx.doi.org/10.1016/j.asr.2013.08.029.

Brown, A. G. A.; Vallenari, A.; Prusti, T.; de Bruijne, J. H. J.; Babusiaux, C.; Bailer-Jones, C. A. L.; Biermann, M.; Evans, D. W.; Eyer, L.; Jansen, F.; Jordi, C.; and Et al, ., 2018. Gaia Data Release 2. *Astronomy & Astrophysics*, 616 (aug 2018), A1. doi:10.1051/0004-6361/201833051. https://www.aanda.org/10.1051/0004-6361/201833051.

Buffington, A.; Crawford, F. S.; Muller, R. A.; Schwemin, A. J.; and Smits, R. G., 1977. Correction of atmospheric distortion with an image-sharpening telescope. *Journal of the Optical Society of America*, 67, 3 (1977), 298. doi:10.1364/josa.67.000298.

Cohen, S. C. and Smith, D. E., 1985. LAGEOS scientific results: introduction. *Journal of Geophysical Research*, 90, B11 (1985), 9217–9220. doi:10.1029/JB090iB11p09217. http://doi.wiley.com/10.1029/JB090iB11p09217.

Colodro-Conde, C.; López López, R.; Oscoz, A.; Rebolo-López, R.; Labadie, L.; Martín-Hernando, Y.; Pérez-Garrido, A.; Velasco Muñoz, S.; and MacKay, C., 2018. The adaptive optics lucky imager (AOLI): presentation, commissioning, and AIV innovations. (2018), 216. doi:10.1117/12.2311982.

Cranford, K. and Lane, M., 1969. An improved analytical drag theory for the artificial satellite problem. In *Astrodynamics Conference*. American Institute of Aeronautics and Astronautics, Reston, Virigina. doi:10.2514/6.1969-925. http://arc.aiaa.org/doi/10.2514/6.1969-925.

Degnan, J., 1985. Satellite Laser Ranging: Current Status and Future Prospects. *IEEE Transactions on Geoscience and Remote Sensing*, GE-23, 4 (1985), 398–413. doi:10.1109/TGRS.1985.289430. http://ieeexplore.ieee.org/lpdocs/epic03/wrapper.htm?arnumber=4072319.

Dirk Krebs, G., 2017. Tselina-2 (11F644). https://space.skyrocket.de/doc{_}sdat/tselina-2.htm.

Eichler, P. and Rex, D., 1990. Debris chain reactions. In *Orbital Debris Conference: Technical Issues andFuture Directions*. American Institute of Aeronautics and Astronautics, Reston, Virigina. doi:10.2514/6.1990-1365. http://arc.aiaa.org/doi/10.2514/6.1990-1365.

Estell, N.; Ma, D.; and Seitzer, P., 2019. Daylight imaging of LEO satellites using COTS hardware. In *AMOS Technologies Conference*, September, 17–20.

European Space Agency, 2016. Impact Chip. https://www.esa.int/ESA{_}Multimedia/Images/2016/05/Impact{_}chip.

European Space Agency, 2019. ESA spacecraft dodges large constellation. https://www.esa.int/Safety{_}Security/ESA{_}spacecraft{_}dodges{_}large{_}constellation.

European Space Agency and Kramer, H. J., 2019. EnviSat (Environmental Satellite). https://earth.esa.int/web/eoportal/satellite-missions/e/envisat.

Fan, Y. W. and Nagy, J. G., 2012. An efficient computational approach for multiframe blind deconvolution. In *Journal of Computational and Applied Mathematics*, vol. 236, 2112–2125. Elsevier B.V. doi:10.1016/j.cam.2011.09.034. http://dx.doi.org/10.1016/j.cam.2011.09.034.

Foy, R. and Labeyrie, A., 1985. Feasibility of adaptive telescope with laser probe. *Astronomy and astrophysics (Berlin. Print)*, 152, 2 (1985).

Fried, D. L., 1965. Statistics of a Geometric Representation of Wave-front Distortion. *Journal of the Optical Society of America*, 56, 3 (1965), 410. doi:10.1364/josa.56.000410.

Fried, D. L., 1966. Optical Resolution Through a Randomly Inhomogeneous Medium for Very Long and Very Short Exposures. *Journal of the Optical Society of America*, 56, 10 (1966), 1372. doi:10.1364/josa.56.001372.

Fried, D. L., 1977. Least-square fitting a wave-front distortion estimate to an array of phase-difference measurements. *Journal of the Optical Society of America*, 67, 3 (1977), 370. doi:10.1364/josa.67.000370.

Fried, D. L., 1978. Probability of Getting a Lucky Short-Exposure Image Through Turbulence. *J Opt Soc Am*, 68, 12 (1978), 1651–1658. doi:10.1364/JOSA.68.001651.

Fried, D. L., 1982. Anisoplanatism in Adaptive Optics. *Journal of the Optical Society of America*, 72, 1 (1982), 52–61. doi:10.1364/JOSA.72.000052.

Fruh, C.; Jah, M.; and Kelecy, T., 2013. Coupled Orbit-Attitude Dynamics of High Area-to-Mass Ratio (HAMR) Objects: Influence of Solar Radiation Pressure, Earth's Shadow and the Visibility in Light Curves. *Celestial Mechanics and Dynamical Astronomy*, 117, 4 (2013), 385–404. doi:10.1007/s10569-013-9516-5. http://arxiv.org/abs/1312.0067http://dx.doi.org/10.1007/s10569-013-9516-5.

Fugate, R. Q., 2003. The Starfire Optical Range 3.5-m Adaptive Optical Telescope. *Large Ground-based Telescopes*, 4837, February 2003 (2003), 934. doi:10.1117/12.457972.

Fugate, R. Q.; Fried, D. L.; Ameer, G. A.; Boeke, B. R.; Browne, S. L.; Roberts, P. H.; Ruane, R. E.; Tyler, G. A.; and Wopat, L. M., 1991. Measurement of atmospheric wavefront distortion using scattered light from a laser guide-star. *Nature*, 353, 6340 (1991), 144–146. doi:10.1038/353144a0.

Greenwood, D. P., 1977. Bandwidth specification for adaptive optics systems. *Journal of the Optical Society of America*, 67, 3 (1977), 390. doi:10.1364/josa.67.000390.

Grosse, D.; Bennet, F.; Korkiakoski, V.; Rigaut, F.; and Thorn, E., 2016. Single detector stereo-SCIDAR for Mount Stromlo. *Adaptive Optics Systems V*, 9909 (2016), 99093D. doi:10.1117/12.2232149.

Grosse, D.; Bennet, F.; Rigaut, F.; D'Orgeville, C.; Korkiakoski, V. A.; Smith, C. H.; Copeland, M.; Price, I.; Blundell, M.; Chan, A.; Ellis, M.; Galla, A.; Gers, L.; Hart, J.; Lingham, M.; Gao, Y.; Houston, E.; Rees, E. R.; Wang, Y.; Ritchie, I.; Travouillon, T.; Vaccarella, A.; and Webb, J., 2018. Adaptive optics tracking and pushing system for space debris manoeuvre. In *Adaptive Optics Systems VI*, July 2018, 24. SPIE. doi:10.1117/12.2313181. https://www.spiedigitallibrary.org/conference-proceedings-of-spie/10703/2313181/Adaptive-optics-tracking-and-pushing-system-for-space-debris-manoeuvre/10.1117/12.2313181.full.

Happer, W.; MacDonald, G. J.; Max, C. E.; and Dyson, F. J., 1994. Atmospheric-turbulence compensation by resonant optical backscattering from the sodium layer in the upper atmosphere. *Journal of the Optical Society of America A*, 11, 1 (1994), 263. doi:10.1364/josaa.11.000263.

Hardy, J. W.; Lefebvre, J. E.; and Koliopoulos, C. L., 1977. Real-time atmospheric compensation. *Journal of the Optical Society of America*, 67, 3 (1977), 360. doi:10.1364/josa.67.000360.

Hart, M., 2018. Image registration for daylight adaptive optics. *Optics Letters*, 43, 6 (2018), 1391. doi:10.1364/ol.43.001391.

Heavens-Above, 2019. Heavens-Above. https://www.heavens-above.com.

Hirsch, M.; Harmeling, S.; Sra, S.; and Schölkopf, B., 2011. Online multi-frame blind deconvolution with super-resolution and saturation correction. *Astronomy and Astrophysics*, 531 (2011), 1–11. doi:10.1051/0004-6361/200913955.

Hope, D. A.; Jefferies, S. M.; and Smith, C., 2019. High-Fidelity Imaging Using Compact Multi-Frame Blind Deconvolution. *Journal of the Astronautical Sciences*, 66, 2 (2019), 162–169. doi:10.1007/s40295-018-00148-x.

Hunten, D. M., 1981. A meteorâĂŘablation model of the sodium and potassium layers. *Geophysical Research Letters*, 8, 4 (apr 1981), 369–372. doi:10.1029/GL008i004p00369. http://doi.wiley.com/10.1029/GL008i004p00369.

Johnson, N. L., 2010. Orbital debris: The growing threat to space operations. *Advances in the Astronautical Sciences*, 137, Figure 1 (2010), 3–11.

Johnson, N. L.; Stansbery, E.; Liou, J. C.; Horstman, M.; Stokely, C.; and Whitlock, D., 2008. The characteristics and consequences of the break-up of the Fengyun-1C spacecraft. *Acta Astronautica*, 63, 1-4 (2008), 128–135. doi:10.1016/j.actaastro.2007.12.044.

Kelso, T. S., 2010. Analysis of the Iridium 33-Cosmos 2251 collision. *Advances in the Astronautical Sciences*, 135, July (2010), 1099–1112.

Kessler, D. J., 1991. Collisional cascading: The limits of population growth in low earth orbit. *Advances in Space Research*, 11, 12 (1991), 63–66. doi:10.1016/0273-1177(91)90543-S.

Kessler, D. J. and Cour-Palais, B. G., 1978. Collision frequency of artificial satellites: The creation of a debris belt. *Journal of Geophysical Research*, 83, A6 (1978), 2637. doi:10.1029/JA083iA06p02637. http://doi.wiley.com/10.1029/JA083iA06p02637.

Kolmogorov, A. N., 1941. The local structure of turbulence in incompressible viscous fluid for very large Reynolds numbers. *Cr Acad. Sci. URSS*, 30 (1941), 301–305.

Lachut, M. and Bennett, J., 2016. Towards Relaxing the Spherical Solar Radiation Pressure Model for Accurate Orbit Predictions. In *Advanced Maui Optical and Space Surveillance Technologies (AMOS) Conference*. http://www.amostech.com/TechnicalPapers/2016/Astrodynamics/Lachut.pdf.

Lam, E. Y. and Goodman, J. W., 2000. Iterative statistical approach to blind image deconvolution. *Journal of the Optical Society of America A*, 17, 7 (2000), 1177. doi:10.1364/josaa.17.001177.

Lane, M., 1965. The development of an artificial satellite theory using a power-law atmospheric density representation. In *2nd Aerospace Sciences Meeting*. American Institute of Aeronautics and Astronautics, Reston, Virigina. doi:10.2514/6.1965-35. http://arc.aiaa.org/doi/10.2514/6.1965-35.

Liou, J. C. and Johnson, N. L., 2009. Characterization of the cataloged Fengyun-1C fragments and their long-term effect on the LEO environment. *Advances in Space Research*, 43, 9 (2009), 1407–1415. doi:10.1016/j.asr.2009.01.011. http://dx.doi.org/10.1016/j.asr.2009.01.011.

Liou, J. C.; Johnson, N. L.; and Hill, N. M., 2010. Controlling the growth of future LEO debris populations with active debris removal. *Acta Astronautica*, 66, 5-6 (2010), 648–653. doi:10.1016/j.actaastro.2009.08.005. http://dx.doi.org/10.1016/j.actaastro.2009.08.005.

Lucchesi, D. M., 2001. Reassessment of the error modelling of non-gravitational perturbations on LAGEOS II and their impact in the Lense-Thirring determination. Part I. *Planetary and Space Science*, 49, 5 (2001), 447–463. doi:10.1016/S0032-0633(00)00168-9.

Mahajan, V. N., 1983. STREHL RATIO FOR PRIMARY ABERRATIONS IN TERMS OF THEIR ABERRATION VARIANCE. *Journal of the Optical Society of America*, 73, 6 (1983), 860–861. doi:10.1364/JOSA.73.000860.

Mason, J.; Stupl, J.; Marshall, W.; and Levit, C., 2011. Orbital debris-debris collision avoidance. *Advances in Space Research*, 48, 10 (2011), 1643–1655. doi:10.1016/j.asr.2011.08.005.

McCarthy, P. J.; Ashby, D. S.; Bigelow, B. C.; Bouchez, A. H.; Burgett, W. S.; Chauvin, E.; Contos, A.; Figueroa, F.; Gray, P.; Groark, F.; Laskin, R.; Millan-Gabet, R.; Rakich, A.; Sandoval, R.; Fanson, J. L.; Bernstein, R.; Angeli, G. Z.; Pi, M.; and Wheeler, N., 2018. Overview and status of the Giant Magellan Telescope project. 1070012, July 2018 (2018), 34. doi:10.1117/12.2313340.

McMahon, J. W. and Scheeres, D. J., 2015. Improving Space Object Catalog Maintenance Through Advances in Solar Radiation Pressure Modeling. *Journal of Guidance, Control, and Dynamics*, 38, 8 (aug 2015), 1366–1381. doi:10.2514/1.G000666. http://arc.aiaa.org/doi/10.2514/1.G000666.

NASA, 2017. LAGEOS: LAser GEOdynamic Satellite. https://lageos.cddis.eosdis.nasa.gov.

Noll, R. J., 1976. Zernike polynomials and atmospheric turbulence. *J Opt Soc Am*, 66, 3 (1976), 207–211. doi:10.1364/JOSA.66.000207.

Phipps, C. R.; Baker, K. L.; Libby, S. B.; Liedahl, D. A.; Olivier, S. S.; Pleasance, L. D.; Rubenchik, A.; Trebes, J. E.; George, E. V.; Marcovici, B.; Reilly, J. P.; and Valley, M. T., 2012. Removing orbital debris with pulsed lasers. In *AIP Conference Proceedings*, vol. 1464, 468–480. doi:10.1063/1.4739901.

Prabhat, P. and Erdogan, T. Flatness of Dichroic Beamsplitters Affects Focus and Image Quality. Technical report, Semrock Inc. https://www.semrock.com/flatness-of-dichroic-beamsplitters-affects-focus-and-image-quality.aspx.

Primmerman, C. A.; Murphy, D. V.; Page, D. A.; Zollars, B. G.; and Barclay, H. T., 1991. Compensation of atmospheric optical distortion using a synthetic beacon. *Nature*, 353, 6340 (1991), 141–143. doi:10.1038/353141a0.

Prusti, T.; De Bruijne, J. H.; Brown, A. G.; Vallenari, A.; Babusiaux, C.; Bailer-Jones, C. A.; Bastian, U.; Biermann, M.; Evans, D. W.; Eyer, L.; and Et al, ., 2016. The Gaia mission. *Astronomy and Astrophysics*, 595, 29272 (2016). doi:10.1051/0004-6361/201629272.

Roddier, F., 1999. *Adaptive Optics in Astronomy*. Cambridge University Press. ISBN 0 521 55375.

Schulz, T.; Stribling, B.; and Miller, J., 1997. Multiframe blind deconvolution with real data: imagery of the Hubble Space Telescope. *Optics Express*, 1, 11 (1997), 355. doi:10.1364/oe.1.000355.

Shack, R. V. and Platt, B. C., 1971. Production and use of a lenticular Hartmann screen. *Journal of the Optical Society of America*, 61 (1971), 656–660.

Shepherd, H. W.; Osborn, J.; Wilson, R. W.; Butterley, T.; Avila, R.; Dhillon, V. S.; and Morris, T. J., 2014. Stereo-SCIDAR: Optical turbulence profiling with high sensitivity using a modified SCIDAR instrument. *Monthly Notices of the Royal Astronomical Society*, 437, 4 (2014), 3568–3577. doi:10.1093/mnras/stt2150.

Space-Track, 2019. Space-Track.org. https://www.space-track.org.

Su, S. Y., 1986. Orbital debris environment resulting from future activities in space. *Advances in Space Research*, 6, 7 (1986), 109–117. doi:10.1016/0273-1177(86)90219-X.

Tamai, R.; Cirasuolo, M.; González, J. C.; Koehler, B.; and Tuti, M., 2016. The E-ELT program status. *Ground-based and Airborne Telescopes VI*, 9906, July 2016 (2016), 99060W. doi:10.1117/12.2232690.

TelescopeOptics. Monochromatic eye aberrations. https://www.telescope-optics.net/monochromatic{_}eye{_}aberrations.htm.

Vallado, D. and Crawford, P., 2008. SGP4 Orbit Determination. In *AIAA/AAS Astrodynamics Specialist Conference and Exhibit*. American Institute of Aeronautics and Astronautics, Reston, Virigina. doi:10.2514/6.2008-6770. http://arc.aiaa.org/doi/10.2514/6.2008-6770.

Vallado, D. A.; Crawford, P.; Hujsak, R.; and Kelso, T. S., 2006. *Revisiting spacetrack report #3*, vol. 3. American Institute of Aeronautics and Astronautics. ISBN 1563478226. doi:10.2514/6.2006-6753.

Valley, G. C., 1980. Isoplanatic degradation of tilt correction and short-term imaging systems. *Applied Optics*, 19, 4 (1980), 574. doi:10.1364/ao.19.000574.

Vernin, J. and Roddier, F., 1973. Experimental Determination of Two-Dimensional Spatiotemporal Power Spectra of Stellar Light Scintillaton. Evidence for a Multilayer Structure of the Air Turbulence in the Upper Troposphere. *J Opt Soc Am*, 63, 3 (1973), 270–273. doi:10.1364/josa.63.000270.

Wilson, R. W., 2002. SLODAR: Measuring optical turbulence altitude with a Shack-Hartmann wavefront sensor. *Monthly Notices of the Royal Astronomical Society*, 337, 1 (2002), 103–108. doi:10.1046/j.1365-8711.2002.05847.x.